UC Santa Cruz

UC Santa Cruz Electronic Theses and Dissertations

Title

Integrated Optofluidic PDMS Biosensor Devices

Permalink

https://escholarship.org/uc/item/9mb6q748

Author

Sano, Tyler Taira

Publication Date

2023

Peer reviewed|Thesis/dissertation

UNIVERSITY OF CALIFORNIA

SANTA CRUZ

INTEGRATED OPTOFLUIDIC PDMS BIOSENSOR DEVICES

A dissertation submitted in partial satisfaction

of the requirements for the degree of

DOCTOR OF PHILOSOPHY

in

ELECTRICAL AND COMPUTER ENGINEERING

by

Tyler Sano

December 2023

The Dissertation of Tyler Sano

is approved by:

_____

Professor Holger Schmidt, Chair

_____

Professor Marco Rolandi

_____

Professor Mircea Teodorescu

_____

Peter F. Biehl

Vice Provost and Dean of Graduate Studies

Table of Contents

List of Figures

Fig. 4.3 Laser characterization. a) A broadband ASE spectrum (green) is demonstrated when pumped below threshold while the narrowed lasing spectrum (orange) is observed when the Rhodamine 6G laser is illustrated when pumped above threshold. b) Similarly, a broadband DCM ASE spectrum (blue) is observed when pumped below threshold while the narrowed lasing spectrum (red) is overlayed when the DFB is pumped above threshold. c), d) Normalized average output power as a function of input pump power for the Rhodamine 6G and DCM lasers, respectively. The orange and red lines are linear fits conducted on the data points above threshold.

Fig. 4.4 Mode images of the Rhodamine 6G and DCM lasers imaged using a 10x objective (top). The mode images were then imaged individually using a 40x objective (bottom) and integrated horizontally and vertically to extract X and Y mode profiles.

Fig. 4.5 Simultaneous detection of two types of fluorescent microspheres. a) Fluorescence time domain trace from the Rhodamine 6G laser ROI illustrated peaks from detection of 1 μm red fluorescence beads. The zoomed image illustrates an individual event. b) Fluorescence time domain trace from the DCM laser excitation ROI illustrating peaks from detection of 2 μm flash red beads. c), d) Intensity histograms from the detected red and flash red fluorescent beads, respectively.

Fig. 4.6 Negative controls. a) Fluorescence time domain trace from the Rhodamine 6G laser excitation ROI when only flash red beads were flown. b) Fluorescence time domain trace from the DCM laser excitation ROI when only red fluorescent beads were flown.

Fig. 5.1 Top: Device schematic of all-in-one PDMS optofluidic LOC consisting of three distinct regions: sample preparation (red), on-chip DFB laser (purple), and optical detection region (green). Bottom: Cross-sectional diagrams of pneumatic lifting-gate valve structures with positive pressure used to close valves (i) and negative pressure used to lift valves and allow fluid flow between adjacent valves (ii).

Fig. 5.2 Top-down camera image of the all-in-one LOC indicating each of the on-chip modules: sample preparation (red), DFB laser (purple), and optical detection (white).

Fig. 5.3 Non-specific biomarker detection. a) dsDNA assay outline. 1 μm streptavidin-coated magnetic beads were loaded into inlet 3 while SYTO 64 and biotinylated 1 kbp dsDNA were loaded into inlets 5 and 6. Inlets 1, 2, and 4 were loaded with 1xPBS buffer to aid in flushing the chip. Samples were combined in the central mixing valves (13, 2, 7, 10) where they were mixed and incubated for the proper construct to be formed. After the fluorescently stained targets were captured onto the beads, a magnet was used to pull the beads down and 1xPBS was washed through the valves to remove any unbound targets. The magnet was then removed and the sample solution was then pushed on to optical detection. b) Fluorescence time domain trace illustrating peaks observed from fluorescently labeled bead constructs. c) Fluorescence time domain trace resulting from negative control experiment conducted without dsDNA targets illustrating no false positive detections.

Fig. 5.4 Specific Zika assay detection. 1 μm streptavidin-coated magnetic beads with biotinylated capture probes, AlexaFluor 594 fluorescent probes, and Zika ssDNA

targets were loaded into inlets 3, 5, and 6, respectively. Assay reagents were brought into the central mixing valves (13, 2, 7, 10), mixed together, and heated to encourage hybridization. The completed magnetic bead constructs were pulled down using a magnet and 1xTE buffer was used to wash any unconjugated reagents away. After rinsing, the magnet was removed and the sample solution was pushed to the optical detection region.

EVs and a 40x objective couples the emission through a fluorescence filter and into an APD.

Fig. 6.3 Mode image of the excitation light guided through the solid-core excitation waveguide. The FWHM dimensions of the excitation mode were measured to be 3.74 μm x 5.08 μm.

Fig. 6.4 Fluorescence time domain traces from EVs stained with a) vFRed and b) SYBR Gold.

Fig. 6.5 Overlayed intensity histogram from detected events from the SYBR Gold and vFRed staining of EVs. The SYBR Gold distribution had a mean intensity of 76.2 counts/0.1 ms compared to the 26.4 counts/0.1ms average observed from the vFRed staining.

Fig. 6.6 Integration of internet-of-things with programmable LOC allows for remote control of valve actuation on-chip through internet connectivity.

Fig. 6.7 Context-aware remote PBL-training using LoC systems. A) Training workflow. In the first lecture the students are taught the theory of LoC systems and their applications to pathogen detection. In the second lecture, the students are taught how to program LoC systems. Both lectures are taught in the students' native language. The students are then assigned a project detecting bacteria in water samples. They then complete the assignment, upload their code and receive feedback. The LoC system is then run with their code and the data is produced, analyzed and returned to the students.

Fig. 6.8 Lab-on-chip device integrating sample preparation with optical detection.

Fig. 6.9 Example of redacted skeleton code given to students as homework. Commands: "c" = close, "o" = open, "w" = wait.

Fig. 6.10 Example fluorescence time domain trace resulting from optical detection of fluorescently stained E. coli. Each peak indicates a detected bacterium.

Fig. 6.11 Context-aware PBL led to a higher interest in LoCs. A) Self-reported interest in learning more about LoCs. B) Perceived applicability of LoC's in biotechnology before and after the program. C) Perceived difficulty of using LoCs before and after the program. D) Perceived performance of LoCs as compared to traditional laboratories. E) Perceived ease to learn to use of LoCs as compared to traditional laboratories. F) Perceived main advantage of LoCs in biotechnology. G) Students' interest in having a LoC-specific course in their degrees. H) Self-reported interest to enroll in LoC-specific courses. Pre-course n = 42. Post-course n = 28.

Fig. 6.12 Program evaluation and prospects of careers in bioinformatics and computational biology. (A-O) Program evaluation showing the distribution of students' responses. A) Evaluation of the theoretical component of the program. B) Evaluation of the programming assignment. C) Perception of the usefulness of the programming assignment to solidify concepts. D) Perception of the usefulness of the call with investigators to receive feedback on programming assignments. E) Perception of value of the program for academic goals. F) Perception of value of the program for professional goals. G-O) Program evaluation showing increased interest in

programming and bioinformatics. G) Comfort in completing programming assignment. H) Perceived relevant of assignment to students' degrees. I) Importance of using context-aware projects in teaching. J) Perceived applicability of LoCs in teaching programming. K) Students' recommendations to their peers. L) Self-reported effects on motivation to learn to program. M) Self-reported effects on feelings toward programming. N) Student's perceptions on whether their degree should have a programming course. O) Comparison of intent to enroll in a programming course before and after this program. Pre-course n = 42. Post-course n = 28.

Abstract

INTEGRATED OPTOFLUIDIC PDMS BIOSENSOR DEVICES

by

Tyler Sano

Recent epidemics such as Zika and SARS-CoV-2 have demonstrated the vital need for novel sample-to-answer biosensors that enable rapid diagnoses to reduce impacts of future disease outbreaks. Additionally, it is essential that these new biosensors remain cost-effective and progress ultimately towards a complete point-of-care (POC) device, enabling access to high quality diagnostic options in developing countries where disease outbreaks are far more devastating due to lack of resources and aid. Optofluidics provides unique advantages to address this challenge. By combining the integration of photonic components with the ability to control nanoliter scales of fluids, multiple functionalities that would usually require an entire laboratory can exist in the same chip. Developing these devices establishes a pathway to point-of-care devices that can democratize infectious disease screening. By fabricating these devices on polydimethylsiloxane (PDMS), even more advantages can be exploited through rapid prototyping of novel devices. Furthermore, the advancement of organ-on-chip studies provides another avenue by which optofluidic biosensor devices can be used to investigate secreted biomarkers and inform on organ health and development. Within this thesis several PDMS-based optofluidic devices are presented. The first device demonstrated an on-chip distributed feedback laser using Rhodamine 6G dissolved in

ethylene glycol that had a central lasing wavelength of 574.6 nm and a bandwidth of 1.08 nm. The threshold fluence of this laser was determined to be 52.7 µJ/cm^2. A second DFB laser using 4-(dicyanomethylene)-2-methyl-6-(4-dimethylaminostyryl)-4H-pyran (DCM) dissolved in dimethyl sulfoxide (DMSO) was then added to demonstrate spatially multiplexed fluorescence sensing. This second laser had a lasing wavelength of 656.5 nm, a FWHM of 1.73 nm, and threshold fluence of 307.6 µJ/cm^2. A complete all-in-one lab-on-chip (LOC) system is then presented integrating the Rhodamine 6G laser with sample preparation and optical detection of Zika nucleic acids. Lastly, new directions for optofluidic biosensors are presented including educational outreach using remotely operated LOC devices to conduct fluorescence detection of *Escherichia coli* (E. coli) as well as optical detection of single extracellular vesicles secreted from cerebral organoids.

Acknowledgements

Firstly, I would like to thank my advisor, Dr. Holger Schmidt for his kindness and continued patience throughout my entire program, particularly having navigated such a unique situation with the pandemic. I am continually grateful for all of the sincere mentorship and assistance in preparing me to enter my next stages in life. Thank you also to Dr. Tom Yuzvinsky for the brainstorming sessions and constant research support. I would also like to acknowledge and thank my committee members, Dr. Marco Rolandi and Dr. Mircea Teodorescu, for their guidance and reviews of my dissertation.

I would also like to thank my peers I have had the pleasure of working with throughout my time here at UC Santa Cruz. Special thank you to Dr. Jen Black for her mentorship during my early days as PhD student. Thank you so much for both the technical and research discussions as well as the time spent outside of the lab on the beach and the many coffees shared.

To my parents and siblings, thank you so much for the endless support and constant encouragement to pursue my goals. To Izzy and Jeffery, thank you for your compassion and never-ending generosity throughout the years. To all of my friends, thank you for all of the laughs and good times. Last but most certainly not least, thank you to my best friend and wife, Sabrina, for your unconditional love and unwavering support while navigating this crazy part of our lives.

Chapter 1

Introduction

With the occurrence of multiple epidemics and pandemics in recent years such as Zika, Ebola, and SARS-CoV-2, disease and pathogen detection have become high priorities in public health care [1]. While incredible achievements in the field of medical diagnostics have been made to detect infections earlier and more precisely, many of these techniques are expensive and time consuming. Frequently, these techniques also require very large pieces of expensive lab equipment making them inefficient in quickly providing point-of-care (POC) diagnostics as well as lacking the ability to be utilized in more rural and developing regions. In response to this, there has been a large effort to develop biosensors that operate on a chip scale, increasing the accessibility of sensitive diagnostic devices that are not hampered by laboratory space, expensive equipment, or even experienced professionals to operate them. These chip-scale biosensors are designed to integrate essential lab functionalities into a single lab-on-chip (LOC) device. In doing so, progress is being continually made towards the

development of an effective POC diagnostic device that can democratize the access of quick sample-to-answer disease diagnostic solutions.

Optofluidics is a unique field of study that emerged from the combination of microfluidics and optics [2]–[4]. The combination of the two fields has brought forth a wide array of approaches to tackling modern day problems, most notably in the realm of disease detection and biosensing [5]–[7]. With the mass utilization of photo and soft lithographic processes, fabrication of chip-scale microfluidic channels and optical waveguides has become relatively easy. The manipulation of small volumes of fluid is necessary for the development of a useful POC device while the integration of photonic components on-chip enables optical detection modalities that are essential for a complete LOC system. This dissertation will highlight chip-scale optofluidic devices designed for integrated coherent light sources [8], [9] and the LOC biosensors resulting from their integration with assay preparation [10]. Furthermore, this dissertation will demonstrate the progression towards remotely operated LOC biosensors.

The recent concurrent onset of widespread influenza, respiratory syncytial virus (RSV), and SARS-CoV-2 had a massive effect on the daily lives of people throughout the world [11]. This coined "tridemic," demonstrated the reality that many rapidly evolving pathogens can exist at the same time. Additionally, several of the infections resulting from these viruses such as Zika and Dengue or influenza and SARS-CoV-2 can result in patients exhibiting very similar symptoms. These two factors prove why the development of diagnostic systems must focus on decreasing limits of detection and time-to-detection while including the ability to conduct multiplexed analysis [12]–

[14]. The ability to test a single sample for several different potential biomarkers is essential for physicians to make informed treatment decisions and combat early-stage infections. Additionally, development of these devices should continue to be conscious of being economically efficient to ensure that a high level of health care is accessible.

In addition to aiding in pathogen detection, chip-scale optofluidic biosensors can also be useful in other fields of study. Organoids are a miniaturized model of an organ that is grown in vitro that aids in studying some of the key structural components of the actual organ [15]. These organoids originate as stem cells and are differentiated into a desired cell type. Organoids can provide a vast array of new insights into the evolution of organs as well as modern day concerns such as cancer and tumor progression and growth [16], [17]. Given that organoids are a relatively new subject of study however, there have been relatively few studies on various markers of health that they secrete throughout their growth. Extracellular vesicles (EVs) are membrane enclosed particles that are secreted from cells. Microvesicles, exosomes, and apoptotic bodies are the three subtypes of EVs that are differentiated primarily based on a number of factors including size and content [18]–[20]. All of these subtypes of EVs serve different functionalities, but specifically in the case of exosomes, contain biomarkers that can potentially be used as indicators of cell health and growth [21], [22]. Optofluidics and on-chip biosensing present a precedented path to detecting these biomarkers [23]. Furthermore, PDMS-based optofluidics presents an excellent platform for integration of these biosensors into systems designed to grow and provide on-demand feedback of organoid health.

3

This thesis first presents a novel polydimethylsiloxane (PDMS)-based optofluidic dye laser using Rhodamine 6G dissolved in ethylene glycol in a fluidic distributed feedback grating cavity using a corrugated sidewall architecture [8]. This on-chip laser was demonstrated to be dynamically tunable using a pneumatic "lightvalve" that deforms the lasing cavity and attenuates the output power. Additionally, this DFB laser was demonstrated to be capable of exciting fluorescence from individual fluorescent microspheres in flow that were used as a proxy for a fluorescently tagged biomarker; an essential functionality in the development on an optofluidic LOC biosensor. This device was then expanded to include a second DFB laser in parallel that used 4-(dicyanomethylene)-2-methyl-6-(4-dimethylaminostyryl)-4H-pyran (DCM) dissolved in dimethyl sulfoxide (DMSO) [9]. The inclusion of a second DFB laser enabled multiplexed fluorescence detection. An all-in-one LOC device is then presented implementing the DFB laser in a PDMS-based device that also contained sample preparation via pneumatically actuatable valves enabling assay preparation on-chip [10]. Lastly, ongoing research in optical fluorescence detection of EVs that are derived from lab-grown neuronal organoids is presented.

Throughout this dissertation, research contributions that result in a PDMS-based optofluidic LOC system and progress towards the goal of a POC device capable of reducing or preventing the impacts of future viral outbreaks are presented. Chapter 2 outlines essential background for the text that follows. Additionally, Section 2.2.1 describes an educational outreach project conducted remotely with university students in Bolivia, demonstrating other applications of LOC technology such as the

4

democratization of high-level scientific and educational outreach. A novel optofluidic distributed feedback dye laser is presented in Chapter 3. This architecture is expanded to include a second laser and spatially multiplexed fluorescence sensing is demonstrated in Chapter 4. The DFB dye laser is then combined with previous work in developing an integrated PDMS sample preparation stage enabled by a series of pneumatically actuated valves. This complete LOC is then demonstrated in Chapter 5 through detection of fluorescently labeled Zika nucleic acids. Chapter 6 discusses ongoing research in using PDMS optofluidics to optically detect and analyze extracellular vesicles that are secreted by laboratory-grown organoids. Lastly, Chapter 7 summarizes the work presented within this thesis and examines potential capabilities and future goals for the devices demonstrated.

Chapter 2

Background

The focus of this chapter is to provide theory and context in the form of prior work for the text that follows through discussion of previous work and motivation. This chapter will additionally present work demonstrating the use of optofluidics and lab-on-chip biosensing implemented in fluorescence detection of individual bacterium in a remote project-based learning educational outreach program with university students in Bolivia.

2.1 PDMS Optofluidics

Optofluidics is a relatively new field existing at the intersection of microfluidics and on-chip photonics [4], [24]. Integration of the two fields enables a new generation of devices that interface optical excitation and analysis directly with fluidic samples [3], [25]. While microfluidics has been a well-studied field presenting avenues for sample preparation and analysis for many years, integration of planar optical components on the same channel revolutionized the sensing capabilities of a single

chip-scale device [3], [24]. Incorporating more complex microfluidic processing, however, benefited from hybrid platforms combining polymer-based fluidic processing modules with solid state photonic devices [26]. Eventually, optical waveguiding in polymer materials such as PDMS dramatically expanded the use of polymer-based chips from sample preparation modules to standalone optofluidic diagnostic devices [27]. Optofluidic technologies have been implemented on solid-state platforms [28] as well as on polymer-based materials such as polymethyl methacrylate (PMMA) [29] and PDMS [30], or some combination of the two platforms [31]. In particular, PDMS provides the benefits of its biocompatibility [32], optical transparency [33], mechanical elasticity [34], and comparatively easy to fabricate [35]. Compared to the solid-state counter parts, PDMS also has a lower refractive index. This allows for more simple, index-guided liquid-core waveguides to be fabricated as there are more commonly used solvents that have a refractive index higher than that of PDMS. Additionally, since PDMS is comprised of a mixture of a base and curing agent, this ratio is variable and can be used to fabricate devices and device layers with varying flexibility and elasticity. More importantly, the refractive index of PDMS can be varied by changing the base-to-curing agent ratio when mixing the PDMS, making it a prime polymer for developing optofluidic LOC devices [27].

2.1.1 Microfluidics

Microfluidics is an expansive field that has been demonstrated to be versatile in the manipulation and handling of small volumes of fluid using fluidic channels on

the scale of tens to hundreds of micrometers in width [36], [37]. Historically, microfluidics was heavily used in chemical synthesis and analysis [38], [39]. Currently, microfluidic technologies are expanding and are being used in progressing exciting new fields of on-chip science such as biosensors and organs-on-a-chip, aiding in fundamental studies of organ health and development. PDMS has been a well-established material used in microfluidics research as a result of the ease of fabrication and ability to rapidly prototype new device designs in a cost-effective way. Furthermore, PDMS is a biocompatible material with additional benefits such as mechanical elasticity. Advancements in increasing the resolution of 3D printing technologies has led to even more rapid fabrications of microfluidic channels and devices [40]–[43]. Soft-lithography remains the primary method for fabricating PDMS-based optofluidic devices and has enabled micron-scale fluidic channels to be fabricated, allowing for sample processing at nanoliter scales.

The flow dynamics within microfluidic channels is often characterized by the Reynold's number:

$$Re = \frac{\rho v D}{\mu}$$

where ρ is the density of the fluid, v is the mean speed, D is the diameter, and μ is the dynamic viscosity. Since most fabricated microfluidic channels are rectangular, this expression can be expressed as:

$$Re = \frac{4\rho v A}{\mu P}$$

where A and P are the area and perimeter of the rectangular channel. As a result of microfluidic channels have micron scale dimensions, their Reynold's numbers are <2000, which is the transition from laminar flow to turbulent flow. Laminar flow implies that particles flowing in the center of the channel will have the maximum speed and those flowing near the channel walls will have the minimum speed.

In LOC systems, microfluidics not only provides the samples to detection sites, but more importantly aids in the mixing of sample suspended in the reagents [44]. Given that fluids often experience laminar flow in microfluidic channels, two fluids that flow in parallel do not mix together. Therefore, more complex channels are necessary to ensure mixing does occur in specific situations such as assay preparation. This mixing can be done in a variety of different ways depending on device architecture and material composition. In line with core microfluidic principles, various channel geometries can be fabricated for mixing purposes [45]. Zigzag, corrugated serpentine channels, and intersecting channels have all been used to conduct reagent mixing. Additionally, biological assays have been demonstrated using droplet microfluidics [46]–[48]. In general, mixing channels in series present a solid foundation for combining fluidic samples but lack the ability to sequentially introduce reagents together and the versatility for being used for different assay protocols. Because of this, microvalve arrays are a useful tool in the development of a versatile microfluidic LOC biosensor [34], [49]. Chapter 5 will present a LOC biosensor where fluidic mixing and assay protocols are conducted using a programmable pneumatically actuated PDMS valve array.

2.1.2 PDMS Automatons

An essential function of a LOC biosensor is the ability to conduct assay preparation on-chip. As described in the previous section, mixing channels are convenient solutions for sample preparation, but lack the ability to conduct a wide array of complex assays requiring multiple sequential steps. Developments in lifting gate valve arrays called "automatons," based on the foundational work presented in [34] and [50] demonstrating PDMS-based microvalves and pumps, significantly improved the ability of on-chip sample preparation by allowing for active control of fluidic systems (Figure 2.1) [26]. In this hybrid implementation, a PDMS automaton was used to conduct the sample preparation before transferring the sample to a solid-state optofluidic biosensing device via connective tubing. Active fluidic control was provided through a custom control box that was used to actuate individual solenoid valves and apply positive and negative pressure to the on-chip lifting-gate valves.
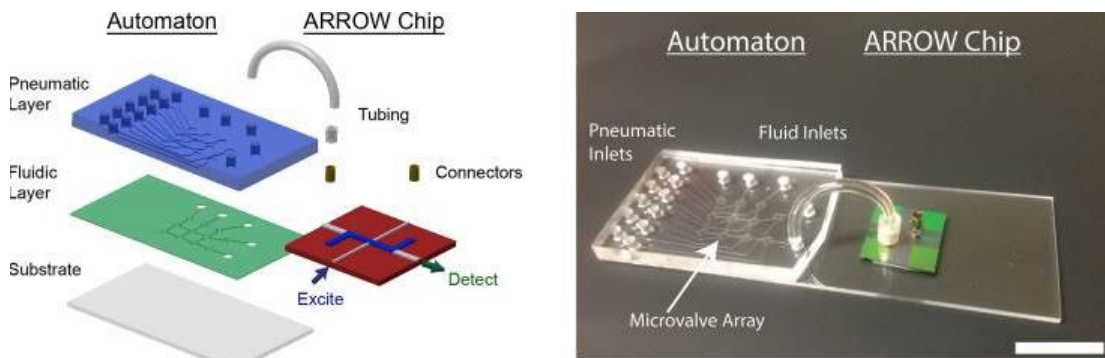
Figure 2.1. Hybrid integration of automaton and optofluidic biosensor device. a) Schematic of hybrid optofluidic device. b) A photograph of the assembled device (white scale bar represents 1 cm).

The automaton and optical detection integration was later advanced in [51] where a single PDMS device contained both the automaton state as well as a solid-core waveguide used to couple excitation light into the chip as seen in Figure 2.2. Fluorescence emission from excited targets was coupled off chip into an avalanche photodetector (APD).
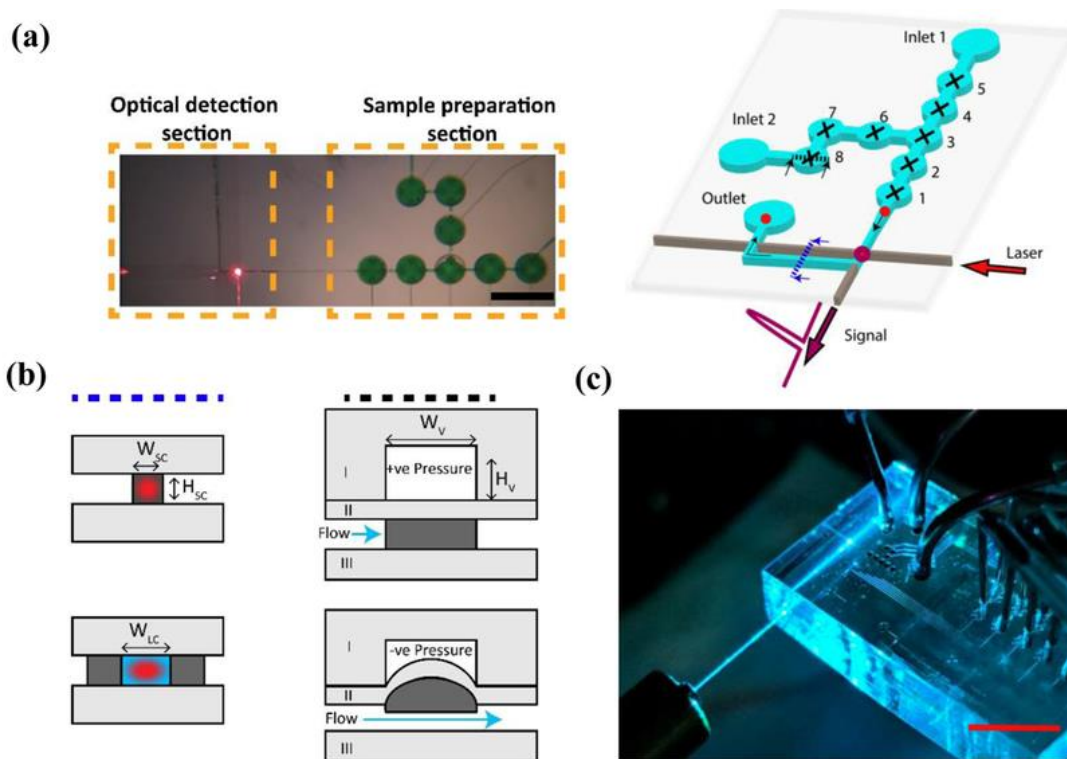
Figure 2.2. a) Left: Top-down camera image of the device with integrated sample preparation and optical detection (scale bar: 1 mm). Right: Schematic of the device where each of the 8 valves are individually actuatable to mix and push fluorescently labeled samples to the optical detection region. b) Cross-sectional schematics of the optical waveguides (left) and valve operation (right). c) Photograph of device (scale bar: 1 mm).

The illustrated device was shown to be capable of multiplexed detection of Zika nucleic acids and proteins using target-specific fluorophore binding on-chip. Chapter 5 will expand on the development of this device by incorporating an on-chip optofluidic

distributed feedback laser to provide a reconfigurable coherent excitation light while simplifying the optical coupling required.

2.1.3 PDMS Waveguiding

Optical waveguiding is essential to the integration of photonic components on PDMS. In the scope of on-chip optofluidics, confining and guiding light allows for the concentration of excitation light to small detection regions in desired areas of a device. Waveguiding in PDMS specifically is achieved through total internal reflection (TIR). TIR waveguiding is a phenomenon that occurs when light enters a waveguide at an angle larger than a critical angle and the refractive index of the core material is greater than that of the surrounding cladding:

$$n_{core} > n_{cladding} \tag{2.1}$$

This condition comes about as a result of Snell's law, which describes the relation of the angle of refraction to the angle of incidence given the refractive indexes of two adjacent materials.

$$n_{core} sin\theta_1 = n_{cladding} sin\theta_2 \tag{2.2}$$

If the condition for TIR waveguiding is met, there exists a critical angle (θ_c), determined by the angle of incidence when the angle of reflection is equal to 90°, beyond which light is reflected into the core material at an angle equal to the angle of incidence. Using angle laws and assuming a straight waveguide, any light that meets

this condition will continue to be confined within the waveguide such as shown in Figure 2.3.

$$\theta_c = \sin^{-1}\left(\frac{n_{cladding}}{n_{core}}\right) \tag{2.3}$$

PDMS is fabricated by mixing a base and curing agent together in an aqueous solution before curing in an oven to create a solid material. By altering the ratio of the base to curing agent when mixing, the refractive index of the final product can be manipulated [27]. Using this information, we are able to fabricate solid-core waveguides where light is confined in two dimensions. In the vertical dimension, these waveguides can be thought of as slab waveguides. For solid-core waveguides, the core is comprised of 5:1 PDMS with refractive index 1.4170 and the cladding is composed of 10:1 PDMS with refractive index 1.4138.
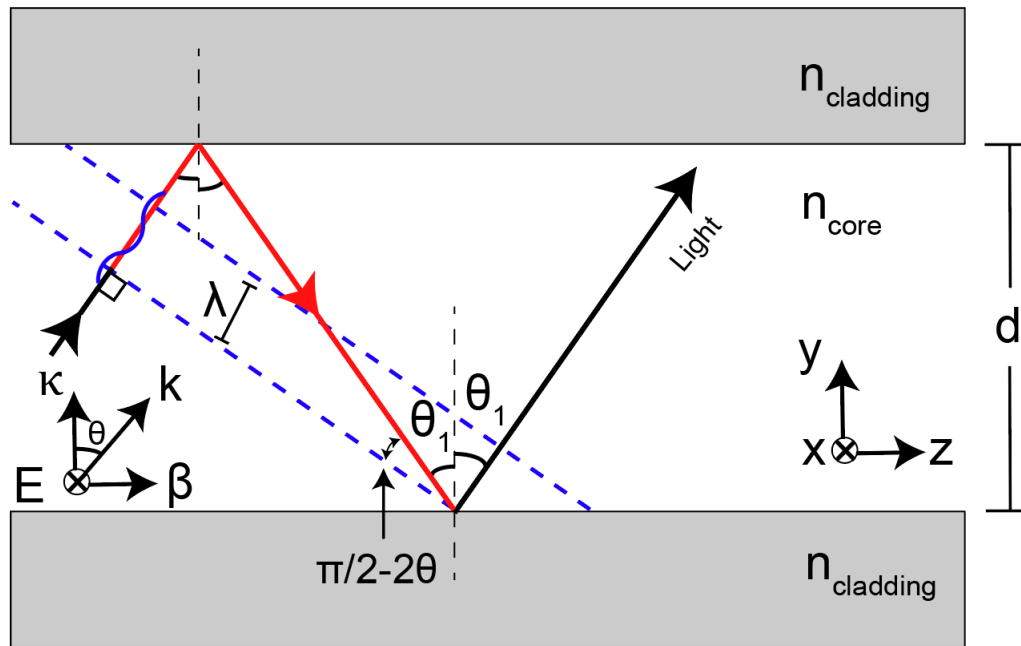
Figure 2.3. Propagation of light through a slab waveguide.

Slab waveguides are one of the most common and simple types of waveguides. The structure of a symmetric slab waveguide consists of a central layer, known as a core, with refractive index, n_{core}, located between two identical layers which are called the cladding, with refractive index, $n_{cladding}$ (Figure 2.3). Since slab waveguides operate using TIR, the refractive index of the core is, by definition, higher than that of the cladding layers. For waveguiding to be achieved, a propagating wave must constructively interfere with itself. Without constructive interference, the light will rapidly diminish via destructively interfering with itself. An electric field propagating in a slab waveguide can be visualized in Figure 2.3 where the phase change from the start to end of the red optical path must be an integer multiple of 2π. This can mathematically be expressed as:

$$\Delta\phi = m(2\pi)$$

where m is an integer. The phase change between the two points can be found by geometrically adding the lengths of the two segments:

$$\Delta\phi = k(2d\cos\theta) - 2\phi = m(2\pi)$$

Where k is the wave vector of the propagating coherent light, which is related to the wavelength of the light via $k = \frac{2\pi n}{\lambda}$, and d is the slab thickness. The 2ϕ factor accounts for the phase change resulting from the two internal reflections. From this equation, it can be seen that only one θ value and ϕ value can satisfy the equation for each m value. We therefore arrive at the waveguide condition:

$$\frac{2\pi n_{core} d}{\lambda} cos\theta_m - \phi_m = m\pi$$

For a step-index waveguide of width, w, a finite number of waveguide modes can be supported. The number of modes a waveguide is capable of supporting, M, is defined by:

$$M \leq \frac{2V - \phi}{\pi}$$

where V is the V-number, defined by:

$$V = \frac{2\pi w}{\lambda} \left(n_{core}^2 - n_{cladding}^2\right)^{1/2}$$

Therefore, the number of supported waveguide modes depends on the effective refractive index contrast between the core and cladding materials in the waveguide and can be manipulated to the point of becoming a single mode waveguide. In Chapter 3, we will discuss the manipulation of core refractive index via dilution of the liquid core solvent to achieve a liquid core DFB laser such that only the fundamental mode is supported.

2.2 Lab-on-chip Biosensing

Lab-on-chip biosensing is one field that has benefitted tremendously from the increased implementation of optofluidics [52]. Detection of desired bioparticles has largely been carried out in large quantities with expensive and bulky instruments in laboratories. Furthermore, by including as many laboratory functionalities as possible

in a single device, contamination and mishandling of samples can be reduced [53]. Microfluidics has allowed for increasingly smaller quantities to be manipulated and processed through a variety of different methods [54], [55]. This reduced quantity of reagents also leads to a reduction in the waste produced [56]. A primary laboratory function that can exist in LOC systems is sample preparation. The ability to conduct complex assays on-chip can dramatically reduce the amount of laboratory equipment needed for disease diagnostics [31], [51]. In LOC biosensing, this ability to conduct sample preparation is necessarily combined with on-chip detection of biomarkers.

On-chip biosensing has been demonstrated through a number of different modalities including electrical sensors and optical sensors [57]. Utilizing chip-based sensing schemes allows for increased sensitivities to be achieved since the detection regions are much smaller. Electrical sensors such as solid-state nanopores have the advantage of being able to detect label-free samples, therefore excluding fluorescence labeling assays generally found in optical sensors [58]. The downside to this type of sensor, however, is the inability to specifically correlate a detected signal to a specific biomarker without prior purification steps. This can be alleviated in aptamer-based electrical biosensors where target-specific binding between bound aptamers or antibodies and biomarkers leads to a current signal in the device [59]–[61], but this technique becomes harder in multiplexing schemes and does not scale well compared to optical biosensing counterparts. Label-free, aptamer-based binding can also be used in optical biosensors that detect the presence of biomarkers through surface plasmon resonance (SPR), however, multiplexing capabilities are, again, more complex. Label-

free optical sensing can also be employed in interferometric sensing where changes in refractive index of fluidic samples are monitored [62]. Fluorescence-based optical biosensors akin to flow cytometers, where fluorescently labeled analytes pass through a laser excitation spot, possess greater multiplexing capability resulting from the ability to selectively tag different biomarkers with an array of different fluorescent labels [12] as well as the ability to reach single molecule sensitivities [5]. In fluorescence-based optical sensors, a coherent excitation source is necessary to excite fluorescent labels. This laser excitation can be supplied by externally coupling a laser to the chip, however a number of on-chip lasers have been demonstrated that provide unique advantages on-chip for biosensing applications and will be discussed in Section 3.1.

The combination of complex microfluidic structures and high throughput biosensing paves a clear road to LOC systems [63]–[66]. Generally, the desired components of LOC symptoms are sample introduction, mixing and reaction, and analyte detection [67]. Various LOC devices have been demonstrated to be able to detect a range of biomarkers using fluorescence signals activated by biomarkers binding to aptamers [68], [69] as well as through Raman spectroscopic detection [70]. Additionally, colorimetric spectroscopy has been demonstrated in a LOC environment [71]. Notably, fluorescence detection at single molecule sensitivities has been demonstrated using a PDMS-based biosensor with an integrated sample preparation stage using pneumatically actuatable valves [51].

This thesis presents two types of chip-scale optofluidic devices fabricated entirely of PDMS in sequential development of an optofluidic LOC biosensor. Chapter

17

3 will discuss the first device which demonstrates optical sensing using a novel on-chip light source to detect fluorescent beads as a proxy for a fluorescently labeled biomarker. This device is then expanded on in Chapter 4, which presents a second device to include a second on-chip light source to demonstrate spatially multiplexed detection of two different fluorescent beads. The on-chip light source is combined with a previously demonstrated sample preparation platform to complete a PDMS-based lab-on-chip biosensor that was used to detect fluorescently labeled Zika nucleic acids captured on magnetic beads which is presented in Chapter 5.

2.2.1 Fluorescence Biosensing

As described above, on-chip biosensing is often achieved through means of electrical or optical detection methods. Optical detection schemes have the benefits of being selective and allow for expansive multiplexing techniques. A primary modality of optical biosensing is accomplished by employing laser-induced fluorescence.
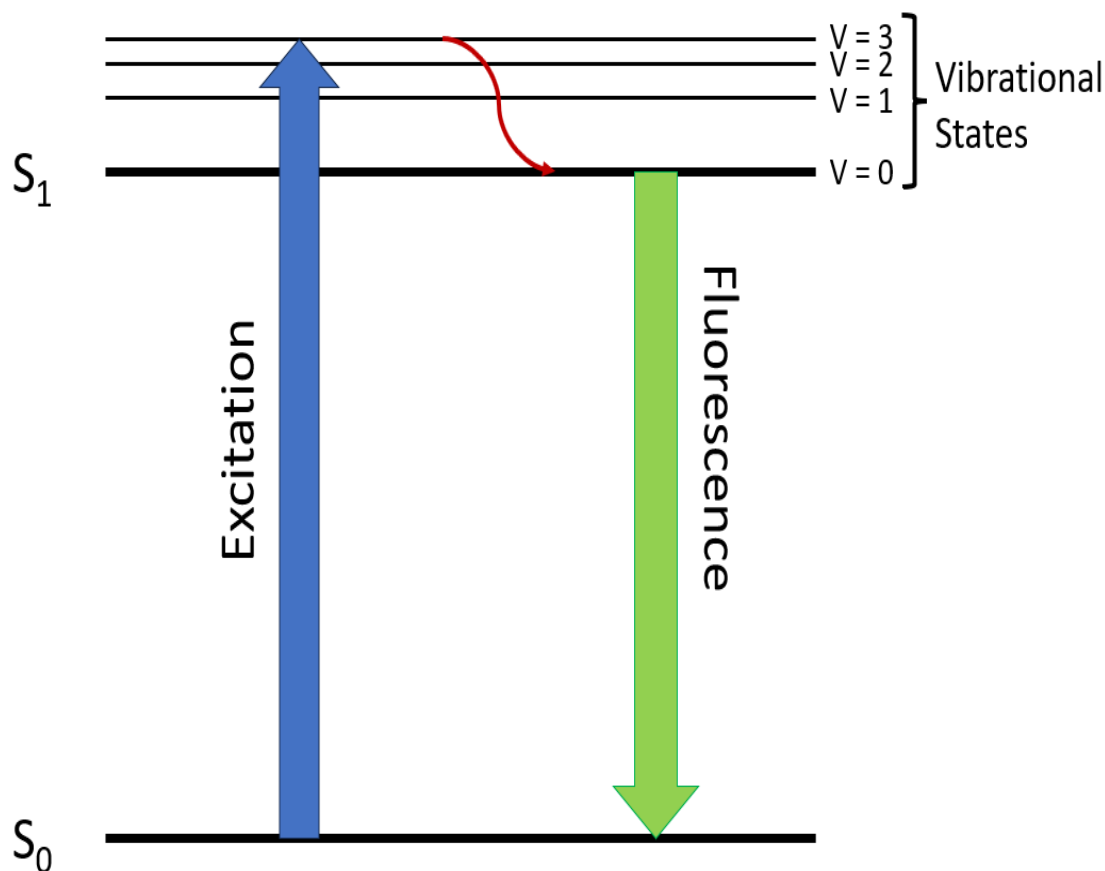
Figure 2.4. Energy diagram of laser-induced fluorescence. Absorption of a photon from a laser excites an electron from the ground state (S_0) to the excited singlet state (S_1, 3). Non-radiative decay relaxes the excited electron to the lowest vibrational energy state, (S_1, 0). A fluorescence photon is emitted as the electron relaxes to the ground state.

Fluorescence is a phenomenon that occurs when an electron in an excited vibrational singlet state emits a photon as it relaxes down to the ground state. In laser-induced fluorescence specifically, a fluorescent dye molecule is selected for having a specific energy gap between the ground and excited state that matches the energy of an excitation laser (Figure 2.4). When an excitation photon is absorbed, an electron is excited from the ground state (S_0) to a vibrational band in the excited singlet state, in

this case (S_1, 3). The excited electron quickly relaxes to the lowest vibrational state (S_1, 0), typically occurring on a timescale of picoseconds. Finally, the electron returns down to the ground state and emits a photon. Because of this relaxation, the emitted fluorescence photon will have less energy than the absorbed photon. This decrease in energy is known as the Stokes shift. In optical biosensing, this emitted fluorescence photon is captured as a fluorescently labeled analyte passes through a detection region where it intersects with laser excitation.

A massive variety of fluorescent dyes are now readily available commercially to allow for fluorescence detection using a host of different excitation wavelengths and a wide variety of applications. Fluorescent dyes can be functionalized to preferentially bind to specific molecules such as nucleic acids and lipids for specific sensing applications. In this thesis, detection of fluorescently stained polystyrene microspheres, E. coli, and extracellular vesicles will be presented. Additionally, dye molecules can be conjugated onto nucleic acid sequences. This thesis will also present specific fluorescence detection of Zika nucleic acid through hybridization of functionalized fluorescent probes onto target nucleic acid sequences.

Chapter 3

Optofluidic Distributed Feedback Dye Laser

The field of lab-on-chip biosensors aims to develop chip-scale devices capable of combining all necessary laboratory functionalities that are used for detection of desired biomarkers. A critical module of a lab-on-chip biosensor is the method of detection. In the case of an optical biosensor, a coherent excitation light source is preferred. In most cases, external lasers are coupled to chip-scale biosensors via an optical fiber aligned to an on-chip waveguide. This coupling can be extremely tedious and sensitive to the external environment. On-chip lasers offer the advantage of being coupled directly to the detection region and therefore require no extra alignment beyond alignment of the pump source [72], [73]. Section 3.1 will discuss various approaches to development of on-chip optofluidic lasers. Section 3.2 will discuss the specifics of a novel all-PDMS distributed feedback dye laser design. Section 3.3 will present results of laser characterization as well as fluorescence detection experiments

conducted with this device. Finally, Section 3.3.4 will describe the integration of the DFB laser with a pneumatic "lightvalve" enabling tunability of DFB laser output power.

3.1 Optofluidic Lasers

As mentioned above, a crucial component of lab-on-chip optical biosensors is a coherent light source. On-chip optofluidic lasers provide a host of reconfigurable advantages in addition to their direct integration to the chip. Typically, a fluorescent dye is dissolved into a solvent that is then flowed through an optical pump laser [72]. Since optofluidic lasers rely on a fluidic gain medium, various dyes can be used to generate a wide range of excitation wavelengths. Additionally, by varying or manipulating the solvent that the dye is dissolved in, the resonant wavelengths in the cavity can be tuned.
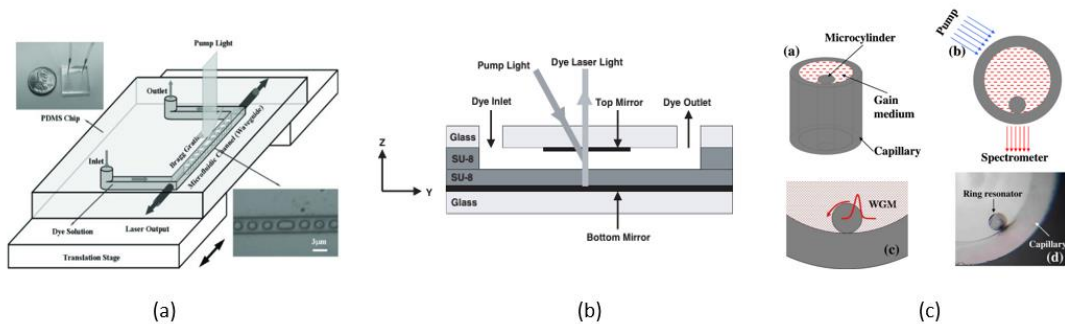
Figure 3.1. Previously demonstrated optofluidic dye laser geometries: a) Distributed feedback dye grating [74], b) Fabry-Perot cavity [75], and c) optofluidic ring resonator [76].

A wide variety of lasing geometries have been used to demonstrate on-chip optofluidic lasers including Fabry-Perot cavities [75], [77], droplet arrays [78], ring resonators [76], and distributed feedback (DFB) cavities [79]–[84] (Figure 3.1). Fabry-

Perot cavities provide a simple lasing cavity but require a very short cavity length to avoid high multimode lasing resulting from a small spacing between resonant wavelengths, or free spectral range (FSR). Droplet arrays provide a unique advantage of being able to dynamically change cavity properties by virtue of changing droplet spacing, but in general require more complex fluidic schemes to maintain droplet generation. Distributed feedback lasers use periodic refractive index contrast to generate optical feedback and lasing and have been used to demonstrate low threshold, single mode lasing in optofluidic implementations [81]. Optofluidic DFB cavities have furthermore been demonstrated to be versatile when implemented on deformable materials such as PDMS where the grating period can be mechanically altered to tune the lasing wavelength of the cavity [74]. Using these geometries, fluidic lasing emission has been demonstrated both out-of-plane as well as in-plane. For the purpose of incorporating the optofluidic laser with on-chip components in a planar device architecture, it is generally more useful for laser emission to be in-plane. In this thesis, we present a novel DFB laser geometry that uses a corrugated sidewall structure to introduce the required alternating effective refractive indexes.

3.2 Device Design

DFB lasers follow the Bragg condition required for reflections occurring in periodic refractive index layers:

$$2n_{eff}\Lambda = m\lambda_m \qquad (3.1)$$

In the Bragg condition, m is an integer number defining the Bragg order. Each corresponding λ_m specifies the resonant wavelength of the given Bragg order. The grating period is represented by Λ and n_{eff} is the effective refractive index.
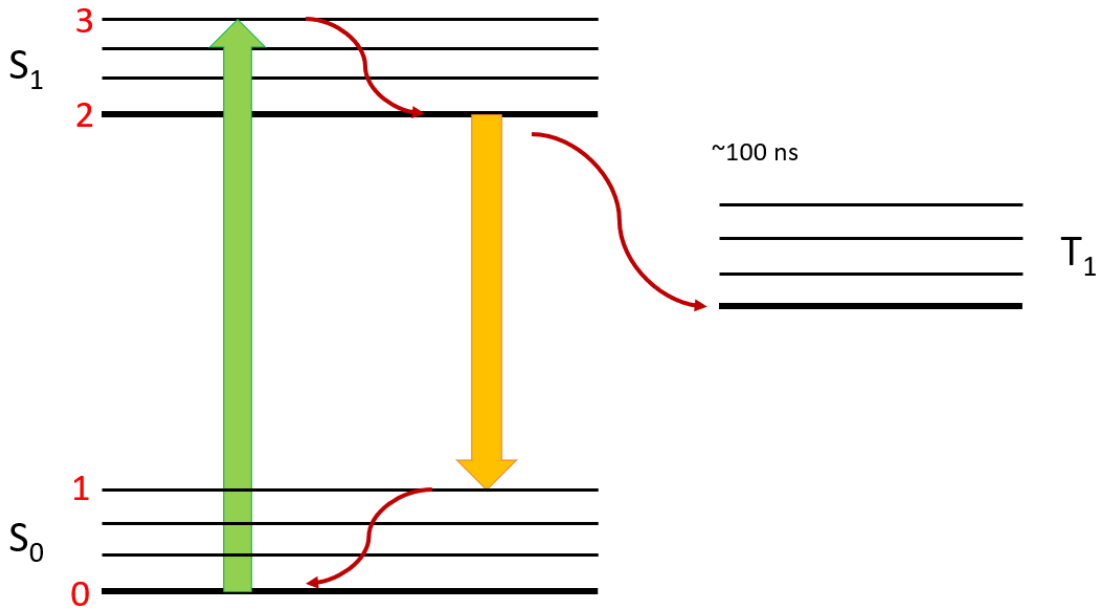
Figure 3.2. Four-level Rhodamine 6G lasing scheme.

The majority of optofluidic dye lasers cited above use Rhodamine 6G dye as the gain medium because of its high quantum yield and compatibility with a range of solvents [85]. Rhodamine 6G lasing is achieved, as with most dye lasers, in a four-level lasing system (Figure 3.2). In an ideal classical four level lasing model, electrons are excited from the ground state (S_0, 0) to an excited singlet state, (S_1, 2). The electrons very quickly relax to the lowest vibrational energy state of the excited singlet state (S_1, 0) via nonradiative decay on a picosecond timescale. This energy state is metastable and forms the upper laser level. The excited electrons relax to the lower laser level (S_0, 3) and emit photons with energy, $E = h\nu$. The electrons then relax rapidly, on the order

24

of picoseconds, to the ground state through nonradiative decay where they can be excited again. The long-lived upper laser level is essential for generating population inversion where the concentration of excited electrons is greater than that in the lower laser level. In reality, however, there can exist intersystem crossing where excited electrons transition to a dark triplet state, which has a detrimental effect on lasing capabilities by parasitically trapping dye molecules. This dark triplet state effect is minimized by using pulsed pump sources with pulse durations typically ranging in the $0.5 - 10$ nanoseconds so that they are much shorter than the intersystem crossing time. Additionally, triplet state effects can also be reduced by constantly replenishing the available dye molecules as well as various triplet state quenchers, which is highly necessary in the case of continuous wave (CW)-pumped dye lasers.

Rhodamine 6G has a peak emission near 580 nm with a bandwidth of roughly 50 nm. To prevent multiple lasing peaks within the emission spectrum, a DFB cavity with an FSR greater than 50 nm is ideal. For these experiments, the DFB grating had a period of $\Lambda = 8$ µm and corrugation depth of $d = 2.5$ µm, corresponding to a Bragg order of $m = 39$. While smaller grating periods are advantageous to decrease the Bragg order and increase the reflectivity of the grating, the grating period was limited by the resolution of the fabrication process. A device schematic is shown in Figure 3.3. Solid-core and liquid-core waveguiding was enabled on this device. As described in Section 2.1.3, solid-core PDMS waveguides were enabled using a 5:1 PDMS high refractive index core, with 10:1 low refractive index cladding. Since laser emission from the DFB laser emits in the $+\hat{z}$ and $-\hat{z}$ directions, solid-core waveguides were used to guide

emission both off chip for analysis of laser characteristics as well as to an orthogonal intersection with a fluidic analyte channel. Liquid-core waveguiding is enabled in the DFB grating where a solvent with a higher refractive index than the surrounding PDMS was used to maintain TIR waveguiding. The analyte channel was used to flow fluorescently labeled biomarkers which were excited by the DFB laser emission.
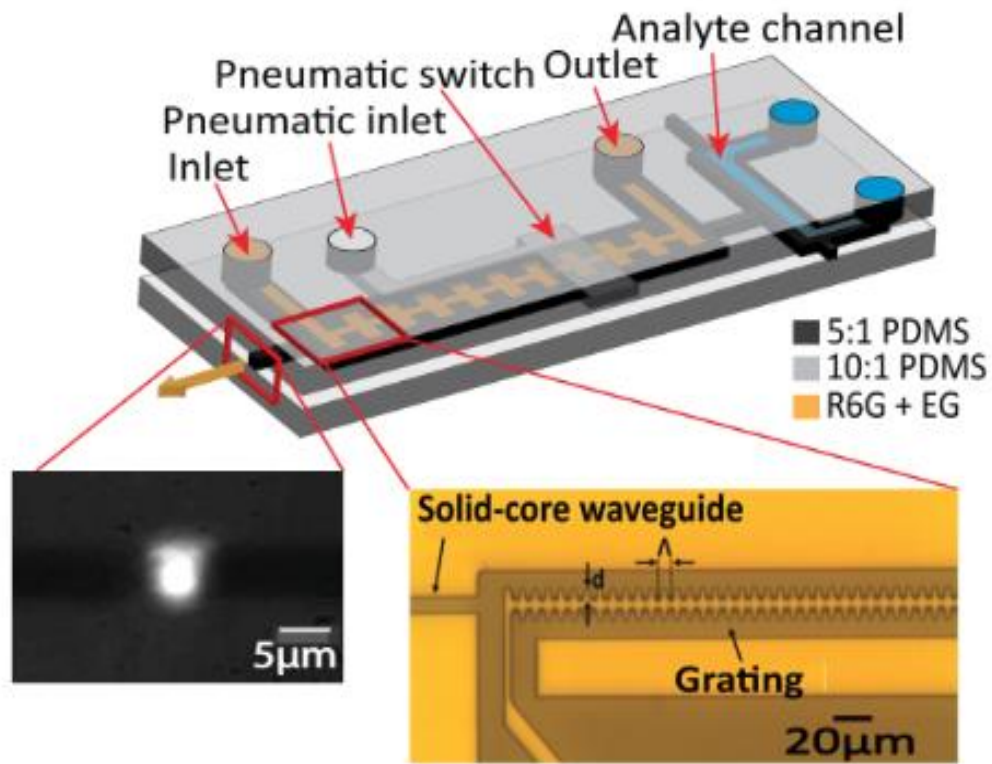
Figure 3.3. Device schematic of all-PDMS optofluidic dye laser. Bottom left image shows the fundamental lasing mode coupled to free space using a 40x objective. The Bottom right image is a microscope image of the DFB grating and the solid-core waveguide used for coupling DFB laser emission.

Theoretical modeling of the device's transmission spectrum was carried out using Rouard's Method, which effectively simplifies the three-dimensional optofluidic grating into one dimension using the effective refractive index of wide and narrow

grating corrugations [86]. The grating was then simulated as a stack of alternating dielectric layers with a thickness of $\Lambda/2$ and a total of $2L/\Lambda$ transmission matrices. Using this, the transmission as a function of wavelength was determined to find the resonant wavelengths in the relevant wavelength span of $550 - 650$ nm (Figure 3.4).
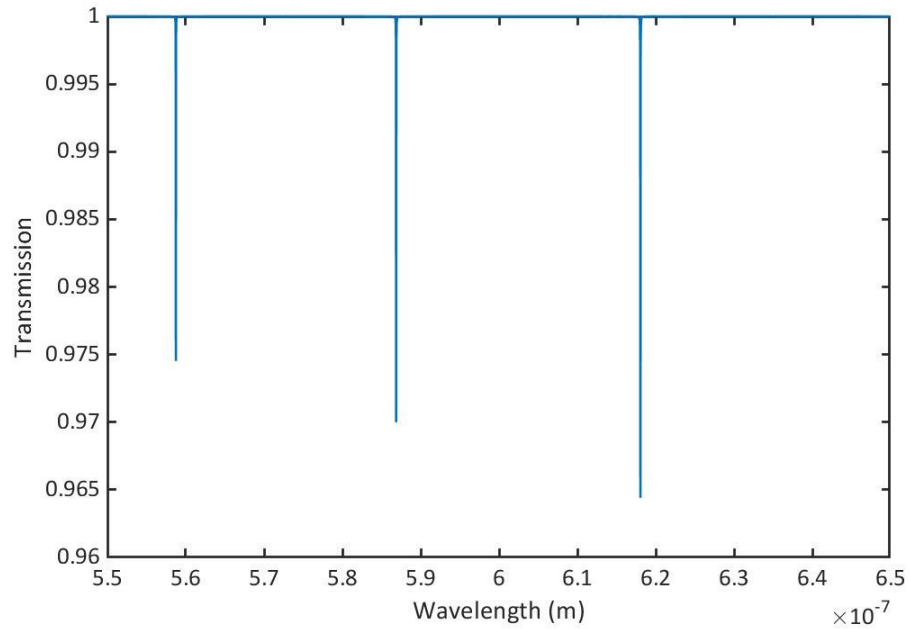
Figure 3.4. Simulated transmission spectrum for a device with $\Lambda = 8\ \mu m$ and corrugation depth of $d = 2.5\ \mu m$ within a wavelength span of $550 - 650$ nm.

3.2.1 Fabrication
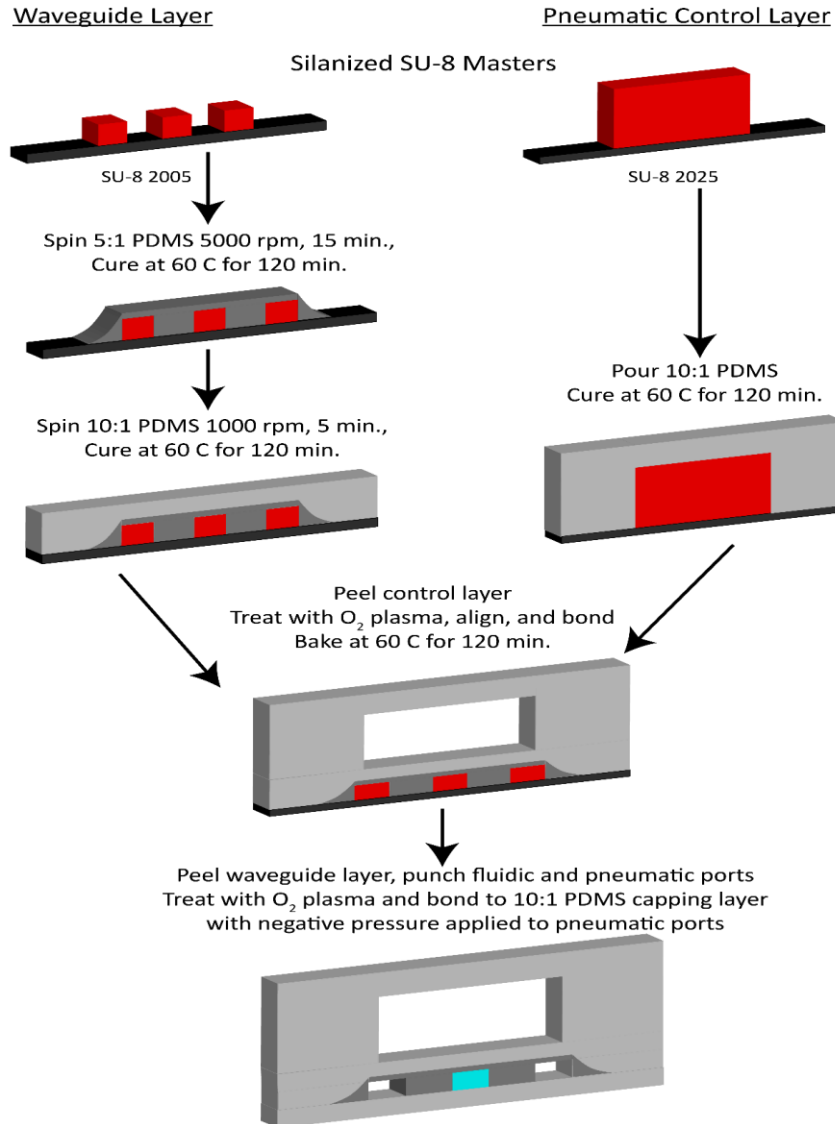
Figure 3.5. PDMS fabrication procedure.

In this chapter, we present two variations of an optofluidic DFB laser. The first design serves as the baseline device with a DFB laser integrated with an analyte channel. The second device incorporates a pneumatic "lightvalve" which uses pneumatic actuation to physically deform the lasing cavity and enable the ability to attenuate the

lasing power emitted from the DFB laser into the analyte channel. The incorporation of the light valve requires an additional step in the fabrication process to enable a multilayer device structure.

Soft lithographic fabrication of these PDMS devices first required standard photolithography procedures to create an SU-8 template. Two silicon wafers were first cleaned and dried in a 60 °C oven overnight to ensure a dry, contaminant-free surface. The silicon wafer is first oxygen treated in a reactive ion etching (RIE) system for 15 minutes. Directly following the oxygen treatment, either SU-8 2005 (waveguide layer) or SU-8 2025 (pneumatic layer) negative photoresist (Microchem) was poured onto the wafer before loading the wafer into a spincoater. The SU-8 spin and baking procedures are outlined in Appendix A. After the SU-8 was spun on and underwent a pre-exposure bake, the coated wafer is spun at 700 rpm while a syringe was used to apply acetone and conduct edge bead removal to alleviate any thicker SU-8 resulting from the spincoat. The wafer is then loaded into a mask aligner for UV exposure through a chrome mask to cure desired SU-8 features. For the waveguide SU-8 2005 layer, a total UV dosage of 69.8 mJ/cm^2 was applied. The exposure time was adjustable to maintain a constant dose with variable UV lamp powers. For the pneumatic layer, the total UV dosage was raised to 146.3 mJ/cm^2. The exposed wafers then underwent a post-exposure bake protocol outline before being developed using SU-8 developer. The final SU-8 master product was checked for faults before hard baking.

Following the production of the SU-8 template, standard soft lithography processes outlined in [35] are used to fabricate each PDMS device. Recall from Section

2.1.3 that varying base-to-curing agent ratios are used for fabricating PDMS waveguides. For a waveguide features, 12 g of 5:1 PDMS (Sylgard 184) was mixed together. For the pneumatic wafer, 55 g of 10:1 PDMS was mixed. Another 55 g of 10:1 PDMS was mixed for the blank capping layer to seal the fluidic channels. To ensure air bubbles in the PDMS are removed, the PDMS was placed in a desiccator for 2 hours. During this time, the silicon masters were silanized in a second desiccator to aid in a smooth separation of PDMS and silicon wafer. After degassing, the 5:1 PDMS was poured on the silicon master and the wafer was spun at 5000 rpm for 15 minutes. The PDMS is then cured in a 60 °C oven for 2 hours. For devices without a pneumatic layer, a PDMS-coated wafer was loaded into a circular acrylic mold and 10:1 PDMS was poured directly on top. This provides structural integrity to the device while also providing a low index cladding for the optical waveguides and a thicker layer to integrate fluidic reservoirs. Concurrently, the blank capping layer was also poured over a blank silicon wafer in another circular acrylic mold. After another 2-hour curing period, the waveguide layer is pealed from the silicon wafer and taped to maintain a clean surface. The locations of the fluidic reservoirs were then marked and punched using a 1 mm biopsy punch. Finally, the capping layer was peeled, and the tape was removed from the surface of the waveguide layer. The two surfaces were oxygen plasma treated in the RIE system for 30 seconds before being bonded and cured in the oven overnight.

For devices containing pneumatic "lightvalve" switches, a thin 10:1 PDMS layer was spun onto the waveguide layer following the curing of the 5:1 PDMS. In

parallel, 10:1 PDMS was poured onto the pneumatic silicon wafer which was loaded into a circular acrylic mold. After pouring, another acrylic slab with polygons cut out was slowly pressed on top. This provided a layer to anchor the pneumatic portion of the PDMS for the alignment procedure to follow. After curing, the pneumatic wafer was separated from the PDMS and loaded into a mask aligner (OAI Instruments) above the coated waveguide layer. After oxygen plasma treating the two layers, the mask aligner was used to position the pneumatic features above their designated locations on the waveguide layer. The layers were then brought into contact and cured before bonding with the capping layer as described above.

3.2.2 Experimental Setup
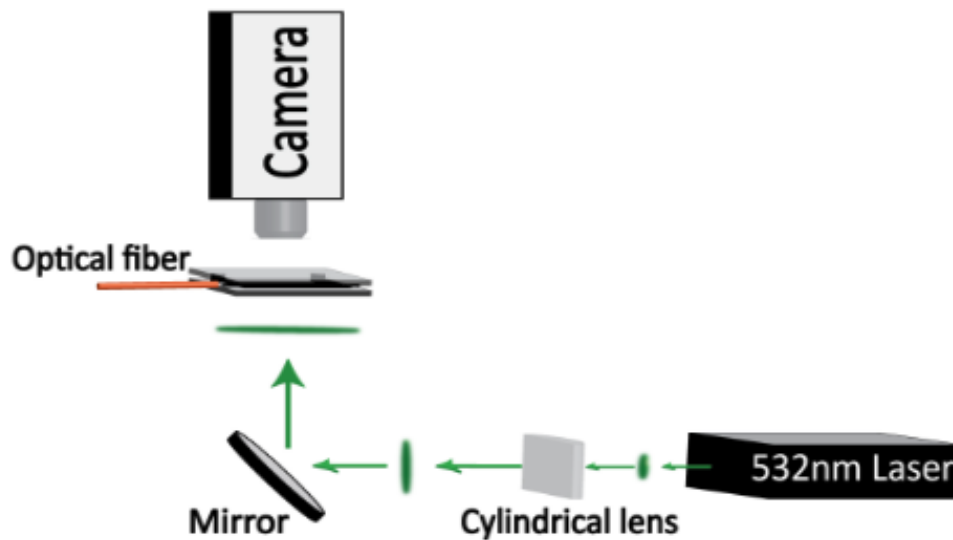
Figure 3.6. Experimental setup for DFB dye lasing. A pulsed 532 nm pump laser is focused through a cylindrical lens and aligned to the DFB grating via bottom-up excitation using a 45° mirror. A high-speed camera is aligned above the chip to aid in aligning the pump laser and as well as collecting fluorescence signals when aligned

above the excitation region in the analyte channel. An optical fiber or objective is aligned to the solid-core waveguide enabling for power and spectral analysis of the DFB emission.

A schematic of the experimental setup is illustrated in Figure 3.6. The pump laser used to excite the gain channel is a 1-4 kHz, 532 nm laser with a 0.5 ns pulse width (TEEM photonics, STG-03E-140). The gaussian beam of the pump laser was passed through a cylindrical lens to elongate and focus the beam along the gain channel. This was done to demonstrate the lowest lasing threshold and optimal lasing characteristics, but with a high-power pulsed pump source, beam shaping may not be necessary. Coupling of a single mode fiber to an on-chip waveguide has a tolerance of ≲ 1 μm whereas the alignment of the pump beam exhibits a 10x improvement with a tolerance of ~10 μm. As mentioned above, with a higher power pump source, the beam focusing could be further relaxed and the alignment tolerance could be as high as ~100 μm. A 45° mirror was used to direct the pump beam up through the bottom side of the chip and to the DFB grating. A camera (Andor Zyla, Oxford Technologies) was aligned above the chip to aid in alignment of the pump laser as well as collect fluorescence signals from the analyte channel. An optical fiber was also coupled to the solid core waveguide on-chip to allow for spectral and power output analysis. Vacuum was applied to the device via 1 mm metal tubing inserted into the outlets of the DFB grating channel and the analyte channel. This was essential for pulling biomarkers through the analyte channel as well as constantly resupplying the liquid-core DFB grating with fresh gain media to avoid photobleaching the Rhodamine 6G. Photobleaching is a phenomenon by which a dye molecule no longer emits fluorescence photons as a result

of chemical damage induced by pump photons. Therefore, by constantly resupplying the gain media, loss of output power as a result of photobleaching was avoided [87].

3.3 Results
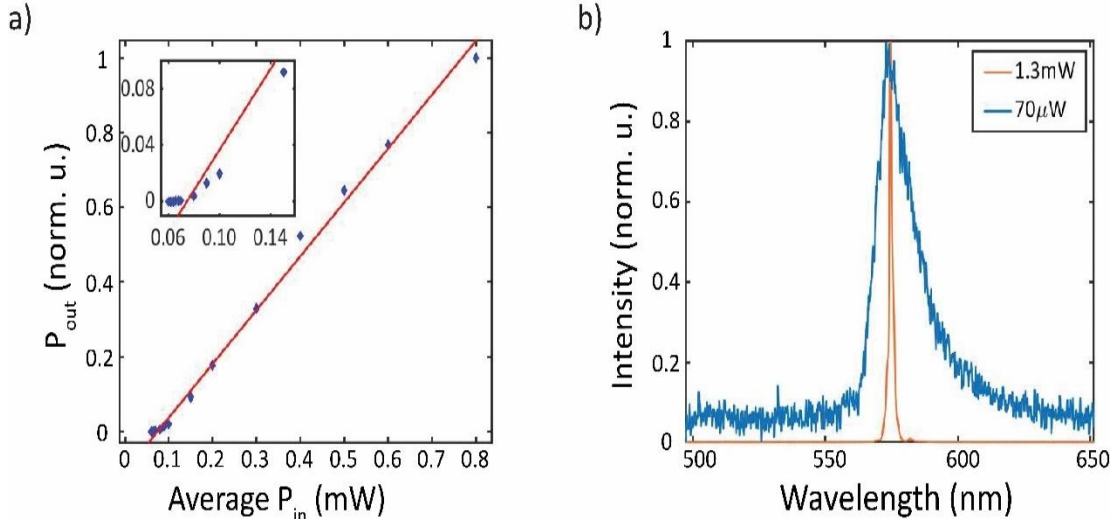
Figure 3.7. Characterization of Rhodamine 6G DFB laser. a) Normalized average output power as a function of average pump power shows are clear change in slope above threshold (inset). b) A broadband Rhodamine 6G amplified spontaneous emission (blue; average pump power: 70 µW) is shown when the DFB laser is pumped below threshold while strong spectral narrowing is seen when pumped above threshold (orange; average pump power: 1.3 mW) with a peak lasing wavelength of 574.6 nm and FWHM of 1.08 nm.

The optofluidic DFB dye laser used a gain medium of 5 mM Rhodamine 6G dissolved in a 15% DI water – 85% ethylene glycol solution. The results of the power series are shown in Figure 3.7a. Two linear regimes were observed, which is one indication of lasing behavior. The point at which the slope changes represented the lasing threshold whereby population inversion, the state in which there are number of electrons in the excited state is greater than those in the ground state, was achieved. A linear fit was applied to both and the intersection of the two was taken to be the

33

threshold value. Using this method, the threshold pump power was determined to be 87.9 µW. Typically, threshold pump fluence is used to compare dye laser performance (Equation 3.2), which is calculated using the beam area ($A = \pi \left(\frac{50\ \mu m}{2}\right)\left(\frac{4.25\ mm}{2}\right)$) and repetition rate of the laser (1 kHz):

$$F = \frac{Energy}{Area} = \frac{P_{threshold}}{A * RepRate} \tag{3.2}$$

This corresponds to a threshold pump fluence of 52.7 µJ/cm². Another characteristic of lasing behavior is spectral narrowing of the DFB laser when pumped above threshold (Figure 3.7b). As illustrated by the blue spectrum, the Rhodamine 6G amplified spontaneous emission (ASE) was observed when the DFB laser was pumped with a power below the threshold value. When the pump laser was increased above the DFB laser threshold, the DFB laser exhibited a central lasing peak at 574.6 nm with a 1.08 nm full width at half maximum (FWHM) narrowed spectrum. The corresponding output mode of the DFB laser was imaged using a 40x objective coupled to the chip facet (Figure 3.8). By integrating the intensity horizontally and vertically, the FWHM dimensions of the excitation mode was determined to be 4.1 µm x 7.1 µm.
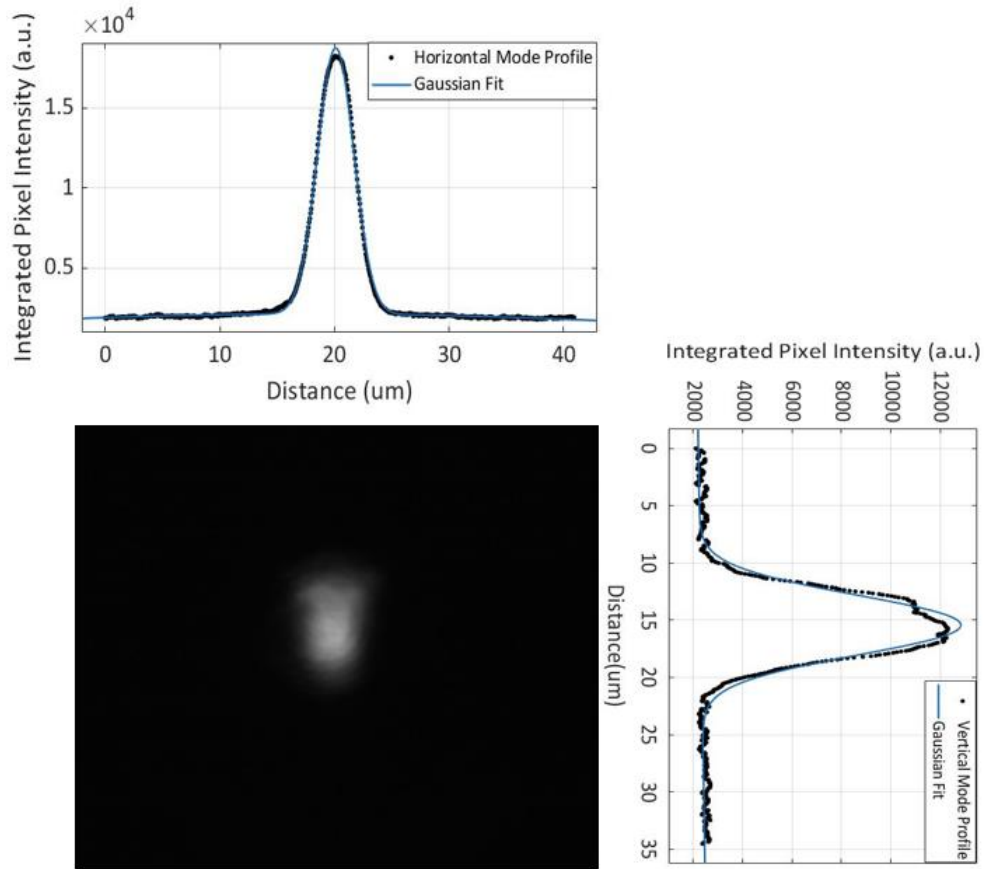
Figure 3.8. Camera image of the laser mode coupled into free space using a 40x objective aligned to the solid-core waveguide at the chip facet. The intensity was integrated horizontally and vertically to generate the horizontal and vertical mode profiles. The FWHM mode dimensions were calculated to be 4.1 μm x 7.1 μm.

3.3.1 Gain Optimization

Optimization of the Rhodamine 6G gain medium occurred through analysis of output power at 1.3 mW average pump power and lasing threshold while varying gain medium parameters. The first tested parameter was concentration of Rhodamine 6G. In general, an increase in dye molecule concentration leads to an increase in output power and decrease in threshold power. As seen in Figure 3.9a, as Rhodamine 6G dye concentration was increased, there was a decrease in the threshold power required for

lasing and an increase in the maximum output power at a pump power of 1.3 mW. When the concentration was increased to 10 mM Rhodamine 6G, however, the threshold continues to decrease, but there was an observed drop in the average output power due to the quantum yield of Rhodamine 6G suffering from aggregation of dye molecules [88].
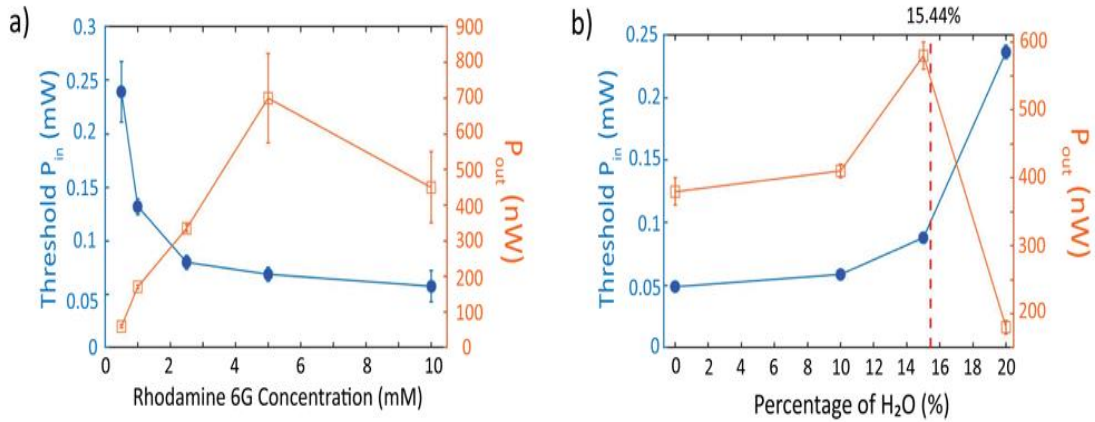
Figure 3.9. Optimization of gain medium. a) Threshold and output power at 1.3 mW pump as a function of Rhodamine 6G concentration. b) Threshold and output power at 1.3 mW pump as a function of percentage of DI water dilution of the ethylene glycol solvent.

The second optimization of the gain medium of the DFB laser was achieved through varying the refractive index of the gain medium. Recall from Section 2.1.3, since the number of propagating modes in the waveguide is scales with the refractive index contrast between the core and cladding materials, dilution of the liquid-core gain medium can be used to achieve a single propagating waveguide mode. If the refractive index of the core medium is reduced to a point below the refractive index of the cladding material, the TIR waveguiding is lost.
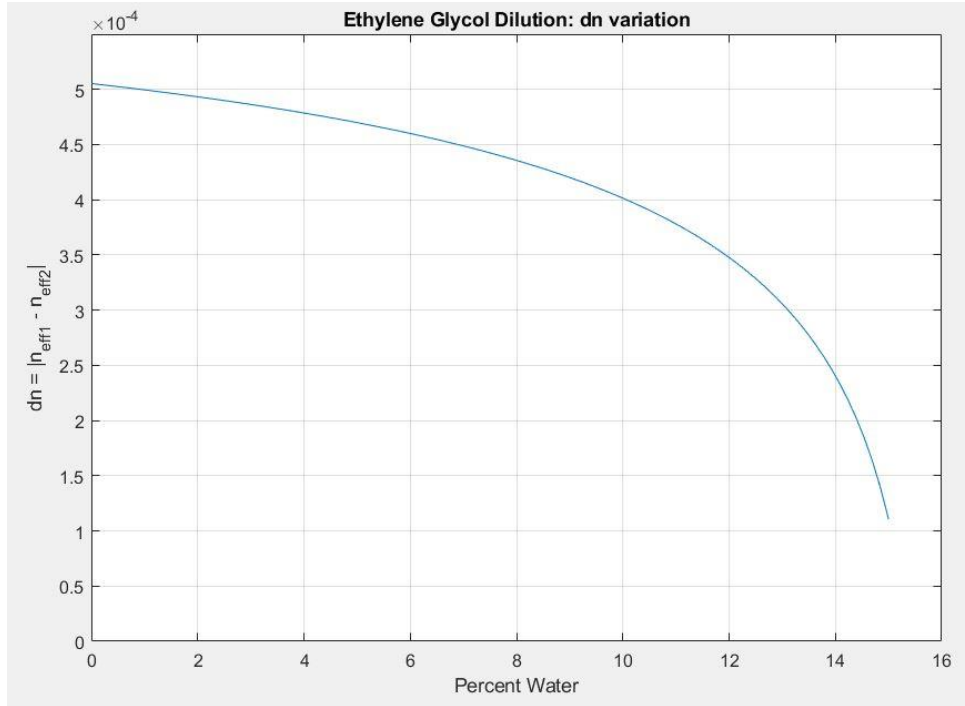
Figure 3.10. Effective refractive interest contrast as a function of dilution of the ethylene glycol solvent with DI water.

$$n^2 = 1 + \frac{A_1\lambda^2}{\lambda^2 - \lambda_1^2} + \frac{A_2\lambda^2}{\lambda^2 - \lambda_2^2} + \frac{A_3\lambda^2}{\lambda^2 - \lambda_3^2} \tag{3.3}$$

By using the Sellmeier equations (Equation 3.3) for water and ethylene glycol, the refractive index of the core can be predicted as a function of wavelength. The index of refraction of the core at a specific wavelength is taken to be the weighted average of the refractive index ethylene glycol and water, respectively, where the weights are defined by the percentage of water used. Using this method, the core refractive index was calculated to match that of the 10:1 PDMS cladding at a dilution of 15.44% DI water (Figure 3.10). To test this, the Rhodamine 6G was dissolved in an ethylene glycol and deionized (DI) water solution with 0%-20% of DI water. This corresponds to a dilution dependent refractive index of the core medium ranging from 1.4321 at 0% to

1.4174 at 15%. As expected, a peak in output power is observed at a dilution of 15% DI water, with a sharp decrease when the dilution was increased to 20% DI water due to the loss of TIR guiding (Figure 3.9b). Of note, as the percentage of DI water was increased, a marginal increase in the threshold was observed. This resulted from the decrease in reflectivity of the Bragg grating that comes with a lower contrast of refractive indexes. The Bragg grating resonance was maintained within the peak of the fluorescence spectrum due to the blue shift of the Rhodamine 6G fluorescence as a result of dilution [89]. Since the objective is to maximize laser power in the analyte channel for fluorescence detection, the tradeoff of higher lasing power for a higher threshold is still advantageous.

3.3.2 Threshold Analysis

To expand on this study, we compared the observed experimental threshold values with modeled threshold values. The dependence of the threshold on Rhodamine 6G concentration and refractive index of the core material can be theoretically modeled using the rate equations. In this study, the theoretical modelling follows the analytic method described in [90]. The laser cavity flux, $d\Phi/dt$, is defined using rate equations:

$$\frac{d\Phi}{dt} = c\left[n_2\sigma_{em}(\lambda_L) - n_0\sigma_{ab}(\lambda_L) - n_T\sigma_T(\lambda_L) - \frac{\gamma}{L}\right]\Phi \qquad (3.4)$$

where c is the speed of light, γ is the single-pass loss, L is the length of the liquid core cavity, n_0, n_2, and n_T are the concentrations of dye molecules in the ground state, excited singlet state, and triplet states, $\sigma_{em}(\lambda_L)$ is the emission cross section at the laser

wavelength, $\sigma_a(\lambda_L)$ is the absorption cross section at the laser, and $\sigma_T(\lambda_L)$ is the stimulated transition cross section at the laser wavelength. Typical values for each constant for Rhodamine 6G, assuming a pump wavelength of 532 nm and lasing wavelength of ~580 nm, can be found in Appendix B [91]. The rate of population change of excited molecules in the excited first singlet state is given by:

$$\frac{dn_2}{dt} = R_P + [n_0\sigma_a(\lambda_L) - n_2\sigma_{em}(\lambda_L)]\Phi - n_2 k_{ST} - \frac{n_2}{\tau_{sp}} \qquad (3.5)$$

where R_P is the lasing pump rate per volume, k_{ST} is the intersystem crossing rate, and τ_{sp} is the spontaneous emission lifetime. The pump rate is defined as:

$$R_P = \frac{n_0\sigma_a(\lambda_P)I_P}{h\nu_P} \qquad (3.6)$$

where $\sigma_a(\lambda_P)$ is the absorption cross section at the pump laser wavelength, I_P is the pump intensity, h is Planck's constant, and ν_P is the pump laser frequency. When a pulsed pump source is used, the pump pulse is shorter than $1/k_{ST}$. As a result, triplet state effects can be neglected [92]. Furthermore, if we assume that absorption of dye laser photons by dye molecules is low, the threshold population inversion is reduced to a function of the loss in the cavity:

$$n_{2th} = \frac{\gamma}{\sigma_{em}(\lambda_L)L} \qquad (3.7)$$

The threshold pump intensity is therefore expressed as:

$$I_{th} = \frac{\gamma h\nu_P}{\sigma_{em}(\lambda_L)\tau_{sp}Ln_0\sigma_a(\lambda_p)} \qquad (3.8)$$

39

where d is penetration depth of pump laser light into the gain cavity. Given that $d = 1/n_0\sigma_a(\lambda_P) = 8.7$ μm for a 5 mM Rhodamine 6G solution and that the pump light is not focused entirely into the grating, not all pump light is absorbed since the channel height is ~7 μm. The single-pass loss in a DFB laser is dependent on the reflectivity of the Bragg grating, radiation loss due to the high Bragg order, scattering loss from interface roughness, and reabsorption of DFB laser emission by Rhodamine 6G molecules. The threshold pump power is inversely proportional to the Rhodamine 6G concentration and proportional to the single-pass loss which is dependent on the refractive index of the liquid core gain medium.
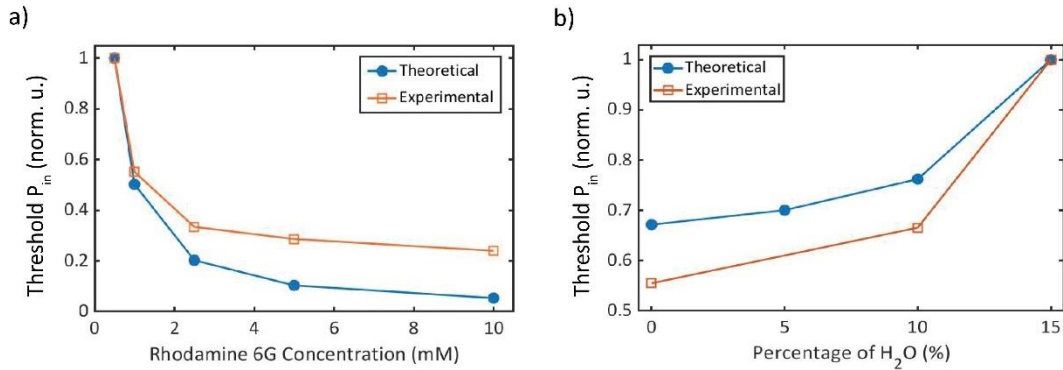
Figure 3.11. Comparison of theoretical and experimental lasing thresholds as a function of a) Rhodamine 6G concentration and b) percentage of water dilution of the solvent.

From Figure 3.11, the normalized experimental and theoretical threshold behaviors show very good qualitative agreement. The true experimental threshold pump powers are an order of magnitude higher than the theoretically predicted threshold pump powers. This discrepancy can be attributed to waveguide loss, out-of-plane scattering, and mode overlap loss in the liquid-core waveguide.

3.3.3 Fluorescent Bead Detection

Detection of fluorescent beads was used as a method of determining proof of concept. While this device was capable of being used with the aforementioned APD detection schematic, a more simplistic camera collection of the fluorescence signals was used. This alleviates the tedious APD alignment in addition to the removal of the fiber alignment of an external laser source. After aligning the pump beam to the DFB channel, the grating was filled with 5mM Rhodamine 6G dissolved in 15% DI water – 85% ethylene glycol. The camera was then aligned above the intersection of the DFB emission and the analyte channel. The analytes of this experiment were 1 μm red fluorescent microspheres (FluoSphere, Invitrogen) that had an absorption maximum of 580 nm and an emission maximum of 605 nm. A 3 μL droplet of the $4\ x\ 10^7$ beads/mL suspended in DI water was placed over the inlet of the analyte channel and vacuum applied at the outlet was used to pull the analyte solution through the channel. A 594 nm long pass fluorescence filter was placed in the path of the camera to block scatter from the DFB laser emission and from the 532 nm pump laser. When the collection region of the camera is reduced to a 40 x 40-pixel window, the frame rate can be increased to 2000 frames per second. This is essential to achieving a time resolution capable of capturing a single fluorescent bead per frame. A total time trace of 3 minutes was collected. In post processing, the intensity in the region of interest was integrated for each frame. Plotting this results in the time domain fluorescence trace shown in Figure 3.12.
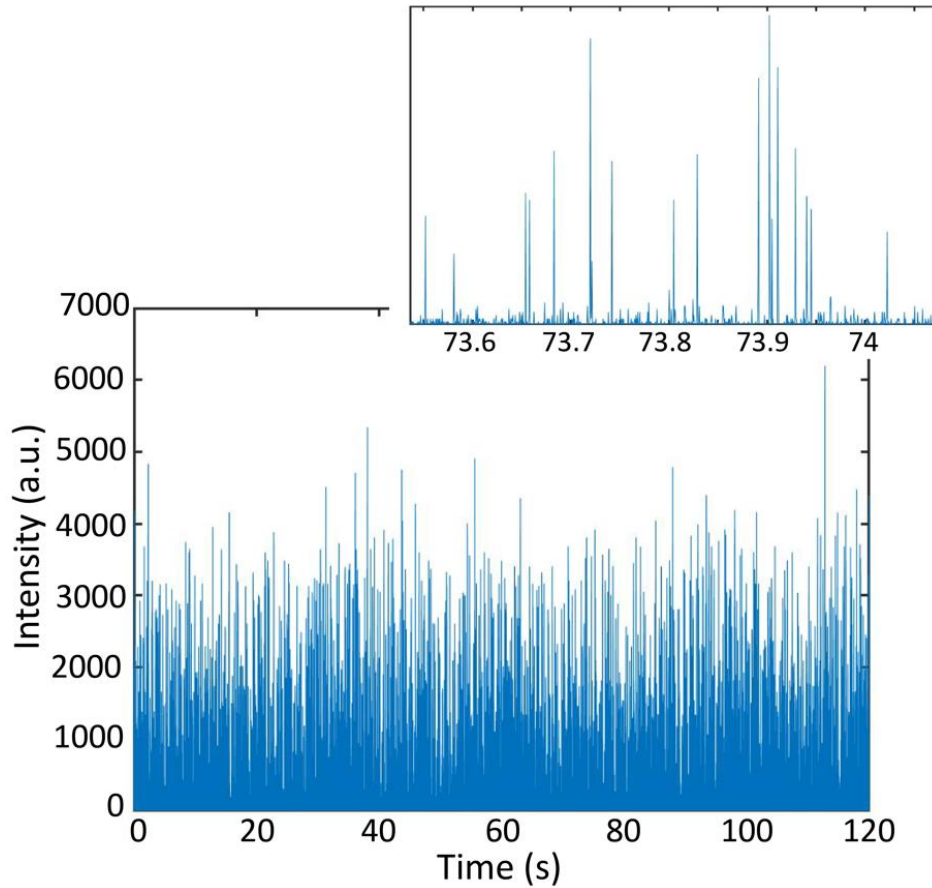
Figure 3.12. Fluorescence time domain trace resulting from camera collection of fluorescence detection of 1 μm red fluorescent microspheres. The zoomed image demonstrates individual peaks, representing detections of single microspheres.

Analysis of the fluorescence time domain trace was carried out using a parallel cluster wavelet analysis (PCWA) algorithm [93]. A Ricker wavelet, defined as the normalized second derivative of a Gaussian function, was used in a continuous wavelet transform (CWT) as it matches the time domain signal expected from single mode excitation. The CWT was calculated according to Equation 3.9 where the fluorescence time domain trace, $f(t)$, is convolved with the Ricker wavelet, $\psi(t)$, across a Δt range. The PCWA efficiently identifies fluorescence events amidst noise while extracting information about each event's time domain FWHM and peak height for signal analysis.

$$C(t, \Delta t) = \langle f, \psi_{t, \Delta t} \rangle = \int_{-\infty}^{\infty} f(t') \frac{1}{\sqrt{\Delta t}} \psi^* \left(\frac{t - t'}{\Delta t} \right) dt' \qquad (3.9)$$

The concentration of the fluorescence beads was deduced using Equation 3.10 where

N is the number of detected events, V_{exc} is the excitation volume, T is the total length

of the time trace and Δt_{avg} is the average FWHM of detected events. In the 120 second

trace, 3036 events were detected, yielding a detection rate of 25.3 events/second. The

excitation volume was found to be $4.3665 \; x \; 10^{-10}$ mL (mode width x mode height x

channel width: 4.1 µm x 7.1 µm x 15 µm). The average FWHM of detected events was

0.567 ms.

$$c = \frac{N V_{exc}}{T \Delta t_{avg}} \qquad (3.10)$$

The concentration of red fluorescent microspheres was thus determined to be

$3.29 \; x \; 10^7$ beads/mL, or 54.62 fM. The calculated concentration of fluorescent

microspheres shows good agreement with the expected concentration based on the

provided documentation and calculated dilutions.
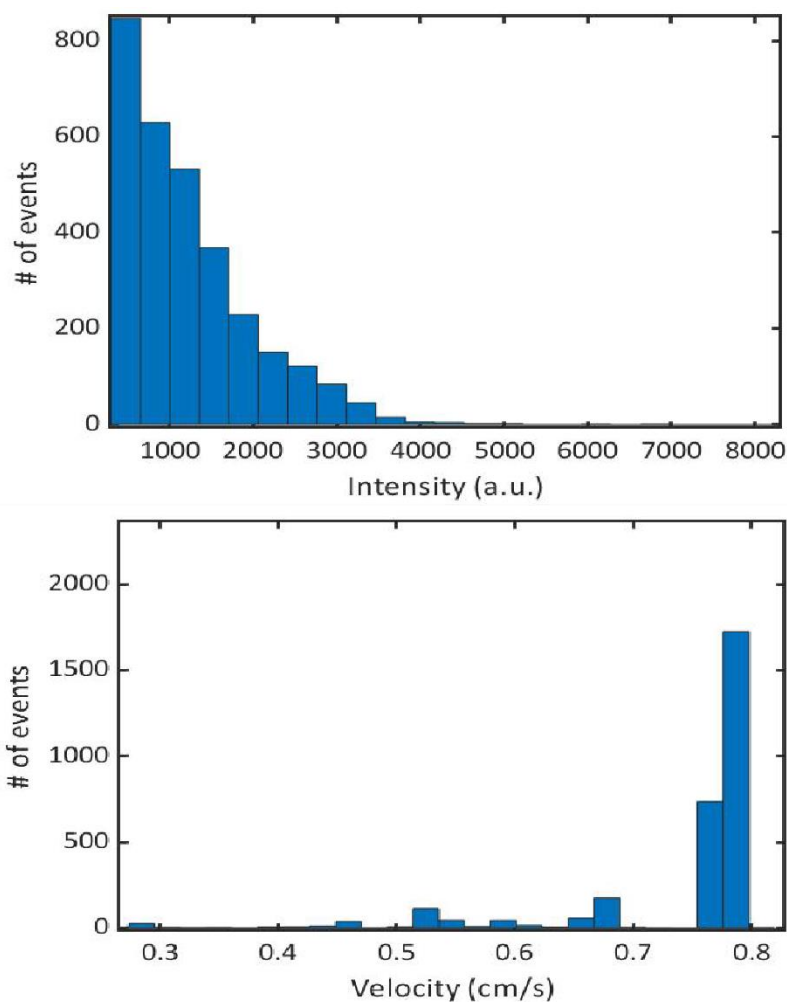
Figure 3.13. Intensity histogram of detected fluorescence events (top). The average intensity of detected events is 1222 with a standard deviation of 894. The velocity histogram (bottom) illustrates an average velocity of 0.74 cm/s with a standard deviation of 0.01 cm/s.

The intensity and velocity histograms of detected fluorescence events can be seen in Figure 3.13. The intensity histogram illustrates a tailed distribution, indicating that there are likely lower intensity signals that are missed. This could result from beads that flow through the excitation region very quickly and thus emit fluorescence for a much shorter period. Despite this, the agreement in concentrations indicates the effect of this is likely small. The velocity of each detected event was calculated by dividing

the excitation mode width by each event's Δt value. Since the maximum frame rate is 2000 frames per second, the time resolution is limited to 0.5 ms. The corresponding maximum detectable velocity was thus 0.82 cm/s corresponding to a bead that is in the excitation region for a single frame. As seen in Figure 3.12, a large portion of the detected events are at the maximum detectable velocity. Thus, it is likely that the true average velocity was higher. This was rectified in later experiments by reducing the vacuum applied at the outlet of the analyte channel via a regulator installed in the vacuum line. Another solution to this issue would be to use a camera with a higher frame rate capability to enable a higher time resolution.

3.3.4 Integration with Light Valve

Integration of pneumatic "lightvalves" has previously been demonstrated to deform PDMS and alter the optical guiding properties of liquid-core waveguides [35]. Here, we demonstrate the implementation of the "lightvalve" principle by integrating a 200 µm x 300 µm pneumatic switch segment above the DFB grating cavity (Figure 3.14a). When the pneumatic switch was actuated, positive pressure physically deformed the DFB grating and disturbed the optical feedback in the channel. This reversible actuation effectively placed the DFB laser in an "off" state. To quantify the effect of the pneumatic switch on output power, the analyte channel was filled with quantum dots suspended in water. The fluorescence emission from the quantum dots is easily imaged via camera (Figure 3.14b). The intensity of the fluorescence emission in a small region-of-interest was integrated and measured as a function of positive

pressure (Figure 3.14c). The output power from the DFB laser experienced a maximum

attenuation of -8.84 dB at a threshold actuation pressure of 50 psi.
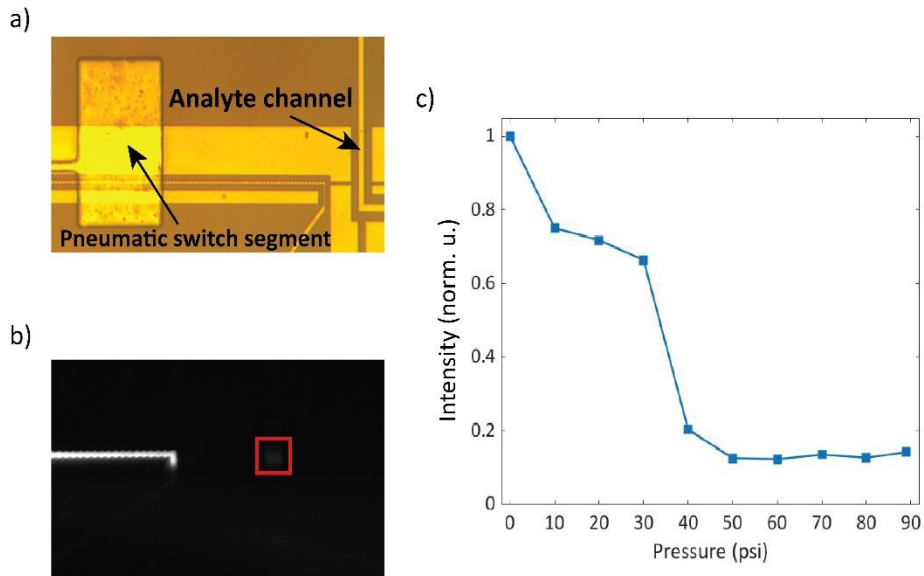
Figure 3.14. a) Camera image of pneumatic "lightvalve" switch located above the DFB grating. b) Top-down camera image of quantum-dot fluorescence emission with pneumatic switch applied (60 psi). Red box indicates the region-of-interest (ROI). c) Integrated intensity in the ROI as a function of positive pressure applied to the pneumatic "lightvalve."

A more direct measurement of the output laser power was also taken. Figure

3.15 demonstrates the power output of the solid-core waveguide coupled off-chip to an

optical power meter. The red lines indicate when a pressure of 60 psi was applied to the

pneumatic switch. The green lines show when the positive pressure was turned off,

demonstrating 5 continuous "on"/"off" cycles with the DFB power returning to the

same nominal output power. For each pneumatic cycle, the power reached an average

output of 6 µW in the "on" state and an average power of 1.3 µW in the "off" state (Figure 3.15). Thus, the reversible and repeatable attenuation when 60 psi was applied was -6.6 dB. The discrepancy in the attenuation of the output power collected from the solid-core waveguide versus the attenuation seen in the analyte channel is due to the location of the "lightvalve" switch. Since the switch was much closer to the analyte channel, a larger effect of the deformation was seen in the power output.
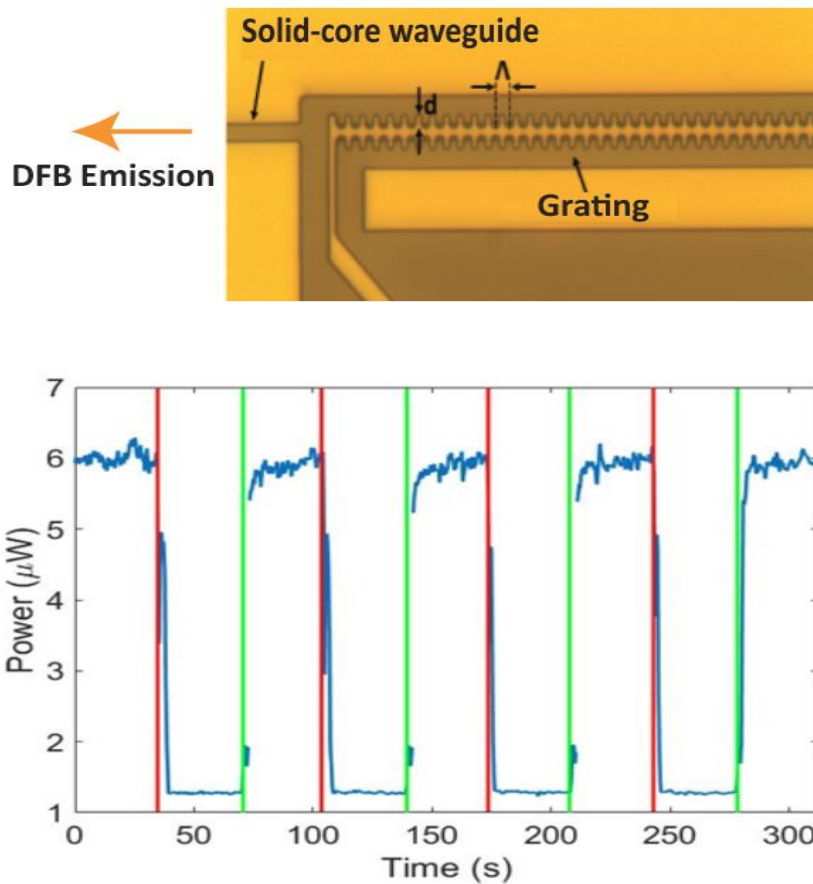
Figure 3.15. Output power from the Rhodamine 6G pump laser with 3 mW average pump power as a function of cycling the pneumatic "lightvalve" with 60 psi of pressure.

To demonstrate the ability to switch the DFB laser between "on" and "off" states, fluorescence detection was conducted while periodically actuating the pneumatic "lightvalve." Figure 3.16 illustrates the fluorescence trace resulting from pneumatically actuating the DFB laser while flowing $4x10^7$ beads/mL red fluorescent microspheres in the analyte channel. As demonstrated by the lack of detected events in the two 20 second periods where the DFB laser was pneumatically switched off, the pneumatic switch is effective at attenuating the DFB laser emission. By averaging the events seen detected in the "on" sections, the experimental concentration was determined to be $2.85x10^7$ beads/mL. Additionally, during the second "on" cycle, the pneumatic switch was briefly turned on at a reduced positive pressure of 30 psi. During this period, we can see that the overall background decreased, but events were still detected. This demonstrates the dynamic tunability of the light valve. The dynamic tunability of output power has potential applications in increasing dynamic concentration detection ranges in multiplexed biosensing such as presented in [94].
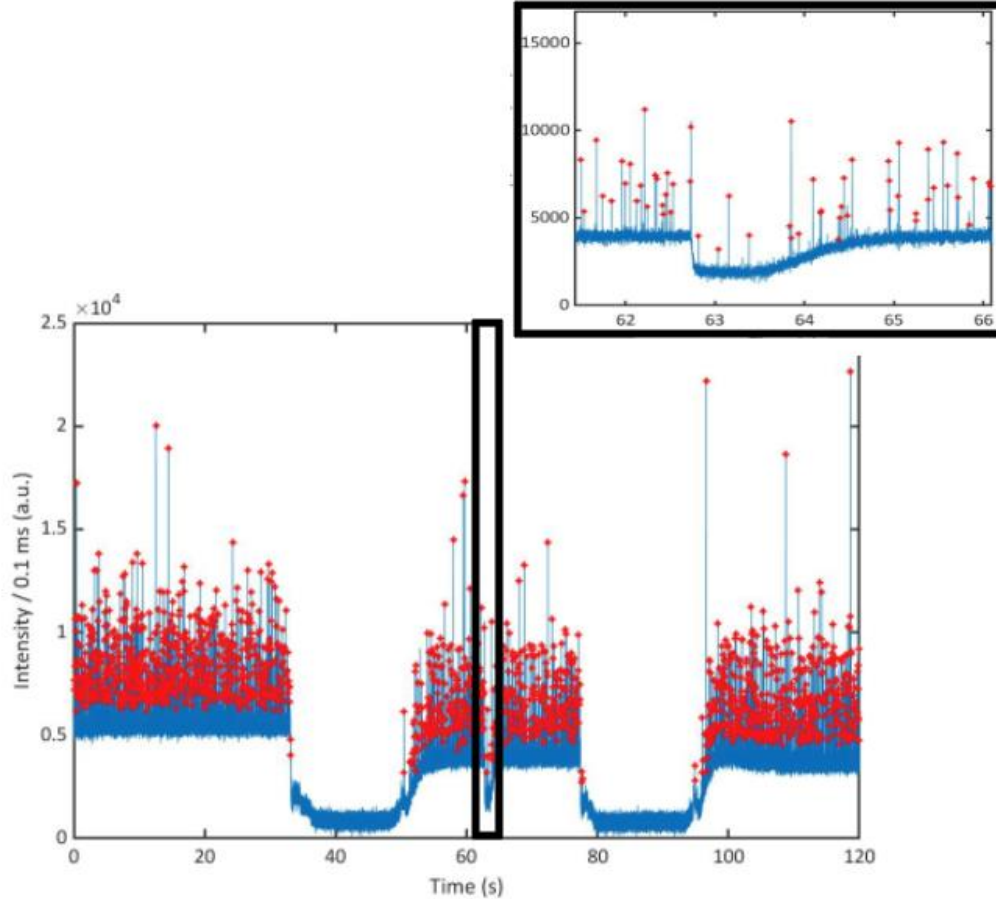
Figure 3.16. Demonstration of pneumatic switching during fluorescence detection of 1 μm red fluorescent microspheres. Top right trace is a zoomed portion of the trace where the pneumatic switch was turned "on" at 30 psi.

In conclusion, this chapter has presented a pneumatically tunable on-chip optofluidic Rhodamine 6G laser using a DFB cavity in an all-PDMS platform with a central lasing wavelength of 574.6 nm and a threshold pump fluence of 52.7 μJ/cm^2. For comparable Rhodamine 6G dye lasers reported in literature, pump thresholds have been reported in the tens [74] to thousands [82] of μJ/cm^2. Therefore, the threshold of the presented DFB laser is within a reasonable threshold fluence when compared with previous findings. This laser has been used to demonstrate optical detection of

49

fluorescent microspheres as a proxy for biomarker detection. Pneumatic switching of the DFB laser was also presented as a method of physically tuning output laser power on-chip with an attenuation of -8.84 dB. The fluidic nature of this laser allows for the gain medium to be swapped for different dye molecules or even have multiple dyes combined for multiple wavelength lasing. The next chapter will outline the addition of another DFB grating to increase the number of fluorescently labeled analytes that can be detected simultaneously. The fabrication of this DFB laser can be easily integrated into other PDMS-based devices. An example of this integration will be presented in Chapter 5 which will ultimately show the integration of the on-chip DFB laser into a LOC platform where the laser was integrated as a coherent light source with sample preparation and detection modules in a single PDMS device.

Chapter 4

Dual Distributed Feedback Dye Laser

As motivated in the introduction of this thesis, the simultaneous presence of multiple pathogens whose infections have similar symptoms has illustrated the need for highly sensitive biosensors that have multiplexing capabilities. This can largely reduce the time it takes for diagnoses as well as minimize misdiagnoses. Various methods have been explored to achieve this including velocity multiplexing [95] wavelength-dependent multimode interference waveguides (MMIs) which has been demonstrated to achieve 7x multiplexed biosensing [12]. Here, we present the addition of another DFB laser using a different gain medium to enable 2x spatially multiplexed detection of fluorescent microspheres as a proxy for detection of two separately labeled fluorescent biomarkers. In Section 4.1, the second laser using 4-(dicyanomethylene)-2-methyl-6-(4-dimethylaminostyryl)-4H-pyran is described and characterized with simultaneous operation alongside the previously presented Rhodamine 6G laser.

Section 4.2 will discuss the results from experiments demonstrating multiplexed detection of fluorescent microspheres.

4.1 DCM Laser
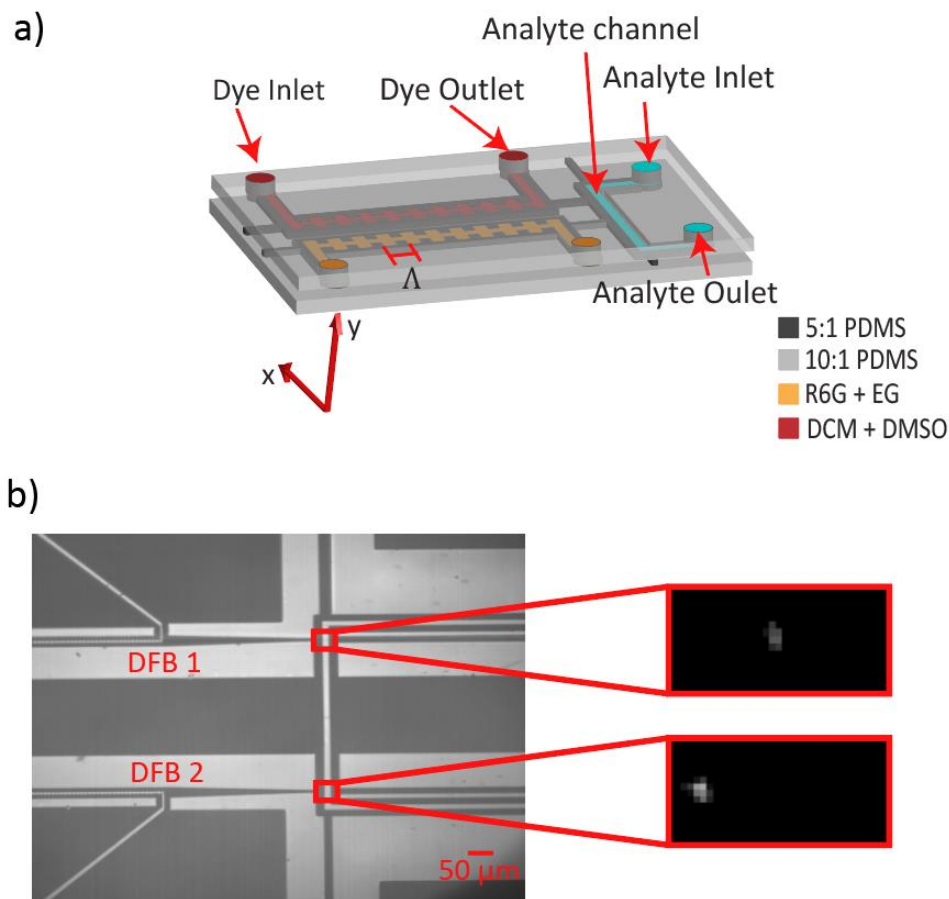
Figure 4.1. Device design. a) Chip design with two parallel DFB gratings of $\Lambda = 8\ \mu m$. One grating is used as a Rhodamine 6G laser and the other is used as a DCM laser. (Gratings are enlarged to enhance visibility). b) Top-down camera image shows the intersection of the two DFB lasers with an orthogonal analyte channel with zoomed images depicting examples of fluorescent detection from a 1 μm red fluorescent microsphere (top) and a 2 μm flash red fluorescent microsphere (bottom).

The majority of optofluidic dye laser have used Rhodamine 6G because of its high quantum yield and high solvent compatibility. Detecting multiple biomarkers

within a single analyte channel, however, necessitates a second excitation wavelength to excite another fluorophore. As described above, this can be achieved using Rhodamine 6G with a DFB laser using another DFB with a different grating period, but multiplexed fluorescence sensing benefits from a larger separation of excitation wavelengths.   4-(dicyanomethylene)-2-methyl-6-(4-dimethylaminostyryl)-4H-pyran (DCM) is another laser dye that has a high quantum yield, specifically when dissolved in dimethyl sulfoxide (DMSO) compared to other solvents [96]. Additionally, the fluorescence emission of DCM has large Stokes shift. This is beneficial in spectral multiplexing as this provides a larger separation between the absorption spectra of the two selected fluorescence markers.

Figure 4.1 illustrates a schematic of the dual DFB laser device, where another DFB grating was added in parallel to the existing grating. The high Bragg order of the $\Lambda = 8 \ \mu m$ gratings allow for it to be used interchangeably with other fluorescent dyes such as DCM with fluorescence aligning with the $m = 34$ Bragg order. A table of other dyes that have been used in dye lasers can be found in Appendix C. since other resonant wavelengths are still within the visible spectrum. Adding a second DFB laser with a different gain medium required the addition of a second pump laser to the setup as well. Since DCM was the desired gain dye, a 1-5 kHz, 473 nm pulsed pump laser with a 5 ns pulse width (RPMC Lasers, SB1 473-3-5) was added to the setup (Figure 4.2). A 45° knife edge prism was used to employ a symmetric bottom-up pumping scheme where the pump lasers are aligned together in millimeter proximities. For the 473 nm pulsed

diode laser, the beam shape was already elliptical, so a spherical lens was used to focus

the beam rather than the cylindrical lens used in the case of a Gaussian beam.
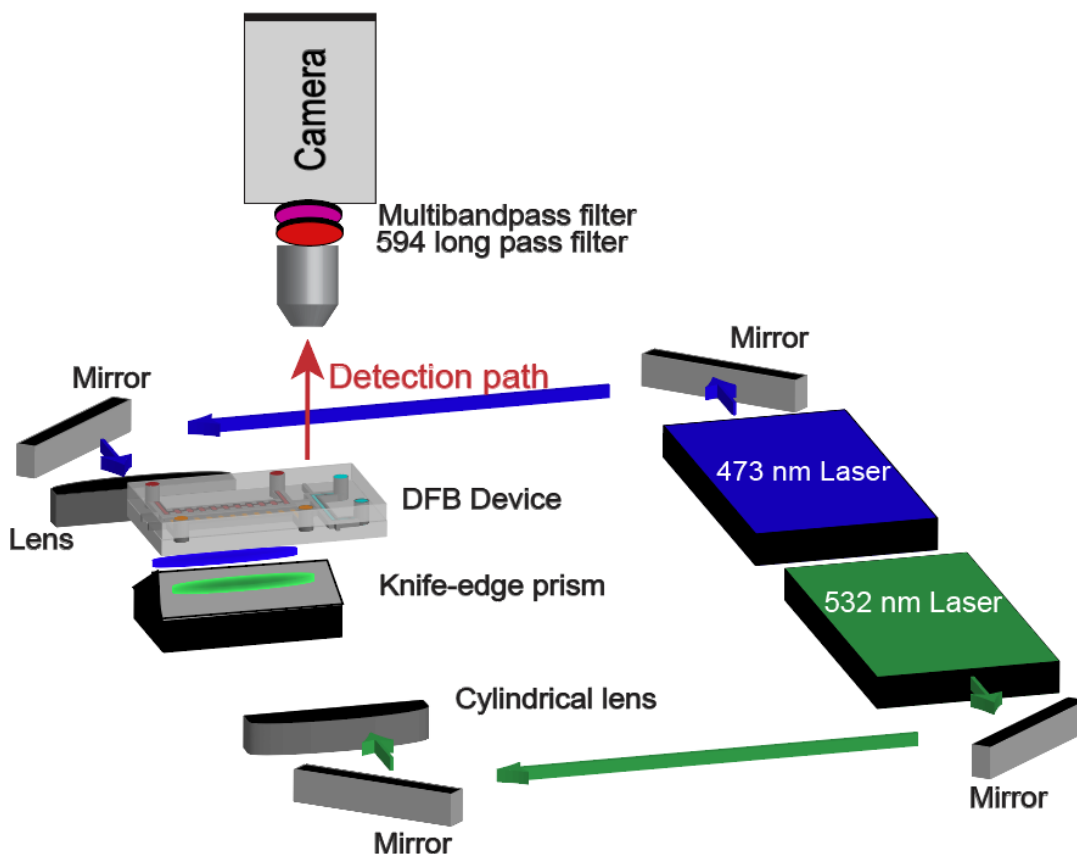
Figure 4.2. Dual DFB laser experimental setup. A symmetric scheme is used to simultaneously focus the 473 nm and 532 nm pump lasers below their respective laser channels using a 45° knife edge prism. Fluorescence events are captured using a camera aligned above the analyte channel with a 594 nm and a penta-bandpass filter in the camera path to remove any stray scatter from the pump and DFB lasers.
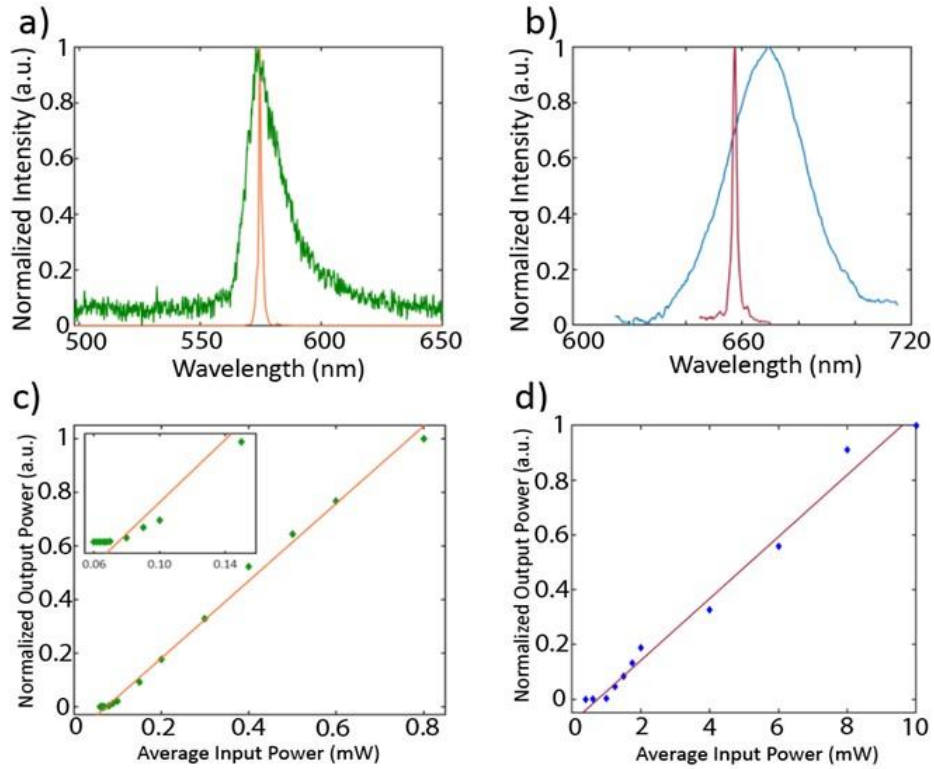
Figure 4.3. Laser characterization. a) A broadband ASE spectrum (green) is demonstrated when pumped below threshold while the narrowed lasing spectrum (orange) is observed when the Rhodamine 6G laser is illustrated when pumped above threshold. b) Similarly, a broadband DCM ASE spectrum (blue) is observed when pumped below threshold while the narrowed lasing spectrum (red) is overlayed when the DFB is pumped above threshold. c), d) Normalized average output power as a function of input pump power for the Rhodamine 6G and DCM lasers, respectively. The orange and red lines are linear fits conducted on the data points above threshold.

The power series for the Rhodamine 6G and DCM lasers are shown in figures 4.3c and 4.3d, respectively. As shown in Chapter 3, the threshold pump power is taken to be the intersection of the two apparent linear regimes in the power series. Using this method, the threshold input power for the Rhodamine 6G laser was measured to be 87.9 μW, corresponding to a threshold fluence of 52.78 μJ/cm^2. For the DCM laser, the threshold pump power was measured to be 0.77 mW, corresponding to a fluence of 307.6 μJ/cm^2. The higher threshold pump power of the DCM DFB laser can be

attributed to primarily to the fact that DCM as a laser dye has a lower quantum yield than Rhodamine 6G, meaning that it will be a less efficient lasing dye.

The lasing spectra from the dual DFB chip operating with both the Rhodamine 6G and DCM lasers simultaneously is shown in Figure 4.3a and Figure 4.3b. The Rhodamine 6G lasing spectrum is shown in orange with the ASE shown in green. The Rhodamine 6G laser demonstrates a central lasing peak of 574.6 nm with a FWHM of 1.24 nm. The DCM lasing spectrum is shown in red with the ASE shown in blue. The central lasing peak of the DCM laser occurred at 656.5 nm with a FWHM of 1.73 nm. The laser modes were imaged simultaneously using a 10x objective, shown in Figure 4.4. The modes were then imaged individually using a 40x objective to achieve better resolution. The Rhodamine 6G laser mode had a FWHM profile of 2.4 µm x 4.5 µm and the DCM laser mode was measured to be 2 µm x 5.2 µm.
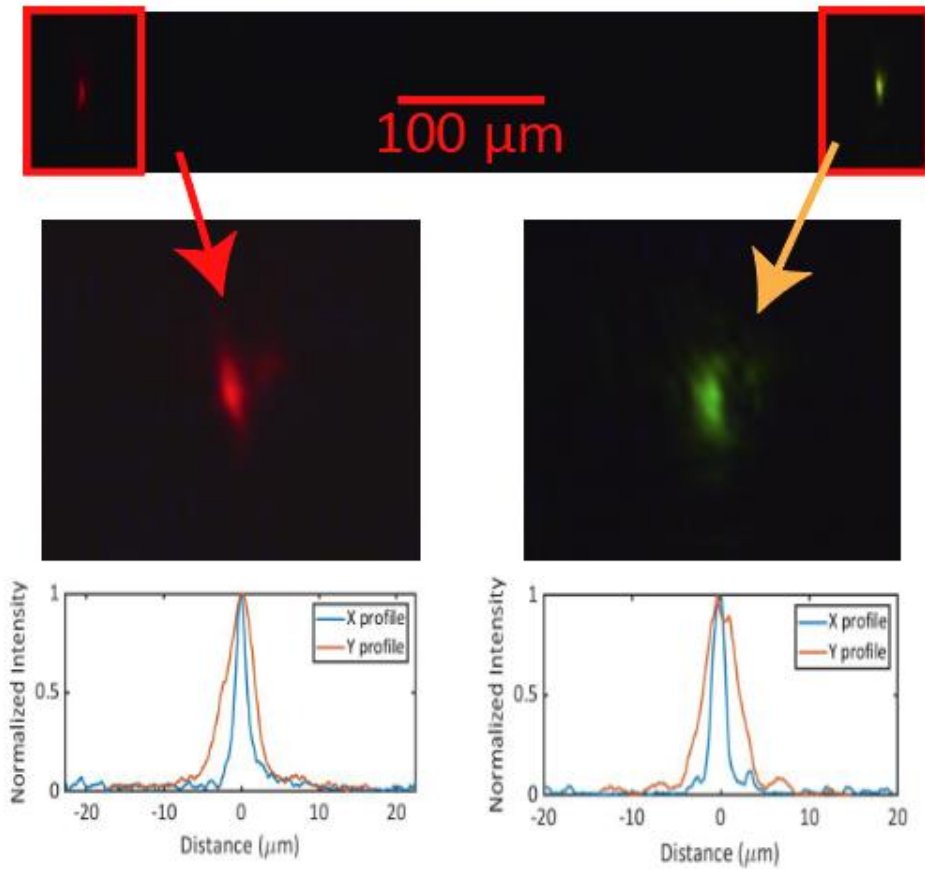
Figure 4.4. Mode images of the Rhodamine 6G and DCM lasers imaged using a 10x objective (top). The mode images were then imaged individually using a 40x objective (bottom) and integrated horizontally and vertically to extract X and Y mode profiles.

4.2 Spatially Multiplexed Detection of Fluorescence Beads

As described in Section 2.2, there are numerous ways of achieving multiplexed sensing. Since both excitation wavelengths are provided via a single mode excitation waveguide into the same analyte channel, multiplexing can be achieved via splitting the fluorescence wavelengths using a dichroic mirror or by spatially multiplexed detection. Keeping in line with the original camera detection scheme of the device

57

presented above, spatial multiplexing enabled by high frame rate capturing of both regions of interest was used.

After carefully aligning both pump beams below their respective DFB grating cavities, the DFB gratings were then filled with the gain media mentioned above. The solution used to fill the analyte channel was comprised of $2 \; x \; 10^6$ beads/mL 2 µm flash red microspheres (Bang Laboratories) and $4 \; x \; 10^7$ beads/mL 1 µm red microspheres (FluoSphere, Invitrogen). The 2 µm flash red beads were used as the specific biomarker proxy for the DCM laser with an absorption maximum of 660 nm and a peak emission at 690 nm. As demonstrated previously, the 1 µm red fluorescent microspheres were used as the specific analyte for the Rhodamine 6G laser with an excitation peak of 580 nm and an emission maximum of 605 nm. A 3 µL droplet of the sample solution was placed at the inlet of the analyte channel and pulled through using a vacuum pressure of -50 kPa. The camera was then aligned over the analyte channel and the acquisition frame was reduced to only collect the region including the two excitation regions. This smaller collection window enabled a 200 frames per second framerate acquisition corresponding to a time resolution of 5 ms. A 5-minute camera recording was then taken to capture fluorescence events. In post-processing of the video, two small regions-of-interest were defined around the excitation regions of each DFB laser (Figure 4.1b). In each of these ROIs, the intensity of each frame was integrated and plotted as a function of time.
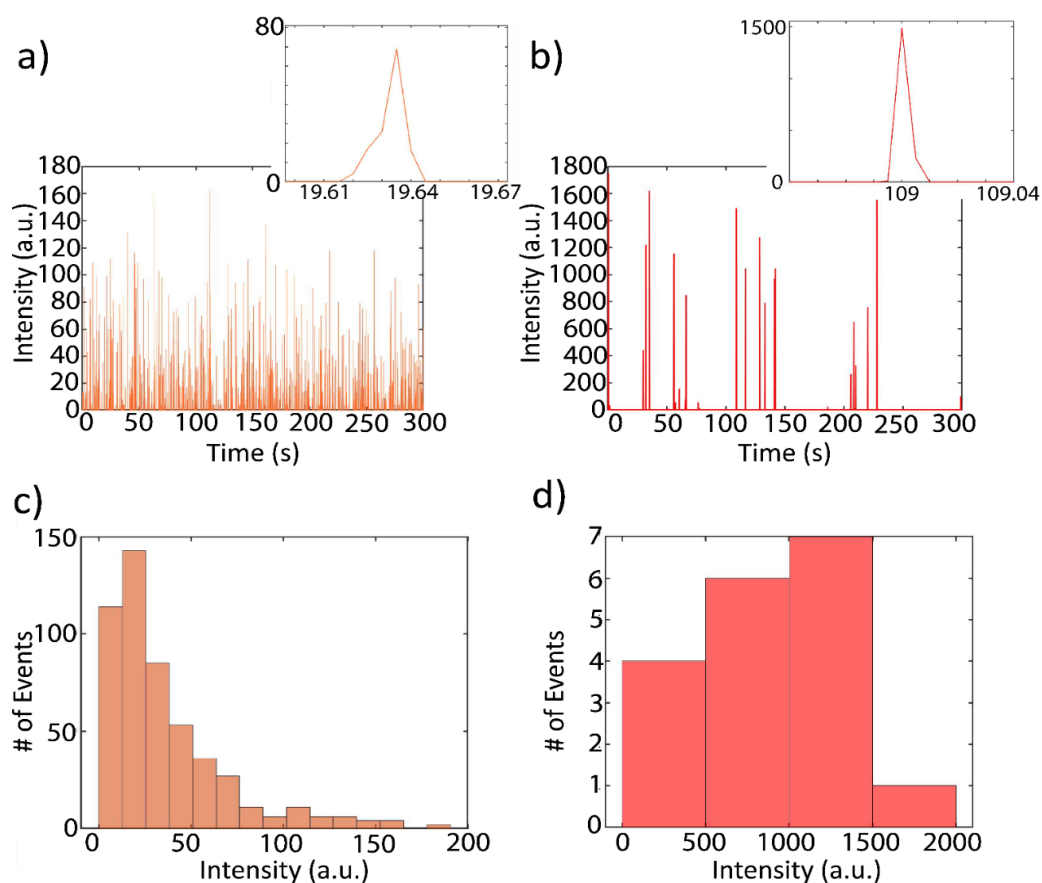
Figure 4.5. Simultaneous detection of two types of fluorescent microspheres. a) Fluorescence time domain trace from the Rhodamine 6G laser ROI illustrated peaks from detection of 1 μm red fluorescence beads. The zoomed image illustrates an individual event. b) Fluorescence time domain trace from the DCM laser excitation ROI illustrating peaks from detection of 2 μm flash red beads. c), d) Intensity histograms from the detected red and flash red fluorescent beads, respectively.

The resulting fluorescence time domain trace is shown in Figure 4.5. Following the same concentration calculations outlined in Section 3.3, the concentration of red beads was determined to be $3.97 \ x \ 10^7$ beads/mL and the concentration of flash red beads was $1.47 \ x \ 10^6$ beads/mL. The intensity histogram for the red fluorescent beads resembles a Gaussian distribution without the lower tail. Since lower intensity signals result from faster flowing particles that spend less time in the excitation region, these

are likely the missed events. The agreement between detected and expected concentrations suggests that the effects of this are small. The DCM intensity distribution roughly resembles a skewed Gaussian distribution, but the lack of events prevents the distribution from being well defined.
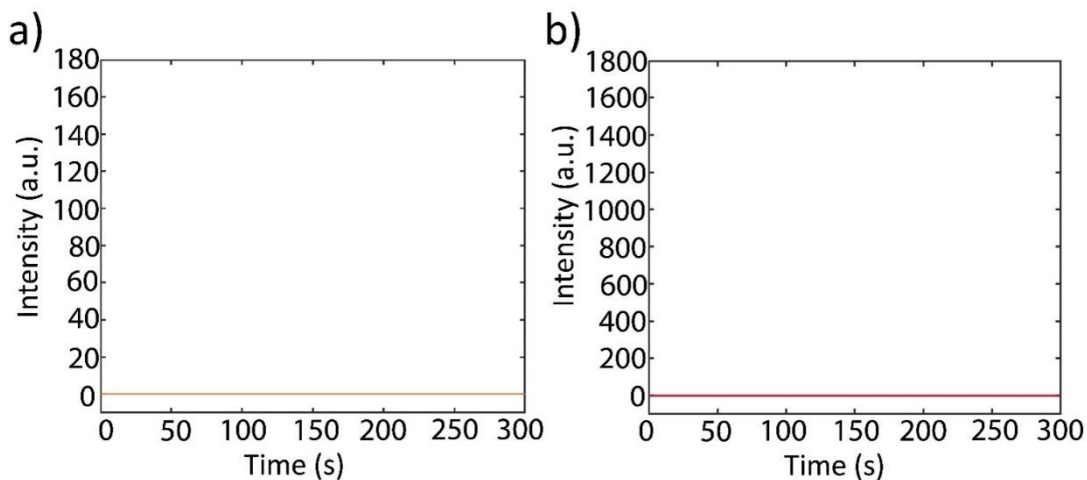
Figure 4.6. Negative controls. a) Fluorescence time domain trace from the Rhodamine 6G laser excitation ROI when only flash red beads were flown. b) Fluorescence time domain trace from the DCM laser excitation ROI when only red fluorescent beads were flown.

Negative controls were run and the resulting fluorescent time domain traces are displayed in Figure 4.6. To test for false positive detections, two negative control experiments were run. In the first, the analyte channel was filled only with 2 μm flash red fluorescent microspheres and only the Rhodamine 6G DFB laser was turned on. The resulting fluorescence time domain trace illustrates no false positive signals. The second negative control experiment consisted of flowing only 1 μm red fluorescent beads and operating only the DCM laser. Similarly, the resulting trace indicates no false positive detections. From the absence of false positive detections in these experiments,

we concluded that the 2x multiplexed detection of fluorescent microspheres was specific.

Thus, 2x spatially multiplexed fluorescence detection was demonstrated using an optofluidic device containing two simultaneously operating DFB lasers using Rhodamine 6G and DCM as gain media, respectively. This device design is scalable through the addition of more DFB gratings in parallel. These gratings can use the same dye as the gain media but vary in grating period to shift the DFB's resonant wavelength and emit different wavelengths. Additionally, different dyes can be used to employ vastly different excitation wavelengths. The high Bragg order allows for the cavities to be used in a multipurposed capacity with various dyes being used at nearby resonant wavelengths. This multiplexing method can also be combined with other demonstrated approaches such as velocity multiplexing where a second analyte channel is added, and analytes are pulled through at a different velocity. Using this method, each DFB laser gains the ability to measure two different analytes, adding a two-fold effect on the multiplexing capability of the entire device.

Chapter 5

All-in-One Optofluidic Lab-on-

Chip Biosensor

As described in Section 2.2, lab-on-chip biosensors are of high interest due to their ability to conduct sample preparation and biosensing while minimizing required laboratory equipment necessary, with vast applications in pathogen detection [51], food contamination screening [97], and single cell analysis [98]. These two primary functionalities have been carried out in hybrid systems combining PDMS-based pneumatic valve structures for sample preparation and solid-state electrical or optical detection devices [31], but the integration of two separate devices is often cumbersome and increases the amount of sample volume required. Therefore, development of a LOC contained in a single platform maintains the reduction of risk of contamination and laboratory equipment while simplifying fabrication and ease of device handling. The previous two chapters described a PDMS-based optofluidic DFB laser demonstrated to be applicable as an excitation source in biosensing applications. This on-chip light

source aids in simplifying the alignment required to supply excitation light in a confined volume to an analyte channel for fluorescence biosensing. This chapter presents the integration of the DFB laser with a PDMS-based sample preparation device to develop an all-in-one LOC optofluidic biosensor. This device was used to conduct generic fluorescence detection of stained double stranded DNA as well as specific detection of Zika nucleic acids, thus progressing towards a portable point-of-care device to aid in rapid disease diagnoses.

5.1 Chip Architecture
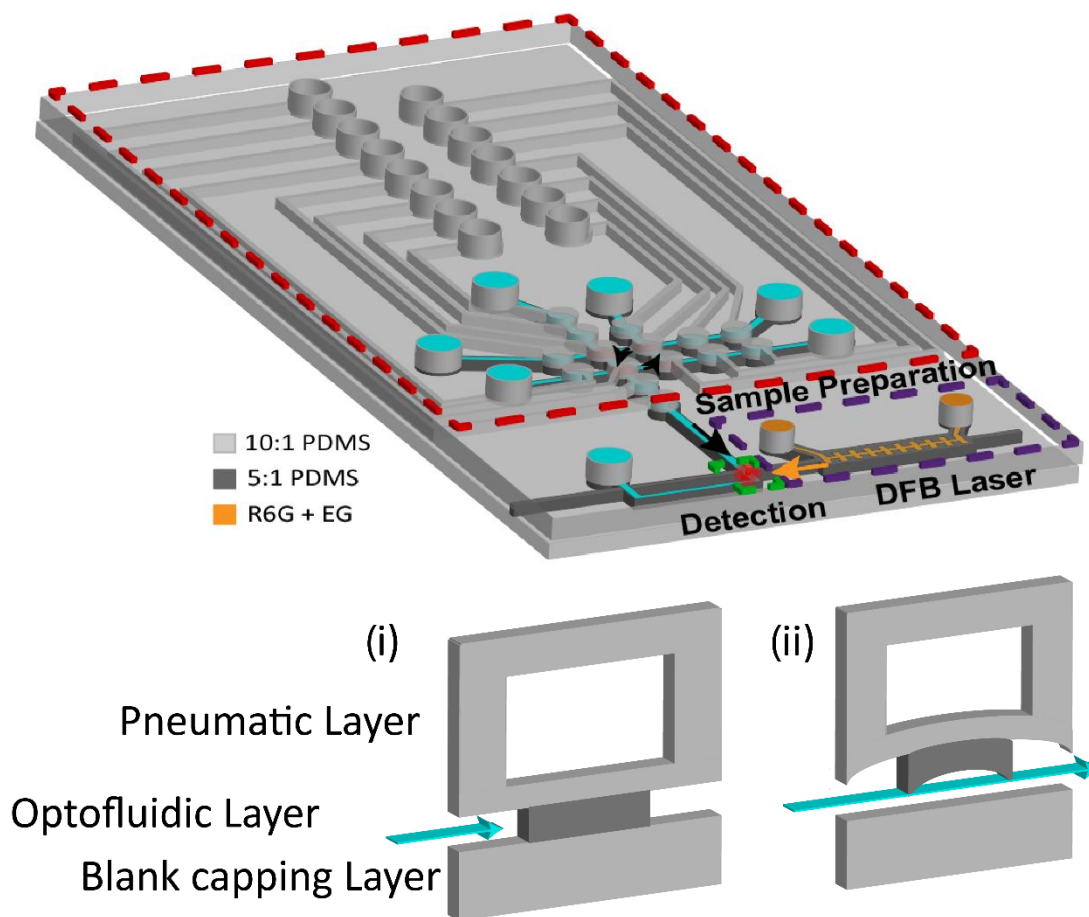
Figure 5.1. Top: Device schematic of all-in-one PDMS optofluidic LOC consisting of three distinct regions: sample preparation (red), on-chip DFB laser (purple), and optical detection region (green). Bottom: Cross-sectional diagrams of pneumatic lifting-gate valve structures with positive pressure used to close valves (i) and negative pressure used to lift valves and allow fluid flow between adjacent valves (ii).

The all-in-one biosensor presented in this thesis is comprised of three main modular components: sample preparation, light source, and optical detection. The sample preparation stage was an automaton comprised of a series of fifteen pneumatically actuatable PDMS valves. Pneumatic ports allow external negative and positive pressure to interface with a membrane on-chip that lifts and compresses to open and close the valve. A schematic of a PDMS valve is illustrated in Figure 5.1 and shows how negative and positive applied pressure is used to move fluid between valves and throughout the device. This sample preparation stage was developed based on the work presented in [34] and the device integration with optical detection was based on the work presented in [51]. The fifteen pneumatic lifting-gate valves were controlled using a custom-made control box that implemented LabView code to use a digital input/output board (National Instruments) to individually operate fifteen solenoid valves. The solenoid valves were connected to pneumatic lines that connected to their respective on-chip valves via 1 mm metal tubing that connected to the on-chip pneumatic inlets. Fabrication of the LOC device followed the same protocol as described in Section 3.2.1. The camera image depicted in Figure 5.2 is taken through a 532 nm long pass filter and shows an example of the LOC device with the DFB laser in operation. The scatter spot imaged within the white box illustrates the scatter of the DFB laser emission intersecting in the analyte channel.
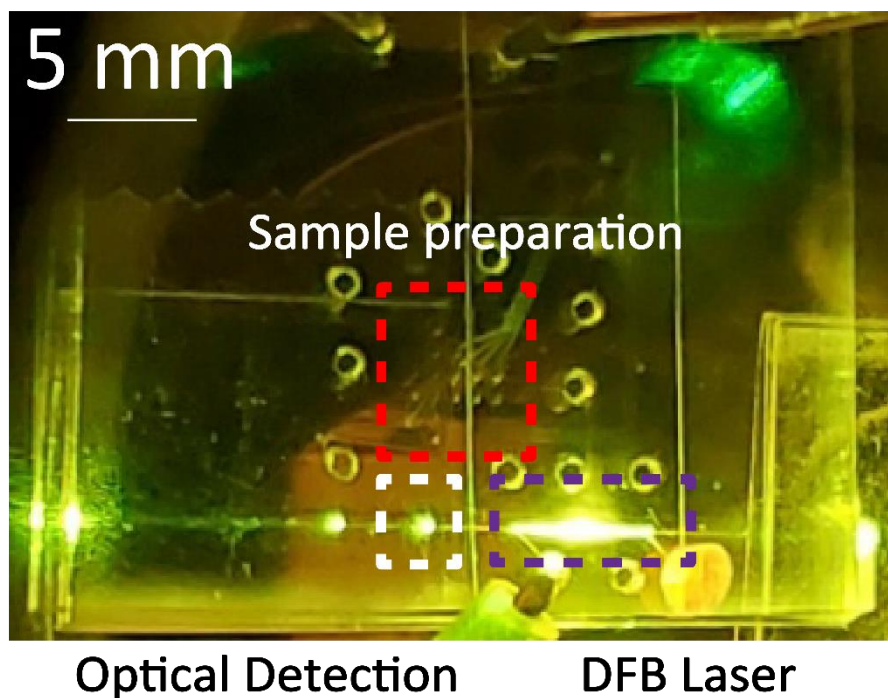
Figure 5.2. Top-down camera image of the all-in-one LOC indicating each of the on-chip modules: sample preparation (red), DFB laser (purple), and optical detection (white).

5.2 Nonspecific dsDNA Detection

Two types of nucleic acid detection were conducted during this study. The first was detection of 1 kbp double stranded DNA (dsDNA). In this experiment, 1kbp biotinylated dsDNA was captured onto 1 μm streptavidin coated magnetic beads (New England Biolabs) and stained with SYTO 64 intercalating dye (Figure 5.3a). 2 μL of $1x10^8$ beads/mL magnetic beads were placed above inlet 3, 50 μM SYTO 64 was placed above inlet 5, and 0.1 μM of biotinylated 1 kbp dsDNA was placed above inlet 6. 1xPBS was loaded into inlets 2 and 4 for wash and rinsing steps. The 1kbp dsDNA

and the SYTO 64 dye were pushed into the central four mixing valves (13, 10, 7, 2) and incubated together for 10 minutes. Following the staining of the dsDNA, the magnetic beads were added to the central mixing valves and incubated for a further 45 minutes. After the incubation period, the resulting bead construct contained stained dsDNA bound to the magnetic beads. A magnet was used to pull down the magnetic beads while 1xPBS from inlets 2 and 4 were used to wash unbound reagents to inlet 1, which was used as a waste inlet. At this stage, the pump laser was aligned to the DFB grating filled with 5mM Rhodamine 6G dissolved in the diluted ethylene glycol solution presented in Chapter 3. The camera was then aligned to the optical detection region of the chip to collect fluorescent signals and a 3-minute recording was taken at 0.5 ms exposure time. Finally, the sample was pushed through to the detection region through sequential actuation of valves 13-10-9-8.
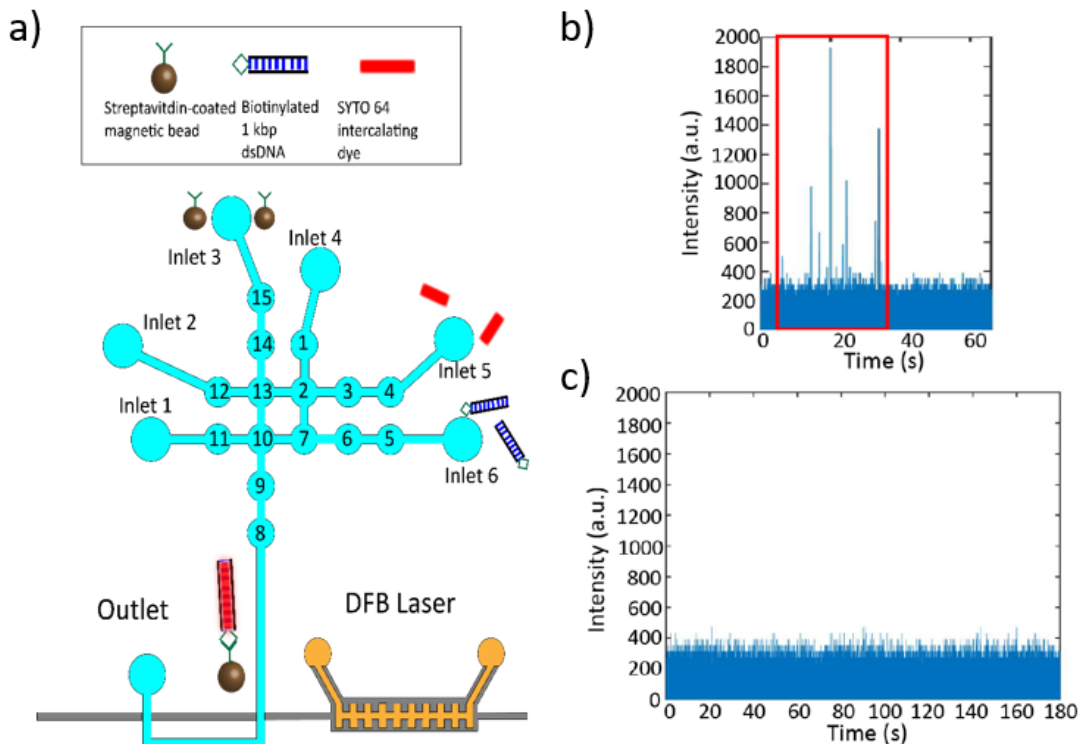
Figure 5.3. Non-specific biomarker detection. a) dsDNA assay outline. 1 µm streptavidin-coated magnetic beads were loaded into inlet 3 while SYTO 64 and biotinylated 1 kbp dsDNA were loaded into inlets 5 and 6. Inlets 1, 2, and 4 were loaded with 1xPBS buffer to aid in flushing the chip. Samples were combined in the central mixing valves (13, 2, 7, 10) where they were mixed and incubated for the proper construct to be formed. After the fluorescently stained targets were captured onto the beads, a magnet was used to pull the beads down and 1xPBS was washed through the valves to remove any unbound targets. The magnet was then removed and the sample solution was then pushed on to optical detection. b) Fluorescence time domain trace illustrating peaks observed from fluorescently labeled bead constructs. c) Fluorescence time domain trace resulting from negative control experiment conducted without dsDNA targets illustrating no false positive detections.

The resulting fluorescence time domain trace from integrating the intensity in the region-of-interest frame-by-frame is shown in Figure 5.3b. We observed an initial pulse of detections of the fluorescently stain dsDNA constructs, followed by no events detected for the rest of the trace. This was an expected observation as only one flush cycle was conducted. Due to the low number of detections, we noted that for future studies involving target-specific sensing that additional flush cycles should be used to resuspend more beads and maximize the detected events. As PDMS is a porous material, it is likely that magnetic beads became stuck in the valves as a result of the compression. A negative control was run in the absence of the 1 kbp dsDNA and resulted in no false positive events as seen in Figure 5.3c.

5.3 Target-specific Detection of Zika ssDNA

Zika nucleic acids were used as the biomarker for the target-specific study. Detection of the nucleic acids structurally used a magnetic bead-based sandwich assay to enable target-specific fluorescence detection (Figure 5.4). The base of the assay was

a 1 μm magnetic bead that was coated with streptavidin. A biotinylated 50-base pair long ssDNA oligomer (KU321639.1, nt. 130-179) served as the capture probe. The magnetic bead-to-capture probe construct was the only portion of the assay that was hybridized off chip. The target of the assay was a 100-base pair long ssDNA oligomer (KU321639.1, nt. 121-220) corresponding to the capsid region of the Zika genome. Lastly, a 25-base pair long oligonucleotide (KU321539.1, nt. 187-211) that had an AlexaFluor 594 fluorophore attached provided a target-specific reporter probe. The capture probe was designed as the complementary sequence to the 50 base pairs towards the bottom end of the target sequence while the fluorescent reporter was complementary to the 25 base pairs on the other end of the target.
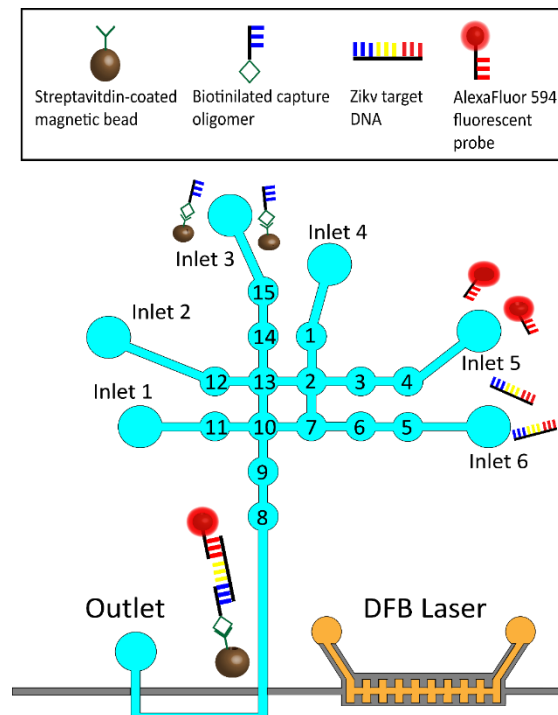
Figure 5.4. Specific Zika assay detection. 1 μm streptavidin-coated magnetic beads with biotinylated capture probes, AlexaFluor 594 fluorescent probes, and Zika ssDNA targets were loaded into inlets 3, 5, and 6, respectively. Assay reagents were brought into the central mixing valves (13, 2, 7, 10), mixed together, and heated to encourage hybridization. The completed magnetic bead constructs were pulled down using a magnet and 1xTE buffer was used to wash any unconjugated reagents away. After rinsing, the magnet was removed and the sample solution was pushed to the optical detection region.

The Zika nucleic acid assay is illustrated in Figure 5.4 and followed a similar protocol to that described in [51]. In preparation for the experiment, streptavidin-coated magnetic spheres were functionalized with the biotinylated capture oligomer. This was the only assay step that was completed off chip. At the start of the experiment 2 μL 1 x 10^9 beads/mL of 1 μm magnetic beads were placed over inlet 3, while 2 μL of 5 μM AlexaFluor 594 fluorescent probe was placed over inlet 5, and 2 μL of 5 μM Zika nucleic acid targets were placed over inlet 6. A molar excess of targets and fluorescent probes was used to increase binding probabilities and saturation of targets onto the magnetic beads. Two of the remaining three inlets (2 and 4) were loaded with 1xTE buffer to be used for cycling sample through and washing steps. Inlet 1 was used as a waste reservoir. The three assay constituents were pushed into the central mixing valves and cycled to mix the sample together. The entire device was then placed onto a thermoelectric heater that heated the chip to 40 °C for 5 minutes. This step encouraged hybridization of ssDNA targets to pull downs and fluorescent probes. The chip was then left to incubate for a further 25 minutes before being returned to its original mount where the 532 nm pump laser was aligned to the on-chip DFB as described in Section 3.2.2. A magnet was then placed underneath the chip to pull down the completed

magnetic beads and 1xTE buffer was used to wash excess targets and fluorescent

probes using actuation of valves 12-13-10-11 and 1-2-7-10-11. After properly rinsed,

the magnet was removed, and the buffer solution was cycled through to resuspend the

magnetic beads. Lastly, the completed assay was pushed sequentially through to the

optical detection region over the course of five cycles using 1xTE buffer. The resulting

fluorescence time domain trace is illustrated in Figure 5.5.
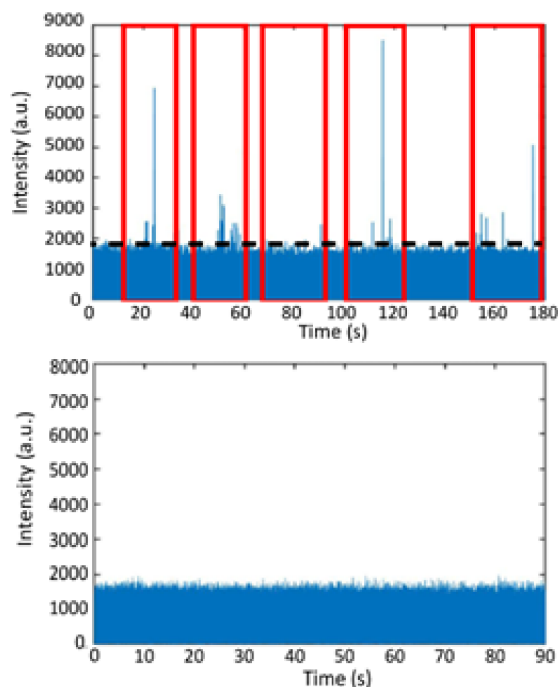
Figure 5.5. Top: Fluorescence time domain trace resulting from target-specific detection of fluorescently labeled Zika nucleic acid bead constructs. Bottom: Negative control trace conducted without Zika nucleic acid targets illustrating no false positive detections.

The average velocity of the detected particles was 0.34 cm/s, which is notably

lower than that of constant flow experiments demonstrated in Chapter 3 (Figure 5.6).

This can be explained by the fact that the velocity of the beads is dependent upon the

flow of fluid generated from the compression of pneumatic valves rather than the

70

vacuum pressure applied in the constant flow experiments. The intensity histogram of the events resembles the upper tail of a Gaussian distribution, indicating that there may be lower intensity events that were missed. This can result from very fast analytes that do not emit enough fluorescence to be detectable. A negative control was run where the assay was run identically, but in the absence of target Zika ssDNA. The resulting fluorescence time domain trace shown in Figure 5.5 illustrates no false positive events.
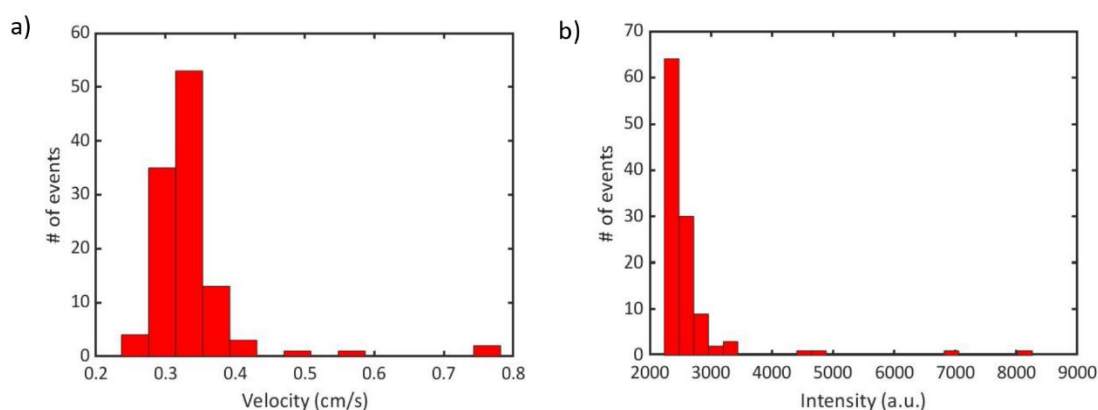
Figure 5.6. a) Velocity histogram from the detected events demonstrating an average speed of 0.34 cm/s and standard deviation of 0.07 cm/s. b) Intensity histogram from the detected Zika-bead constructs with a calculated average intensity of 2055 and standard deviation of 491.

Thus, we have demonstrated specific fluorescence detection of Zika nucleic acids through the integration of an on-chip distributed feedback laser with both optical detection and sample preparation functionalities on a PDMS lab-on-chip biosensor. This work presents continued significant progress towards a highly sensitive point-of-care LOC that can provide unique advantages in reducing the impact of future disease outbreaks. The use of LOC devices has been shown to reduce necessary sample volumes while implementing necessary sample handling on-chip, thus reducing risks of contamination and sample mishandling. Furthermore, by seamlessly integrating an

71

on-chip DFB laser, we avoid inconsistent and tedious optical alignment of external light sources. While the camera sensor further reduces necessarily meticulous optical alignment of single photon detections, additional steps in using APDs can be used to further increase the sensitivity of the device [51]. Long-lasting surface modification can also potentially aid in the efficiency of the sample preparation stage by reducing the number of beads becoming stuck within the porous PDMS [99]. Lastly, the PCWA algorithm for detection could be implemented in real-time to provide live results, thus further decreasing the sample-to-answer time [93].

Chapter 6

New Avenues for Optofluidic Biosensors

6.1 Optical Detection of Organoid-Derived Extracellular Vesicles
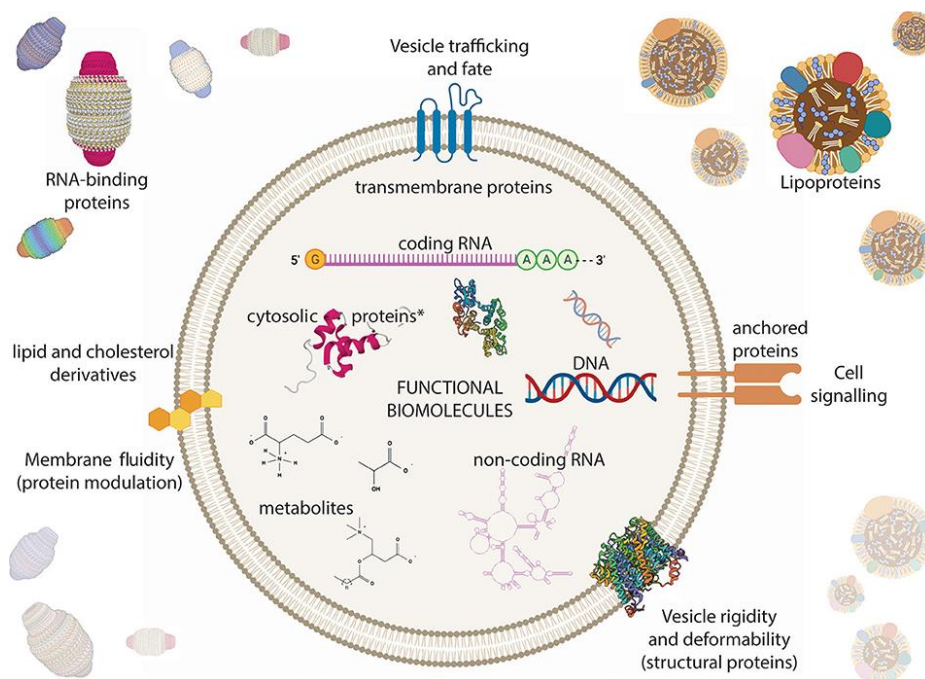
Figure 6.1. Schematic of an extracellular vesicle composed of a lipid bilayer with various surface proteins and cargo including nucleic acids, proteins, and metabolites [100].

Extracellular vesicles (EVs) are lipid-enclosed vesicles containing a wide array of cargo that are excreted into extracellular space [20], [100] (Figure 6.1). There are three subcategories of EVs that have been classified by size and biogenesis pathway: microvesicles, exosomes, and apoptotic bodies [18]. Microvesicles are 100 nm to 1 μm EVs that are typically formed via direct outward budding of the plasma membrane and contain mainly proteins embedded in the plasma membrane. Apoptotic bodies range from 50 nm to 5 μm in diameter, but the size distribution is typically on the larger end of the size range [101]. These vesicles generally contain intact organelles and proteins generally associated with cell lysate. Lastly, exosomes are EVs with diameters ranging from 30 nm to 150 nm formed by inward budding of endosomes originating from the cell plasma membrane. Exosomes and microvesicles have been demonstrated to be vital in cell-cell signaling between both local and distant cells [102]–[105]. One particular application of monitoring EV concentration and content is the role that EVs can play in cancer metastasis with cancer cells transporting their cargo to otherwise healthy cells [22], [106]–[108].

The increase of studies focusing on EVs within genomic science has combined with the advancement of laboratory-grown organoids and organ-on-chip technologies [109]–[111]. Organoids are three dimensional models of organs that are grown in vitro and have been used in recent years to study evolution and development of organs and diseases such as cancer progression. Here, we present proof-of-concept optical

detection of EVs derived from cerebral organoids grown by the UCSC Braingeneers within the established NIH Center for Excellence in Genomic Science (CEGS) using fluorescence staining using both a lipid-based stain and an intercalating nucleic acid stain. The future goal of this project is to integrate highly specific optical detection of EVs at a single EV sensitivity in a complete environment combined with modular automated cell cultures employing multiplexed organ-on-a-chip microfluidics [112].

6.1.1 Device Design and Setup

The goal of these studies is to optically detect EVs given their importance in cell signaling and health. Future studies will focus on detecting specific biomarkers within EVs. Since exosomes have been shown to be important in cell communication, they are of higher interest. As a result, any cell media received was filtered using a 200 nm filter. Given the small size of the targets, APD collection of fluorescent emission from stained EVs was used, in contrast to the camera collection presented in previous chapters.
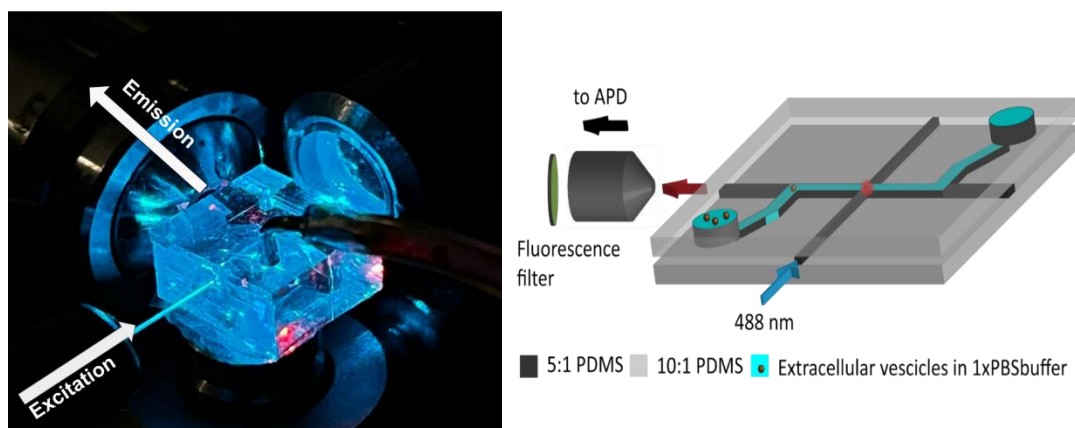
Figure 6.2. Left: Photograph of PDMS-based optofluidic chip and setup for optical detection of extracellular vesicles. Right: Schematic of optofluidic chip. External light was coupled to the chip via a solid-core waveguide that intersects with an orthogonal analyte channel. A second solid-core waveguide carries fluorescence emission from EVs and a 40x objective couples the emission through a fluorescence filter and into an APD.

The optofluidic PDMS device used in these experiments followed a simple single mode excitation scheme (Figure 6.2). A solid-core waveguide composed of 5:1 PDMS was used to couple external 488 nm laser light to an orthogonal liquid-core analyte channel. The mode image of the light coupled through this waveguide is displayed in Figure 6.3 with the intensity profiles in the horizontal and vertical dimensions. Sample fluid was pulled through the analyte channel using a regulator-controlled vacuum line inserted into the outlet, shown as the metal inlet in Figure XX. A wide solid-core waveguide collected fluorescence emission from detected EVs and a 40x objective was used to couple light to free space through a fluorescence filter. The fluorescence emission was finally coupled back into a multimode fiber where it was guided into an APD.
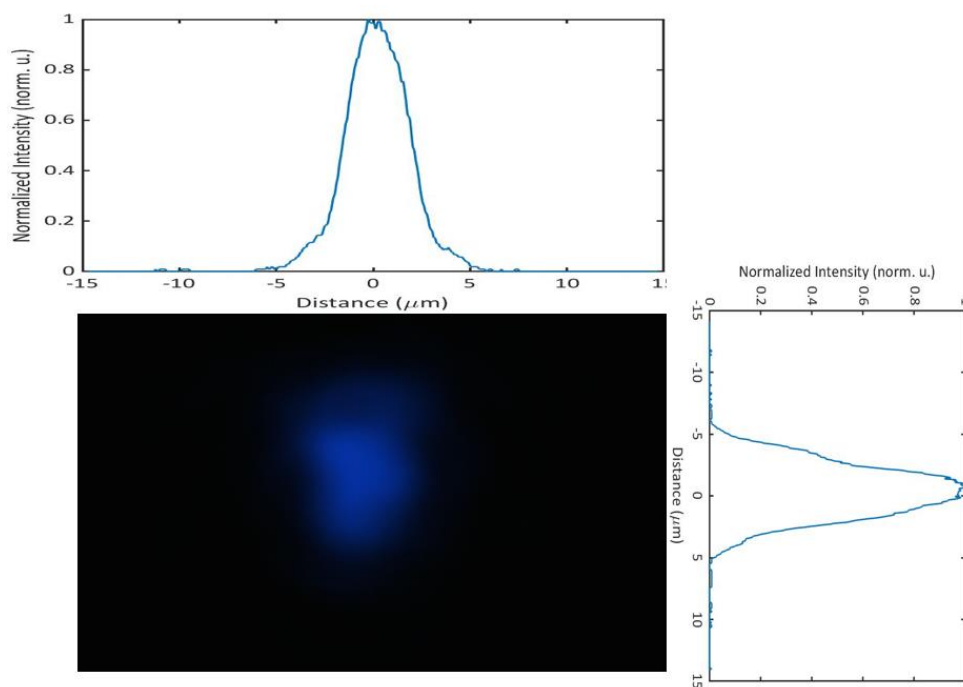
Figure 6.3. Mode image of the excitation light guided through the solid-core excitation waveguide. The FWHM dimensions of the excitation mode were measured to be 3.74 μm x 5.08 μm.

6.1.2 Results

The EV sample tested in these experiments was conditioned media from 56-day-old cerebral organoids. Prior to staining, all conditioned media was filtered using a 200 nm sterilized filter (MilliporeSigma). The first fluorescence stain used was vFRed, a proprietary lipophilic stain (Cellarcus Biosciences). vFRed has an absorption maximum at 465 nm and a large Stokes shift with an emission maximum at 590 nm. For the vFRed stained EVs, a 532 nm long pass filter was used to block out any light from the 488 nm excitation laser. As per the assay protocol, 5 μL of 10x diluted vFRed was combined with 5 μL of 200 nm filtered conditioned media and 40 μL of staining buffer provided by Cellarcus Biosciences. The combined solution was incubated on a

rotary mixer for 1 hour before being pulled through the analyte channel. The second

stain used was SYBR Gold (Invitrogen), an intercalating nucleic acid stain. SYBR Gold

has an absorption maximum at 495 nm and an emission maximum at 539 nm. Since

the 532 nm long pass filter would block out some of the fluorescence emission, a 440-

521-607-694-809 multi bandpass filter was used as the fluorescence filter in the APD

collection path. In experiments using SYBR Gold, 2 µL of 1x SYBR Gold was used to

stain 2 µL of 200 nm filtered cell media in 16 µL of 1xPBS buffer. The solution was

left to incubate for 20 minutes on a rotary mixer before being pulled through the analyte

channel as per the SYBR Gold staining protocol.
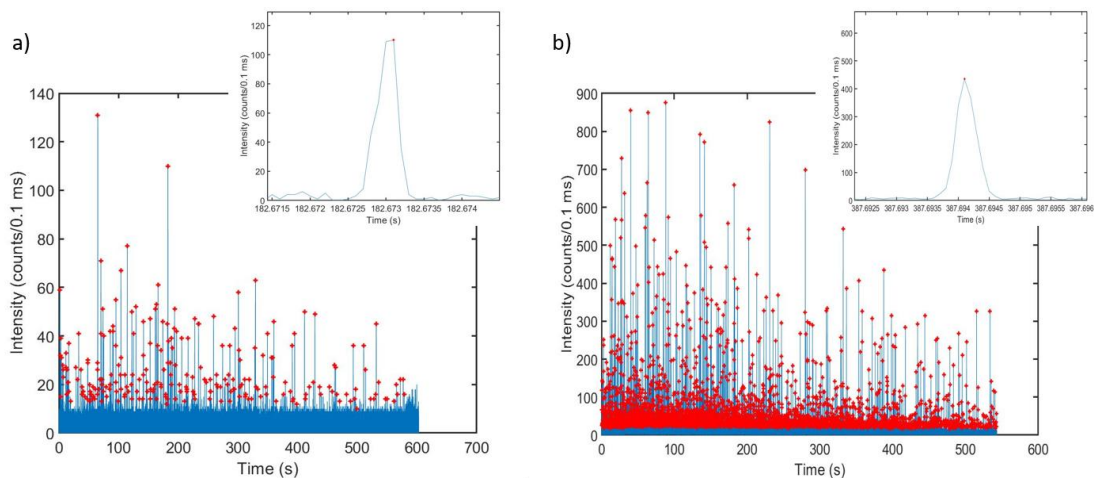
Figure 6.4. Fluorescence time domain traces from EVs stained with a) vFRed and b) SYBR Gold.

The results of fluorescence detection experiments using vFRed and SYBR Gold

independently are shown in Figure 6.4a and 6.4b, respectively. Similar to the previously

presented studies, event detections were identified using a PCWA algorithm using a

Ricker wavelet. Experimental concentrations were calculated using the same equation

as described in Section 3.3.3, but the excitation volume used was calibrated for this

78

device ($V_{exc} = 3.74 \; \mu m \; x \; 5.08 \; \mu m \; x \; 15 \; \mu m = 2.8x10^{-10} \; mL$). The concentration of the vFRed stained EVs was thus calculated to be $2.6 \; x \; 10^6$ EVs/mL while the concentration of SYBR Gold stained EVs was determined to be $9.33 \; x \; 10^7$ EVs/mL. The intensity histogram of the detected events from each experiment overlapped are displayed in Figure 6.5. From the concentration measurements, it is evident that there are significantly more events detected in the SYBR Gold stained EV experiment. Additionally, the average event intensity of the detected SYBR Gold EVs was calculated to be 76.2 counts/0.1ms compared to 26.4 counts/0.1ms for the vFRed stained EVs. Thus, SYBR Gold granted an ~3x improvement on event intensity with ~36x more detected EVs.
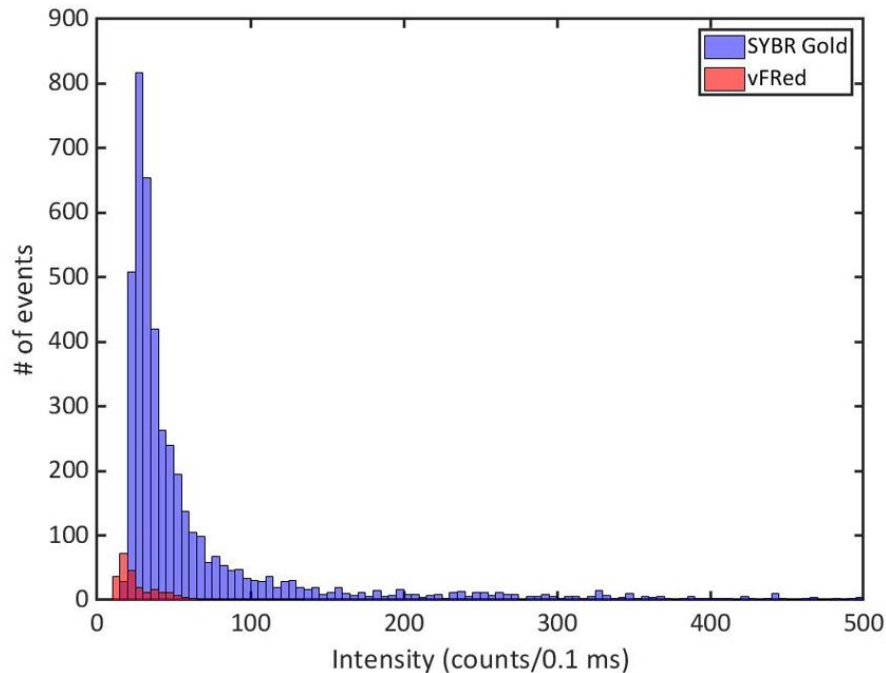
Figure 6.5. Overlayed intensity histogram from detected events from the SYBR Gold and vFRed staining of EVs. The SYBR Gold distribution had a mean intensity of 76.2 counts/0.1 ms compared to the 26.4 counts/0.1ms average observed from the vFRed staining.

Thus, we have demonstrated detection of single EVs at femtomolar concentrations. This work provides a proof-of-concept foundation for continued optical analysis of single EVs. Additionally, it is possible to continue to probe the cargo and surface biomarkers of EVs by using target-specific fluorescent probes to gain further insight into the various cell signaling markers that are being excreted by these cortical organoids. Lastly, the implementation of this detection on a PDMS platform presents ample opportunity for continued device integration with the existing organoid culturing platform to progress towards an on-demand diagnostic measurement of organoid health.

6.2 Educational Outreach Using Remotely Controlled LOC Platform
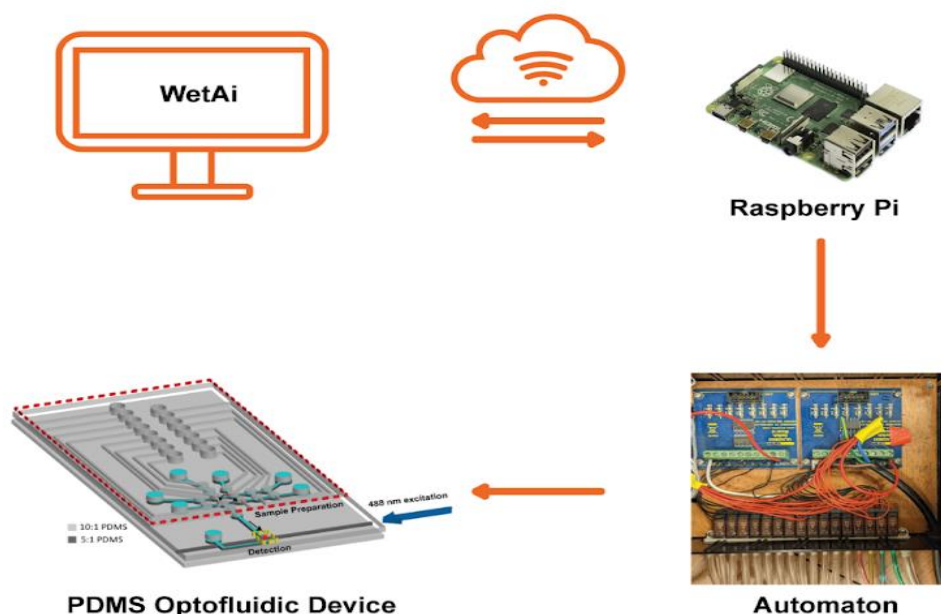
Figure 6.6. Integration of internet-of-things with programmable LOC allows for remote control of valve actuation on-chip through internet connectivity.

Modern STEM fields greatly benefit from a diverse workforce with diverse teams demonstrating increased impact of publications and complementary skills [113], [114]. Despite this, high level scientific training often misses the mark in including minority groups such as women and Latinx students. Increasing efforts are being made to explore ways in which modern tools such as the internet-of-things (IoT) can be used to expand educational outreach opportunities [115]. Lab-on-chip technology enables a vast array of benefits that expands beyond pathogen detection. By combining LOC technology with the internet-of-things (IoT), high level biomarker detection can be brought to vast distances and enable higher level of scientific accessibility and educational outreach (Figure 6.6). Here, we present an integration of LOC technology and project-based learning (PBL) implemented using IoT in order to conduct an

educational outreach project conducted with first to fourth year university students at the Universidad Católica Boliviana San Pablo in Bolivia. The motivation of this study was to provide context-aware PBL using LOC technology to students in Bolivia to demonstrate the ability to democratize science and bring exposure and access to underrepresented communities. This collaborative work with Mohammed Julker Neyen Sampad, Dr. Mohammed A. Mostajo-Radji, Dr. Sofie Salama, and Dr. David Haussler was conducted as a facet of the NIH CEGS Center and was reviewed and approved by the UCSC Institutional Review Board (HS-FY2023-42) and the Ethics Committee at the Universidad Católica Boliviana San Pablo (Protocol Approval 034).

Step 1: Lecture on Theory
Lecture on Lab-on-a-Chip systems and optofluidic with background and application towards staining *E. coli* for detection *(In Spanish)*

Step 2: Instruction
Lecture on how to program valve sequences to manipulate fluids to conduct assay. It was performed with food dye as demonstration of chip function *(In Spanish)*

Step 3: Programming
Give students a skeleton code for *E. coli* staining to be completed as homework.

Step 4: *E. coli* staining and detection
Give feedback to the students and run their code in LoC device to detect the stained *E.coli (In English translated to Spanish)*

Step 5: Data Analysis
Fluorescence detection data is analyzed in post and returned to students in the form of fluorescence time domain traces and videos of detection events

Figure 6.7. Context-aware remote PBL-training using LoC systems. A) Training workflow. In the first lecture the students are taught the theory of LoC systems and their applications to pathogen detection. In the second lecture, the students are taught how to program LoC systems. Both lectures are taught in the students' native language. The students are then assigned a project detecting bacteria in water samples. They then complete the assignment, upload their code and receive feedback. The LoC system is then run with their code and the data is produced, analyzed and returned to the students.

Water contamination was used as the framework for this study since Bolivia has a complicated history with regards to water quality and accessibility. Significant contamination of *Escherichia coli* (E. coli) in drinking water was reported in 2010 of up to 64% of tested water samples [116]. Given this history, fluorescence detection of E. coli was determined to be a fitting project for implementing remote PBL and exposing students to a high-level biosensing experiment. The training module was split into a lecture portion and an experimental session (Figure 6.7). Two lectures of one hour length each were given outside of official class times. The first lecture laid the foundation for LOC technology and its applications. Students were introduced to the specific chip that they would be using to test for E. coli as well as how the chip was fabricated. During the second lecture, students were shown how to use various coding elements to program sequential valve operation with examples of how certain sequences would move fluid throughout the device. The module culminated in a one-on-one session where students were able to remotely initiate the code they completed to operate an LOC located in Santa Cruz, California and stain and optically detect fluorescently labeled E. coli.
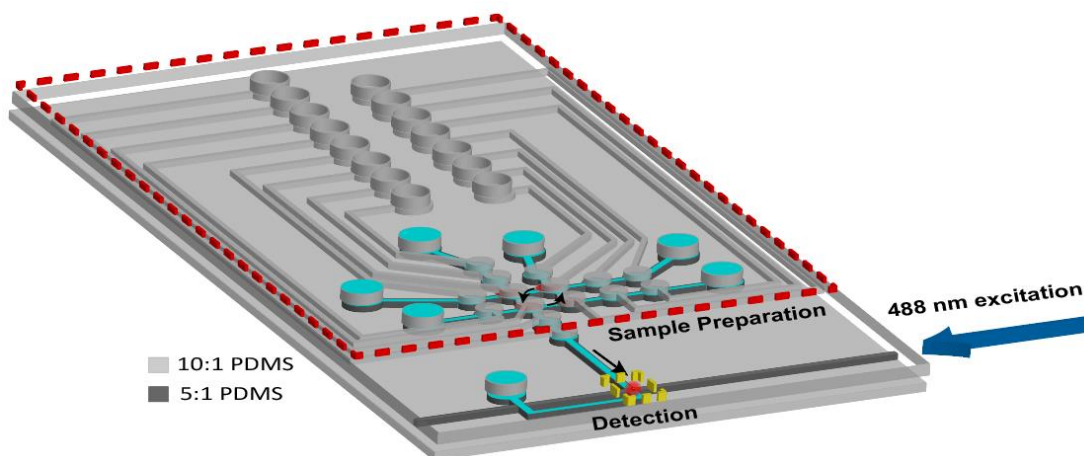
Figure 6.8. Lab-on-chip device integrating sample preparation with optical detection.

The LOC chip that was used in this study was a PDMS-based device that integrates sample preparation and optical detection stages (Figure 6.8) [51]. This device has been used to demonstrate fluorescence labeling and detection of Zika nucleic acids and proteins. Nanoliter scales of sample volume and assay reagents were controlled using a series of fifteen pneumatic valves. The valve structures measured 500 μm in diameter with a channel height being approximately 5-7 μm throughout the device. The air gap used to lift the valve was roughly 25 μm tall. Valve actuation was carried out using a custom-made control box connected to a vacuum source as well as compressed air. The control box used a National Instruments digital I/O board to control fifteen solenoid valves, one for each PDMS valve as presented in Chapter 5. Negative pressure was used to lift the PDMS valve which allowed fluid to move between adjacent valves. When positive pressure was applied, the valves would close, and fluid would be pushed in the direction of open adjacent valves.

In this implementation, remote control of the automaton was required for students in Bolivia to operate the LOC. As a result, the LabView control software was replaced by a Raspberry Pi controlling the I/O board and solenoid valves which acted as the local IoT device. The Raspberry Pi was connected and controlled by a web-based graphical user interface (GUI) via Message Queueing Telemetry Transport (MQTT) protocol. The GUI was hosted in Jupyter Notebook through wetAI, which is an online platform established by the UCSC Genomics Institute that enables remote access. A straightforward programming language implementing the same commands (e.g. "o" for open, "c" for close) as used in previous LOC experiments was integrated via a Python interpreter to code sequential valve operation. Using this platform, a remote user can log in to wetAI and execute their own script which transfers via MQTT to the local IoT device where the Python interpreter decodes the information and operates the solenoid valves.

```
main                    detect              flush
call rotateCW 5         o10                 o1
call wait 1             call wait 1         call wait 1
call detect 1           o9                  o2
call wait 1             call wait 1         call wait 1
call flush 15           o8                  o13
end                     call wait 1         call wait 1
                        c2                  o10
rotateCW                call wait 1         call wait 1
o??                     c13                 c9
call wait 1             call wait 1         call wait 1
c??                     c10                 o8
call wait 1             call wait 1         call wait 1
o??                     c9                  c1
call wait 1             call wait 1         call wait 1
c??                     c8                  c2
call wait 1             call wait 20        call wait 1
o??                     end                 c13
call wait 1                                 call wait 1
c??                                         c10
call wait 1             wait                call wait 1
o??                     w1000               c9
call wait 1             end                 call wait 1
c??                                         c8
call wait 1                                 call wait 20
end                                         end
```

valve orientation

Figure 6.9. Example of redacted skeleton code given to students as homework. Commands: "c" = close, "o" = open, "w" = wait.

During the second lecture, a live demonstration of mixing red and blue food dye together was used as a proxy for mixing assay reagents to illustrate how fluids were mixed. At the conclusion of the second lecture, students received a skeleton code of a program designed to stain E. coli with SYBR Gold. The students' homework was to

complete the redacted portions of the code that would be run in a one-on-one session where the students would be able to run their code remotely and conduct a successful staining and detection of E. coli (Figure 6.9). Accuracy in completing the skeleton code that was given as homework was evaluated in determining the success rate of groups. Based on this metric, 10 out of the 11 (90.9%) participating groups successfully completed the redacted code. The sole error was a minor fault that was rectified during the one-on-one session so that the group would still be able to run their experiment.
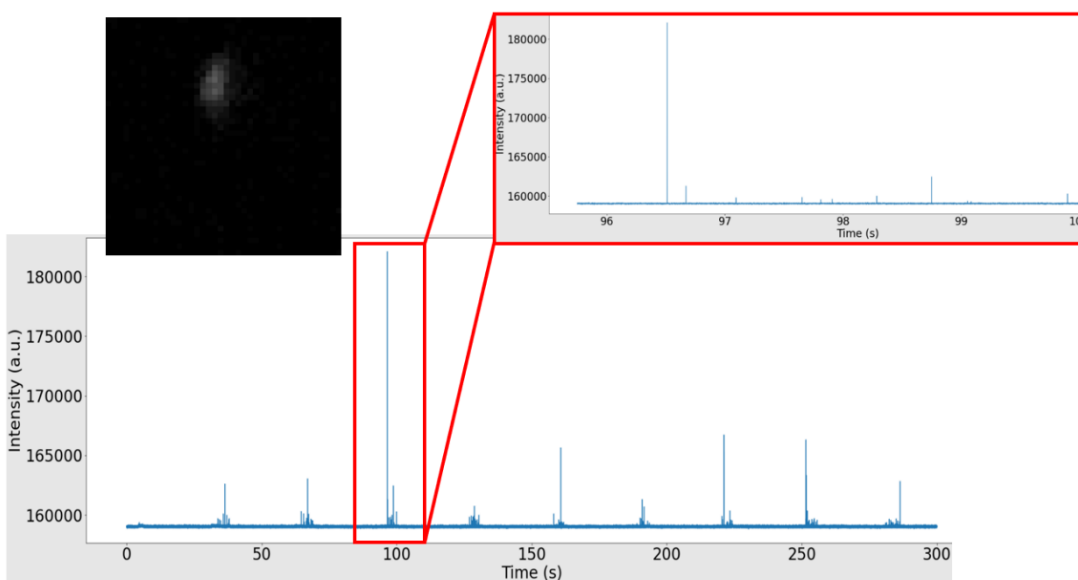
Figure 6.10. Example fluorescence time domain trace resulting from optical detection of fluorescently stained E. coli. Each peak indicates a detected bacterium.

In preparation for the one-on-one sessions, 24 LOC devices were fabricated, following the procedure outlined in Section 3.2.1, to account for one chip per group and extras in the case of any errors. Prior to each of the 12 one-on-one session, 2 µL of E. coli bacteria diluted in 1xPBS buffer, 2 µL of 1xSYBR gold, and 5 µL of 1xPBS were loaded on top of their respective inlets and preloaded into the first valve.

Additionally, the fiber coupling of the 488 nm laser into the solid-core excitation waveguide was optimized before each experiment. While monitored over a Zoom call, each group of students then remotely executed their code, and the SYBR gold intercalating dye and E. coli were pushed into the central four mixing valves and rotated to ensure complete mixing of the two fluids. The solution was then incubated for 20 minutes as per the SYBR gold staining procedure. The stained bacteria were then sequentially pushed through to the optical detection region where a 488 nm excitation laser was coupled into the chip via a solid core waveguide. Fluorescence emissions from excited bacteria were detected by a camera aligned above the detection region over a 5-minute period. The resulting video recording was analyzed frame-by-frame, where pixel intensities in the region of interest were integrated and plotted in the time domain. An example of one group's fluorescence time domain trace is shown in Figure 6.10. Each group received the results of their fluorescence detection experiment in the days following the one-on-one sessions.
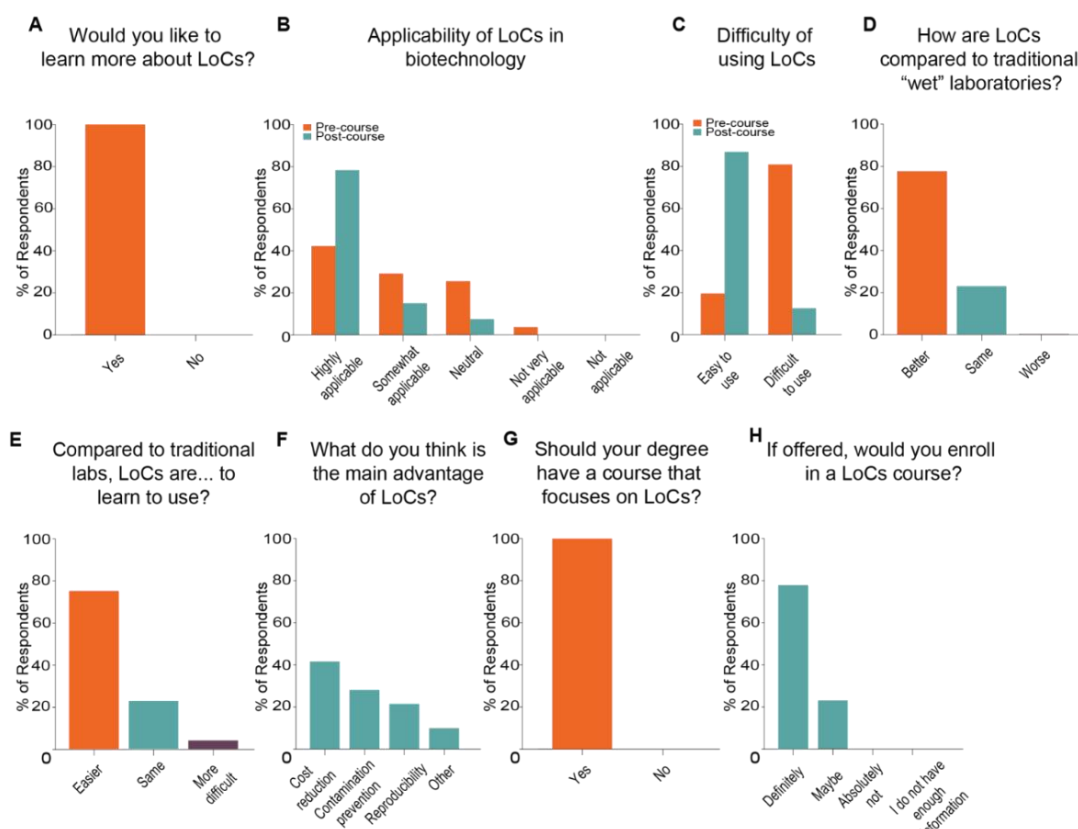
Figure 6.11. Context-aware PBL led to a higher interest in LoCs. A) Self-reported interest in learning more about LoCs. B) Perceived applicability of LoC's in biotechnology before and after the program. C) Perceived difficulty of using LoCs before and after the program. D) Perceived performance of LoCs as compared to traditional laboratories. E) Perceived ease to learn to use of LoCs as compared to traditional laboratories. F) Perceived main advantage of LoCs in biotechnology. G) Students' interest in having a LoC-specific course in their degrees. H) Self-reported interest to enroll in LoC-specific courses. Pre-course n = 42. Post-course n = 28.

In addition to measuring the success of the groups of students in completing the assigned homework, a voluntary survey was given to the students before and after the PBL experience. These surveys were generally assessed the participants' feelings towards relevant topics such as programming and LOC systems and were a combination of Likert scale, where participants selected their level of agreement with a prompt, as well as multiple choice questions. The number of pre-course surveys

received was 42, while the number of surveys received after the course was 28. Due to local regulations prohibiting the collection of identifying information, surveys were not mandatory. This also prevented matching the 28 collected post-course survey responses to the responses from the 28 participants in the pre-course survey. Because of this, we refrain from making direct statistical significance conclusions between the pre- and post-course survey responses.

In the pre-course surveys, we found that a majority (66.7%) of students felt that Latinx scientists are underrepresented in bioengineering. Notably, 45.2% of participants believed lack of exposure to relevant subjects and classes is the main obstacle. This PBL is a direct attempt at providing a solution where students can be directly exposed to and involved in high level scientific experiments. Overall, the responses of the students indicated positive engagement. From Figure 6.11, the 2-week experience led to an increased interest in LOC technologies as well as their overall difficulty of control and operation. As seen in Figure 6.12, students felt that both the theoretical and experimental portions of the PBL module were well executed, with 100% of respondents valuing the 1-on-1 session. The responses also indicate that the context and subject matter of the module was well aligned with their current degree, and that the introductory programming was useful and advanced their interest in continuing to learn how programming can benefit their current skill set. Moreover, students said that they would highly recommend peers to take this module if offered again.
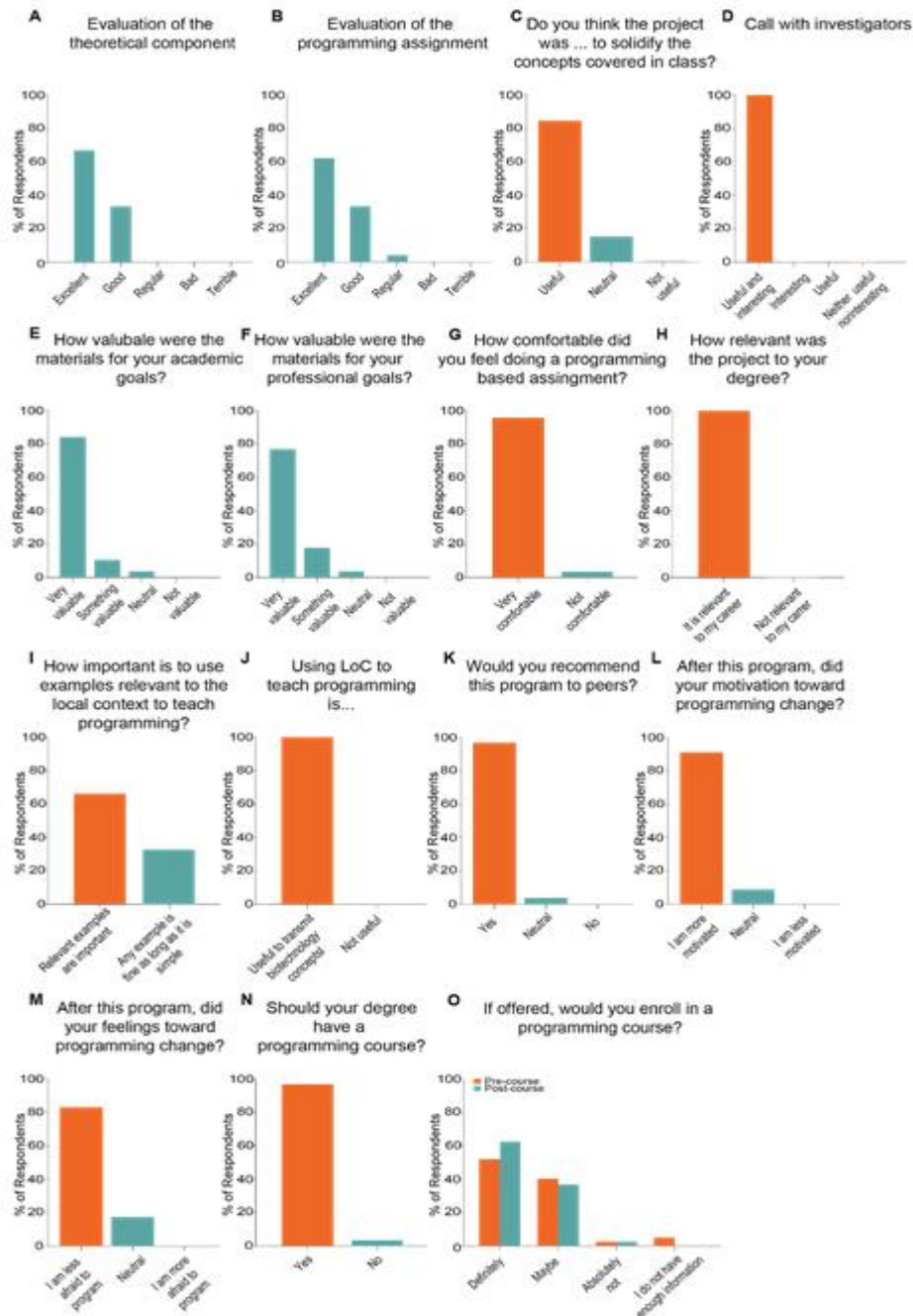
Figure 6.12. Program evaluation and prospects of careers in bioinformatics and computational biology. (A-O) Program evaluation showing the distribution of students' responses. A) Evaluation of the theoretical component of the program. B) Evaluation of the programming assignment. C) Perception of the usefulness of the programming assignment to solidify concepts. D) Perception of the usefulness of the call with investigators to receive feedback on programming assignments. E)

Perception of value of the program for academic goals. F) Perception of value of the program for professional goals. G-O) Program evaluation showing increased interest in programming and bioinformatics. G) Comfort in completing programming assignment. H) Perceived relevant of assignment to students' degrees. I) Importance of using context-aware projects in teaching. J) Perceived applicability of LoCs in teaching programming. K) Students' recommendations to their peers. L) Self-reported effects on motivation to learn to program. M) Self-reported effects on feelings toward programming. N) Student's perceptions on whether their degree should have a programming course. O) Comparison of intent to enroll in a programming course before and after this program. Pre-course n = 42. Post-course n = 28.

Students were eventually asked about additional comments regarding feedback about the experience or any comments to the team that they would like to give. Students demonstrated their excitement around the subject matter as well as their desire to learn more about LOCs and programming, some even showing interest in involvement in planning and executing future outreach opportunities. Some of the received quotes include:

- *"The classes were very interesting. I had never heard of this technology. After learning a little bit (about this technology), I want to study more programming. I feel (that learning programming) is something that I feel would simplify many procedures."* - Translated from Respondent 1.

- *"I wish you could share this project with many other young people who are interested in science. It is really impressive work."* - Translated from Respondent 2.

- *"Here in Latin America, and especially in Bolivia, this type of technology does not exist, so I am very grateful for this experience."* - Translated from Respondent 3.

- "*It is a beautiful project. (I wish you) great success in improving your work and I hope that in the future courses you can accept volunteers from different countries to develop pilot programs or experiments.*" - Translated from Respondent 4.

- "*Thank you very much for giving us this opportunity and (I) wish you success in your present and future projects. Also, how can we get involved in more activities like these?*" - Translated from Respondent 5.

In conclusion, we developed a context-aware PBL module designed for Latinx life science students in Bolivia that focused on water quality testing. This PBL outreach module demonstrates a glimpse of the possibilities of expanding high level scientific research to underserved communities via IoT integration and remote capabilities. By increasing exposure of students to introductory programming and bioinformatics studies, internet-enabled PBL can be a powerful tool in expanding the representation of underserved communities in STEM fields.

Chapter 7

Summary and Future Work

In conclusion, this thesis has presented several optofluidic devices with contributions in the fields of integrated optofluidics and biophotonics.

Firstly, the integration of an on-chip optofluidic distributed feedback laser directly with an analyte channel for biosensing on an all-PDMS platform dramatically simplifies the alignment necessary to provide excitation light in fluorescence biosensing, providing a minimum of a 10x improvement in the tolerance of optical alignment. In this application, 5mM Rhodamine 6G was dissolved in a solution of 85% ethylene glycol – 15% DI water and used to fill a distributed feedback grating dye laser with a Bragg spacing of $\Lambda = 8\,\mu m$ and corrugation depth of $d = 2.5\,\mu m$. This optofluidic dye laser was used to demonstrate low threshold lasing (52.7 μJ/cm^2) with a central lasing wavelength of 574.6 nm and a FWHM of 1.08 nm. Fluorescence detection of fluorescent microspheres was demonstrated using this DFB when integrated with a fluidic analyte source. Dynamic tunability of the output power was also shown using a pneumatic "lightvalve" switch integrated in the all-PDMS device

demonstrating attenuation of the output power by up to -8.84 dB. This fluidic light source is widely reconfigurable with the ability to use various gain media for an array of fluorescent labels. Quantum dots could also be used by colloidally suspending them in PDMS to generate a solid-core DFB grating or in solution which could enable multiple lasing wavelengths using a single pump laser. Lasing characteristics of this DFB laser could be improved in the future by using tools such as electron beam lithography (EBL) to fabricate a stamping tool where the grating period could further be reduced. This would move the resonant wavelength to a lower Bragg order, therefore increasing the reflectivity of the cavity and thus, the output power of the DFB laser [117].

Furthermore, this DFB lasing scheme was demonstrated to be scalable and applicable in multiplexed biosensing schemes through the addition of a second, identical DFB grating using 5 mM DCM dissolved in DMSO as the gain medium instead. This DFB laser demonstrated a lasing wavelength of 656.5 nm and a FWHM of 1.73 nm with a reasonable threshold fluence of 307.6 μJ/cm^2. The two lasers were operated simultaneously and used to conduct multiplexed detection of two types of fluorescent microspheres which served as proxy analytes for analogously stained fluorescent biomarkers. Further studies into the use of other fluorescent dyes in additional or the same channels could continue to scale the multiplexing capabilities of this platform and could reasonably achieve 5-10x multiplexing. This spatial multiplexing scheme could also be advanced with integration with other multiplexing methods such as velocity multiplexing whereby an additional analyte channel is placed

in parallel, and biomarkers are flowed at a different speed to produce a distinguishable Δt value in the fluorescence time domain trace [95].

Integration of this light source into an all-in-one optofluidic lab-on-chip system combining sample preparation with a coherent light source and optical detection was then presented. Sample preparation was conducted in a network of fifteen pneumatically operated valves controlling the flow of assay reagents throughout the device, enabling sequential and complex assays to be conducted. The Rhodamine 6G DFB laser was integrated as the coherent light source and a tapered solid-core waveguide carried the laser emission to the orthogonal analyte channel to provide optical excitation. This all-in-one PDMS-based LOC was then used to conduct nonspecific detection of dsDNA as well as specific detection of Zika nucleic acids using magnetic bead-based assays. This work presents further progress towards a highly sensitive and selective point-of-care biosensor that can aid in curbing the impact of future disease outbreaks.

Lastly, optical detection of fluorescently stained extracellular vesicles that were derived from neuronal organoids was presented. Fluorescence detection of extracellular vesicles was conducted using both a lipophilic stain as well as an intercalating nucleic acid stain. This provides foundational proof-of-concept for further work in detecting specific biomarkers contained on or within extracellular vesicles or subgroups of extracellular vesicles. More specific fluorescence detection could include fluorescence labeling of surface proteins such as CD63, CD81, or CD9 that are essential in biosynthesis of EVs. Additionally, the devices presented in this work have

demonstrated the ability to progress the level of integration of optofluidic devices into

existing microfluidic environments used to culture and grow organoids [98].

Appendix A: SU-8 and PDMS Fabrication Protocols

-----------------------------------SU-8 Master Fabrication---------------------------------

- Spray blank silicon wafers with isopropyl alcohol (IPA)

- Blow dry with nitrogen

- Dry in 60 °C oven overnight

Next day

- RIE at 80% power for 10 minutes

    o (recipe: 80p_10min)

- Cover spin coater with aluminum foil

- Load wafer onto spin coater

-----------------------------------Waveguide Layer---

- Carefully pour SU-8 2005 onto wafer until about 2/3 of the wafer is covered.

- Use the following spin procedure programmed into spin coater

- While wafer is spinning, program hotplates to 65°C and 95°C

SU-8 2005 Spin Protocol

Step	Speed (RPM)	Time (sec)	Ramp (RPM/s)
1	500	10	100
2	3500	60	300

3	0	0	500

- Follow pre-exposure bake protocol outlined below:

SU-8 2005 Pre-exposure Bake

Step	Temperature (°C)	Time (min)
1	65	1
2	95	6
3	65	1
4	25	3

- Conduct edge bead removal using acetone loaded into a syringe with a small gauge needle (30 gauge):
    - While wafer is spinning at 700 RPM, remove ~2-3 mm of SU-8 from the outside edge of the wafer

Step	Speed (RPM)	Time (sec)	Ramp (RPM/s)
1	700	30	100
2	1500	5	500
3	2500	10	1000
4	0	0	500

- Follow SOP for Karl Suss mask aligner to turn on and then load the waveguide layer chrome mask

- Measure output flux from UV lamp using power meter

- Load and align SU-8 coated wafer and bring wafer into contact with mask

- Ensure "Hard Contact" is enabled and then expose wafer with total dosage of 69.8 mJ/cm^2

- Follow post-exposure bake protocol outlined below:

Step	Temperature (°C)	Time (min)
1	65	6
2	95	6
3	65	7
4	25	10

- Develop wafer using SU-8 developer

  o Alternate between approximately 8 seconds of developer and wash with IPA to prevent washing away any features

  o Check features under microscope to ensure fully developed

- Hard bake @ 200°C for 5 minutes to reflow SU-8

  o Ramp wafer to 65°C first for 5 minutes

  o This can help with cracked features

---------------------------------Pneumatic Layer---

- Carefully pour SU-8 2025 onto wafer until about 2/3 of wafer is covered

- Use following spin procedure programmed into spin coater

SU-8 2025 Spin Protocol

Step	Speed (RPM)	Time (sec)	Ramp (RPM/s)
1	500	10	100
2	3000	120	300
3	0	0	500

- Follow pre-exposure bake procedure outlined below:

SU-8 2025 Pre-exposure Bake

Step	Temperature (°C)	Time (min)
1	65	5
2	95	30
3	65	5
4	25	5

- Conduct edge bead removal using same protocol as described in the "Waveguide Layer" section

- Load pneumatic layer chrome mask into Karl Suss mask aligner

- Load and align SU-8 2025 coated wafer and bring into contact with mask

- Ensure "Hard Contact" mode is enabled and exposure wafer with total dosage of 146.3 mJ/cm^2.

- Follow post-exposure bake protocol outlined below:

Step	Temperature (°C)	Time (min)
1	65	5
2	95	15
3	65	10
4	25	10

- Develop wafer using SU-8 developer

  o Alternate between approximately 30 seconds of developer and wash with IPA to prevent washing away any features

  o Check features under microscope to ensure fully developed

- Hard bake @ 200°C for 5 minutes to reflow SU-8

  o Ramp wafer to 65°C first for 5 minutes

- This can help with cracked features

--------------------------------PDMS Fabrication---

- Mix 12 grams of 5:1 PDMS and two cups of 55 grams of 10:1 PDMS

  o For devices with a pneumatic waver, mix an additional cup of 11 grams of 10:1 PDMS

- Degass PDMS for 2 hours in the PDMS desiccator

    o This can be accelerated by toggling the vacuum of the desiccator

- Ensure waveguide, pneumatic, and blank wafers are clean

    o Wash with IPA and blow dry if necessary

- Silanize wafers for 40 minutes in silane desiccator using 3-4 drops of silane

    o Keep wafers as far away from silane source as possible to keep wafers clean

    o Blow dry wafers after silane treatment to remove any particles on surface

- Use the following spin procedure for spinning 5:1 PDMS:

Step	Speed (RPM)	Time (sec)	Ramp (RPM/s)
1	500	10	100
2	5000	900	600
3	0	0	500

- Cure 5:1 PDMS-coated wafer in oven for 2 hours

If not using a pneumatic layer:

- Load 5:1 PDMS-coated wafer into thin, circular acrylic mold

- Pour 10:1 PDMS close to surface to prevent air bubbles

- Load blank silicon wafer into circular acrylic mold and pour 10:1 PDMS

- Cure both wafers in oven for 2 hours (overnight if possible)

- Carefully separate waveguide layer from master and tape the exposed PDMS

- Mark location of fluidic inlets using a sharpie and punch inlets using a 1 mm biopsy punch

- Separate blank layer from silicon wafer carefully using IPA and load into the RIE

- Remove tape from the waveguide layer and load into RIE alongside blank

- Treat with O_2 plasma for 30 seconds

    o Recipe: PDMS_bonding

- Carefully remove both layers and bond from one side to the other to prevent trapping air bubbles

If using pneumatic layer:

- Load 5:1 PDMS-coated wafer back into spin coater and spin the 11 g of 10:1 PDMS using the following program:

Step	Speed (RPM)	Time (sec)	Ramp (RPM/s)
1	500	10	100
2	1000	300	500
3	0	0	500

- While wafer is spinning, load pneumatic silicon master and blank silicon wafer into thin, circular acrylic molds

- Pour 10:1 PDMS for both wafers close to surface to prevent bubbles

- Carefully place acrylic plate with polygons over the top of pneumatic layer without creating bubbles and then secure with screws

- Cure both the waveguide wafer, pneumatic wafer, and blank layer in oven for 2 hours (overnight if possible)

Next day:

- Remove acrylic backing, silicon pneumatic master, and circular mold carefully using IPA
    - PDMS pneumatic layer should remain in contact with acrylic plate with polygons

- Load pneumatic layer and waveguide layer into OAI mask aligner
    - Use substrate vacuum to keep waveguide wafer in place
    - Roughly align and mark placement of wafer and mask

- Load both layers into RIE and plasma treat for 30 seconds
    - Recipe: PDMS_bonding

- Place pneumatic layer and waveguide wafer back into OAI mask aligner
    - Realign and then carefully bring the waveguide wafer into contact with pneumatic layer

- Turn off substrate vacuum and remove bonded layers from mask aligner and cure in oven for 2 hours (overnight if possible)

- Separate acrylic polygon plate and silicon waveguide master and tape exposed waveguide surface

- Mark fluidic and pneumatic inlets/outlets using a sharpie and punch using a 1 mm biopsy punch

- Separate blank layer from silicon wafer

For chips only requiring positive pressure actuation:

- Remove tape and treat waveguide layer and blank layer with O_2 plasma in RIE for 30 seconds

- Carefully remove layers and bond together

For automatons or devices needing negative pressure actuation, cut chips individually and cut identical shapes out of blank layer.

- Remove tape and treat each chip and corresponding blank with O_2 plasma in RIE for 30 seconds
    o Recipe: PDMS_bonding

- Place top half of chip on vacuum line such that vacuum is only applied to pneumatic inlets

- Carefully overlay blank on exposed surface and bond chip together

Appendix B: Rhodamine 6G Photophysical Constants

The following table is a list of typical photophysical parameters for Rhodamine 6G assuming a pump wavelength of 532 nm and a lasing wavelength of ~580 nm [91].

$\sigma_a(\lambda_P)$ (cm^2)	3.8×10^{-16}
$\sigma_a(\lambda_L)$ (cm^2)	1×10^{-19}
$\sigma_{em}(\lambda_L)$ (cm^2)	1.2×10^{-16}
$\sigma_T(\lambda_L)$ (cm^2)	1×10^{-17}
τ_{sp} (ns)	5
$1/k_{ST}$ (ns)	100
τ_T (ns)	100

Appendix C: Laser Dyes

The following table is a list of dye families that have been demonstrated in dye laser applications along with the range of lasing wavelengths achieved. Use of different dyes including combinations of dyes could enable greater multiplexing capabilities of on-chip dye lasers.

Laser Dye Family	Emission Range (nm)
Coumarins	435-555
Xanthenes (Rhodamines)	560-800
Oxazine dyes	650-750
Pyrromethenes	525-575

Appendix D: Dual DFB Optical Setup

The following is a photograph of the dual DFB laser optical setup used to demonstrate two optofluidic DFB dye lasers operated simultaneously for multiplexed fluorescence sensing:
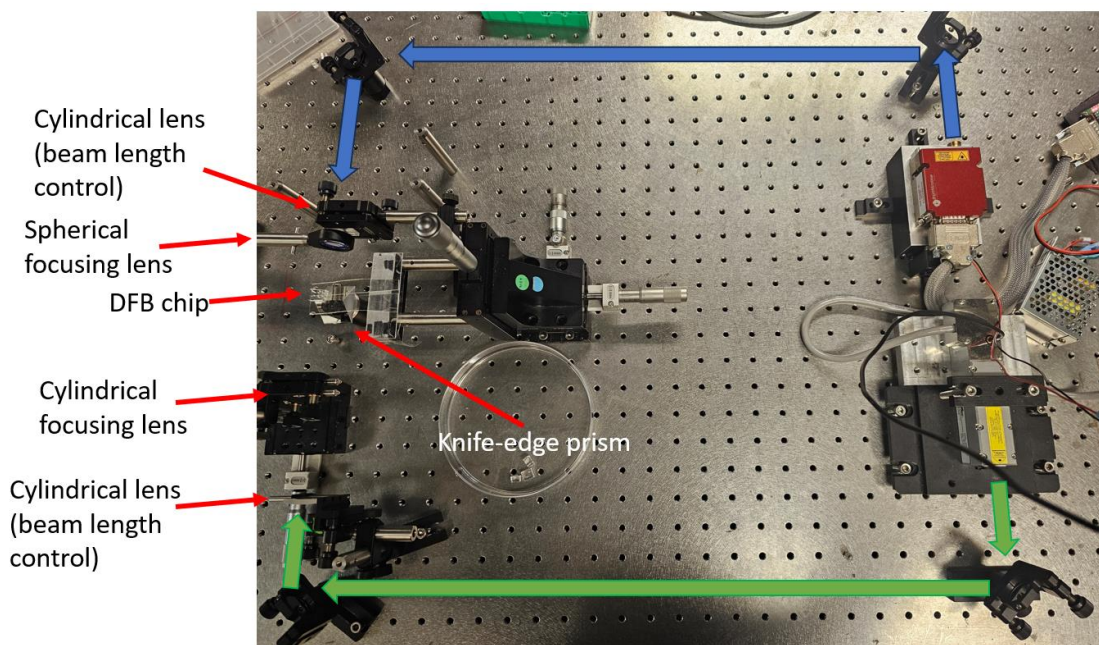
The camera used for alignment and collection was removed for the picture as it blocks visibility of other optics.

Appendix E: Fluorescence Stains and Fluorescent Beads

Below is a table listing the fluorescent markers used in this thesis along with their respective excitation and emission maxima.

Fluorescent Marker	Excitation Max (nm)	Emission Max (nm)
Red Fluorescent Beads	580	605
Flash Red Fluorescent Beads	660	690
vFRed	465	490
SYBR Gold	495	539

Bibliography

[1] P. Yager *et al.*, 'Microfluidic diagnostic technologies for global public health', *Nature 2006 442:7101*, vol. 442, no. 7101, pp. 412–418, Jul. 2006, doi: 10.1038/nature05064.

[2] A. R. Hawkins and H. Schmidt, *Handbook of optofluidics*. 2010. doi: 10.1201/9781420093551.

[3] C. Monat, P. Domachuk, and B. J. Eggleton, 'Integrated optofluidics: A new river of light', *Nature Photonics*. 2007. doi: 10.1038/nphoton.2006.96.

[4] P. Minzioni *et al.*, 'Roadmap for optofluidics', *Journal of Optics*, vol. 19, no. 9, p. 093003, Aug. 2017, doi: 10.1088/2040-8986/AA783B.

[5] A. Stambaugh, J. W. Parks, M. A. Stott, G. G. Meena, A. R. Hawkins, and H. Schmidt, 'Optofluidic multiplex detection of single SARS-CoV-2 and influenza A antigens using a novel bright fluorescent probe assay', *Proc Natl Acad Sci U S A*, vol. 118, no. 20, May 2021, doi: 10.1073/PNAS.2103480118/SUPPL_FILE/PNAS.2103480118.SAPP.PDF.

[6] J. Wang, S. A. Maier, A. Tittl, J. Wang, S. A. Maier, and A. Tittl, 'Trends in Nanophotonics-Enabled Optofluidic Biosensors', *Adv Opt Mater*, vol. 10, no. 7, p. 2102366, Apr. 2022, doi: 10.1002/ADOM.202102366.

[7] X. Fan and I. M. White, 'Optofluidic Microsystems for Chemical and Biological Analysis', *Nat Photonics*, vol. 5, no. 10, p. 591, Oct. 2011, doi: 10.1038/NPHOTON.2011.206.

[8] T. Sano, J. Black, S. Mitchell, H. Zhang, and H. Schmidt, 'Pneumatically tunable optofluidic DFB dye laser using corrugated sidewalls', *Opt Lett*, 2020, doi: 10.1364/ol.404303.

[9] T. Sano, R. Losakul, and H. Schmidt, 'Dual optofluidic distributed feedback dye lasers for multiplexed biosensing applications', *Scientific Reports 2023 13:1*, vol. 13, no. 1, pp. 1–8, Oct. 2023, doi: 10.1038/s41598-023-42671-4.

[10] T. Sano, H. Zhang, R. Losakul, and H. Schmidt, 'All-in-One Optofluidic Chip for Molecular Biosensing Assays', *Biosensors (Basel)*, vol. 12, no. 7, Jul. 2022, doi: 10.3390/BIOS12070501.

[11]   M. Suran, 'Preparing Hospitals' Medical Oxygen Delivery Systems for a Respiratory "Twindemic"', *JAMA*, vol. 327, no. 5, pp. 411–413, Feb. 2022, doi: 10.1001/jama.2021.23392.

[12]   G. G. Meena *et al.*, '7X multiplexed, optofluidic detection of nucleic acids for antibiotic-resistance bacterial screening', *Optics Express, Vol. 28, Issue 22, pp. 33019-33027*, vol. 28, no. 22, pp. 33019–33027, Oct. 2020, doi: 10.1364/OE.402311.

[13]   H. Cai, M. A. Stott, D. Ozcelik, J. W. Parks, A. R. Hawkins, and H. Schmidt, 'On-chip wavelength multiplexed detection of cancer DNA biomarkers in blood', *Biomicrofluidics*, 2016, doi: 10.1063/1.4968033.

[14]   S. Mandal, J. M. Goddard, and D. Erickson, 'A multiplexed optofluidic biomolecular sensor for low mass detection', *Lab Chip*, vol. 9, no. 20, pp. 2924–2932, Oct. 2009, doi: 10.1039/B907826F.

[15]   Z. Zhao *et al.*, 'Organoids', *Nature Reviews Methods Primers 2022 2:1*, vol. 2, no. 1, pp. 1–21, Dec. 2022, doi: 10.1038/s43586-022-00174-y.

[16]   'Organoids: A new window into disease, development and discovery | Harvard Stem Cell Institute (HSCI)'. Accessed: Oct. 23, 2023. [Online]. Available: https://hsci.harvard.edu/organoids

[17]   S. A. Yi, Y. Zhang, C. Rathnam, T. Pongkulapa, and K. B. Lee, 'Bioengineering approaches for the advanced organoid research', *Adv. Mater.*, vol. 33, no. 45, Nov. 2021, doi: 10.1002/adma.202007949.

[18]   G. Raposo and W. Stoorvogel, 'Extracellular vesicles: Exosomes, microvesicles, and friends', *Journal of Cell Biology*, vol. 200, no. 4, pp. 373–383, Feb. 2013, doi: 10.1083/JCB.201211138.

[19]   M. P. Zaborowski, L. Balaj, X. O. Breakefield, and C. P. Lai, 'Extracellular Vesicles: Composition, Biological Relevance, and Methods of Study', *Bioscience*, vol. 65, no. 8, pp. 783–797, Jul. 2015, doi: 10.1093/BIOSCI/BIV084.

[20]   L. M. Doyle and M. Z. Wang, 'Overview of Extracellular Vesicles, Their Origin, Composition, Purpose, and Methods for Exosome Isolation and Analysis', *Cells*, vol. 8, no. 7, Jul. 2019, doi: 10.3390/CELLS8070727.

[21]   M. Yáñez-Mó *et al.*, 'Biological properties of extracellular vesicles and their physiological functions', *J Extracell Vesicles*, vol. 4, no. 2015, pp. 1–60, 2015, doi: 10.3402/JEV.V4.27066.

[22]   M. P. Bebelman, M. J. Smit, D. M. Pegtel, and S. R. Baglio, 'Biogenesis and function of extracellular vesicles in cancer', *Pharmacol Ther*, vol. 188, pp. 1–11, Aug. 2018, doi: 10.1016/J.PHARMTHERA.2018.02.013.

[23] M. Rahman *et al.*, 'A Critical Review on the Sensing, Control, and Manipulation of Single Molecules on Optofluidic Devices', *Micromachines 2022, Vol. 13, Page 968*, vol. 13, no. 6, p. 968, Jun. 2022, doi: 10.3390/MI13060968.

[24] D. Psaltis, S. R. Quake, and C. Yang, 'Developing optofluidic technology through the fusion of microfluidics and optics', *Nature 2006 442:7101*, vol. 442, no. 7101, pp. 381–386, Jul. 2006, doi: 10.1038/nature05060.

[25] Y. Fainman, D. Psaltis, and C. Yang, *Optofluidics: Fundamentals, Devices, and Applications*, no. 2. McGraw-Hill Education, 2010. Accessed: Feb. 22, 2023. [Online]. Available: https://www.accessengineeringlibrary.com/content/book/9780071601566

[26] J. W. Parks *et al.*, 'Integration of programmable microfluidics and on-chip fluorescence detection for biosensing applications', *Biomicrofluidics*, 2014, doi: 10.1063/1.4897226.

[27] Z. Cai, W. Qiu, G. Shao, and W. Wang, 'A new fabrication method for all-PDMS waveguides', *Sens Actuators A Phys*, 2013, doi: 10.1016/j.sna.2013.09.019.

[28] J. Wang, M. M. Sanchez, Y. Yin, R. Herzer, L. Ma, and O. G. Schmidt, 'Silicon-Based Integrated Label-Free Optofluidic Biosensors: Latest Advances and Roadmap', *Adv Mater Technol*, vol. 5, no. 6, p. 1901138, Jun. 2020, doi: 10.1002/ADMT.201901138.

[29] M. Ramezannezhad, A. Nikfarjam, H. Hajghassem, M. M. Akram, and M. Gazmeh, 'A micro optofluidic system for toluene detection application', *Microelectron Eng*, vol. 222, p. 111204, Feb. 2020, doi: 10.1016/J.MEE.2019.111204.

[30] G. Luka *et al.*, 'Microfluidics Integrated Biosensors: A Leading Technology towards Lab-on-a-Chip and Sensing Applications', *Sensors (Basel)*, vol. 15, no. 12, pp. 30011–30031, Dec. 2015, doi: 10.3390/S151229783.

[31] J. W. Parks *et al.*, 'Hybrid optofluidic integration', *Lab Chip*, 2013, doi: 10.1039/c3lc50818h.

[32] I. Miranda *et al.*, 'Properties and Applications of PDMS for Biomedical Engineering: A Review', *Journal of Functional Biomaterials 2022, Vol. 13, Page 2*, vol. 13, no. 1, p. 2, Dec. 2021, doi: 10.3390/JFB13010002.

[33] M. P. Wolf, G. B. Salieb-Beugelaar, and P. Hunziker, 'PDMS with designer functionalities—Properties, modifications strategies, and applications', *Prog Polym Sci*, vol. 83, pp. 97–134, Aug. 2018, doi: 10.1016/J.PROGPOLYMSCI.2018.06.001.

[34] J. Kim, M. Kang, E. C. Jensen, and R. A. Mathies, 'Lifting gate polydimethylsiloxane microvalves and pumps for microfluidic control', *Anal Chem*, vol. 84, no. 4, pp.

2067–2071, Feb. 2012, doi: 10.1021/AC202934X/SUPPL_FILE/AC202934X_SI_002.PDF.

[35]   J. W. Parks and H. Schmidt, 'Flexible optofluidic waveguide platform with multi-dimensional reconfigurability', *Sci Rep*, 2016, doi: 10.1038/srep33008.

[36]   J. Godin, C. H. Chen, S. H. Cho, W. Qiao, F. Tsai, and Y. H. Lo, 'Microfluidics and photonics for bio-System-on-a-Chip: A review of advancements in technology towards a microfluidic flow cytometry chip', *Journal of Biophotonics*. 2008. doi: 10.1002/jbio.200810018.

[37]   G. M. Whitesides, 'The origins and the future of microfluidics', *Nature 2006 442:7101*, vol. 442, no. 7101, pp. 368–373, Jul. 2006, doi: 10.1038/nature05058.

[38]   J. K. Nunes and H. A. Stone, 'Introduction: Microfluidics', *Chem Rev*, vol. 122, no. 7, pp. 6919–6920, Apr. 2022, doi: 10.1021/ACS.CHEMREV.2C00052.

[39]   A. J. DeMello, 'Control and detection of chemical reactions in microfluidic systems', *Nature 2006 442:7101*, vol. 442, no. 7101, pp. 394–402, Jul. 2006, doi: 10.1038/nature05062.

[40]   A. K. Au, W. Huynh, L. F. Horowitz, and A. Folch, '3D-printed microfluidics', *Angew. Chem. Int. Ed.*, vol. 55, no. 12, pp. 3862–3881, Mar. 2016, doi: 10.1002/anie.201504382.

[41]   C. M. B. Ho, S. H. Ng, K. H. H. Li, and Y. J. Yoon, '3D printed microfluidics for biological applications', *Lab Chip*, vol. 15, no. 18, pp. 3627–3637, Jul. 2015, doi: 10.1039/c5lc00685f.

[42]   S. M. Hampson, W. Rowe, S. D. R. Christie, and M. Platt, '3D printed microfluidic device with integrated optical sensing for particle analysis', *Sensors Actuators B Chem.*, vol. 256, pp. 1030–1037, Mar. 2018, doi: 10.1016/j.snb.2017.10.041.

[43]   H. Wang, A. Enders, J. A. Preuss, J. Bahnemann, A. Heisterkamp, and M. L. Torres-Mapa, '3D printed microfluidic lab-on-a-chip device for fiber-based dual beam optical manipulation', *Scientific Reports 2021 11:1*, vol. 11, no. 1, pp. 1–12, Jul. 2021, doi: 10.1038/s41598-021-93205-9.

[44]   K. Ward and Z. H. Fan, 'Mixing in microfluidic devices and enhancement methods', *Journal of Micromechanics and Microengineering*, vol. 25, no. 9, 2015, doi: 10.1088/0960-1317/25/9/094001.

[45]   C. Y. Lee, C. L. Chang, Y. N. Wang, and L. M. Fu, 'Microfluidic Mixing: A Review', *Int J Mol Sci*, vol. 12, no. 5, p. 3263, May 2011, doi: 10.3390/IJMS12053263.

[46] M. T. Guo, A. Rotem, J. A. Heyman, and D. A. Weitz, 'Droplet microfluidics for high-throughput biological assays', *Lab Chip*, vol. 12, no. 12, pp. 2146–2155, Jun. 2012, doi: 10.1039/C2LC21147E.

[47] M. Zagnoni and J. M. Cooper, 'Droplet microfluidics for high-throughput analysis of cells and particles', *Methods Cell Biol*, vol. 102, pp. 23–48, 2011, doi: 10.1016/B978-0-12-374912-3.00002-X.

[48] A. M. Kaushik, K. Hsieh, and T. H. Wang, 'Droplet microfluidics for high-sensitivity and high-throughput detection and screening of disease biomarkers', *Wiley Interdiscip Rev Nanomed Nanobiotechnol*, vol. 10, no. 6, Nov. 2018, doi: 10.1002/wnan.1522.

[49] P. E. Guevara-Pantoja, R. J. Jiménez-Valdés, J. L. García-Cordero, and G. A. Caballero-Robledo, 'Pressure-actuated monolithic acrylic microfluidic valves and pumps', *Lab Chip*, vol. 18, no. 4, pp. 662–669, Feb. 2018, doi: 10.1039/C7LC01337J.

[50] E. C. Jensen, B. P. Bhat, and R. A. Mathies, 'A digital microfluidic platform for the automation of quantitative biomolecular assays', *Lab Chip*, vol. 10, no. 6, pp. 685–691, 2010, doi: 10.1039/B920124F.

[51] G. G. Meena *et al.*, 'Integration of sample preparation and analysis into an optofluidic chip for multi-target disease detection', *Lab Chip*, 2018, doi: 10.1039/c8lc00966j.

[52] Z. Liao *et al.*, 'Microfluidic chip coupled with optical biosensors for simultaneous detection of multiple analytes: A review', *Biosens Bioelectron*, vol. 126, pp. 697–706, Feb. 2019, doi: 10.1016/J.BIOS.2018.11.032.

[53] J. P. Lafleur, A. Jönsson, S. Senkbeil, and J. P. Kutter, 'Recent advances in lab-on-a-chip for biosensing applications', *Biosens Bioelectron*, vol. 76, pp. 213–233, Feb. 2016, doi: 10.1016/J.BIOS.2015.08.003.

[54] G. Luka *et al.*, 'Microfluidics integrated biosensors: A leading technology towards lab-on-A-chip and sensing applications', *Sensors (Switzerland)*, vol. 15, no. 12, pp. 30011–30031, Dec. 2015, doi: 10.3390/S151229783.

[55] G. P. Nikoleli, C. G. Siontorou, D. P. Nikolelis, S. Bratakou, S. Karapetis, and N. Tzamtzis, 'Biosensors Based on Microfluidic Devices Lab-on-a-Chip and Microfluidic Technology', *Nanotechnology and Biosensors*, pp. 375–394, Jan. 2018, doi: 10.1016/B978-0-12-813855-7.00013-1.

[56] C. Chircov, A. C. Bîrcă, A. M. Grumezescu, and E. Andronescu, 'Biosensors-on-Chip: An Up-to-Date Review', *Molecules*, vol. 25, no. 24, Dec. 2020, doi: 10.3390/MOLECULES25246013.

[57] N. Bhalla, P. Jolly, N. Formisano, and P. Estrela, 'Introduction to biosensors.', *Essays Biochem*, vol. 60, no. 1, pp. 1–8, 2016, doi: 10.1042/EBC20150001.

[58] Z. Liao *et al.*, 'Recent advances in microfluidic chip integrated electronic biosensors for multiplexed detection', *Biosens Bioelectron*, vol. 121, pp. 272–280, Dec. 2018, doi: 10.1016/J.BIOS.2018.08.061.

[59] S. M. Shadman *et al.*, 'Aptamer-based electrochemical biosensors', *Electrochemical Biosensors*, pp. 213–251, Jan. 2019, doi: 10.1016/B978-0-12-816491-4.00008-5.

[60] Y. Xiao, A. A. Lubin, A. J. Heeger, and K. W. Plaxco, 'Label-Free Electronic Detection of Thrombin in Blood Serum by Using an Aptamer-Based Sensor', *Angewandte Chemie International Edition*, vol. 44, no. 34, pp. 5456–5459, Aug. 2005, doi: 10.1002/ANIE.200500989.

[61] C. Fan, K. W. Plaxco, and A. J. Heeger, 'Electrochemical interrogation of conformational changes as a reagentless method for the sequence-specific detection of DNA', *Proc Natl Acad Sci U S A*, vol. 100, no. 16, pp. 9134–9137, Aug. 2003, doi: 10.1073/PNAS.1633515100.

[62] G. Gervinskas, S. Juodkazis, and D. J. Day, 'Optofluidic Fabry-Pérot sensor for water solutions at high flow rates', *Optical Materials Express, Vol. 2, Issue 3, pp. 279-286*, vol. 2, no. 3, pp. 279–286, Mar. 2012, doi: 10.1364/OME.2.000279.

[63] C. Szydzik *et al.*, 'An automated optofluidic biosensor platform combining interferometric sensors and injection moulded microfluidics', *Lab Chip*, vol. 17, no. 16, pp. 2793–2804, Aug. 2017, doi: 10.1039/C7LC00524E.

[64] T. Arfin, 'Emerging trends in lab-on-a-chip for biosensing applications', *Functionalized Nanomaterials Based Devices for Environmental Applications*, pp. 199–218, Jan. 2021, doi: 10.1016/B978-0-12-822245-4.00008-8.

[65] M. C. Estevez, M. Alvarez, and L. M. Lechuga, 'Integrated optical devices for lab-on-a-chip biosensing applications', *Laser Photon Rev*, vol. 6, no. 4, pp. 463–487, Jul. 2012, doi: 10.1002/LPOR.201100025.

[66] A. M. Foudeh, T. Fatanat Didar, T. Veres, and M. Tabrizian, 'Microfluidic designs and techniques using lab-on-a-chip devices for pathogen detection for point-of-care diagnostics', *Lab on a Chip*. 2012. doi: 10.1039/c2lc40630f.

[67] S. Mukherji and D. Mondal, 'Lab-on-chip (LOC) devices for point of care (POC) applications', *Medical Biosensors for Point of Care (POC) Applications*, pp. 99–131, Jan. 2017, doi: 10.1016/B978-0-08-100072-4.00005-8.

[68] N. I. Khan and E. Song, 'Lab-on-a-Chip Systems for Aptamer-Based Biosensing', *Micromachines (Basel)*, vol. 11, no. 2, Feb. 2020, doi: 10.3390/MI11020220.

[69]   X. Weng and S. Neethirajan, 'A microfluidic biosensor using graphene oxide and aptamer-functionalized quantum dots for peanut allergen detection', *Biosens Bioelectron*, vol. 85, pp. 649–656, Nov. 2016, doi: 10.1016/J.BIOS.2016.05.072.

[70]   G. Persichetti, I. A. Grimaldi, G. Testa, and R. Bernini, 'Multifunctional optofluidic lab-on-chip platform for Raman and fluorescence spectroscopic microfluidic analysis', *Lab Chip*, vol. 17, no. 15, pp. 2631–2639, Jul. 2017, doi: 10.1039/C7LC00460E.

[71]   M. P. Bhat, M. Kurkuri, D. Losic, M. Kigga, and T. Altalhi, 'New optofluidic based lab-on-a-chip device for the real-time fluoride analysis', *Anal Chim Acta*, vol. 1159, p. 338439, May 2021, doi: 10.1016/J.ACA.2021.338439.

[72]   Y. Chen *et al.*, 'Optofluidic microcavities: Dye-lasers and biosensors', *Biomicrofluidics*, vol. 4, no. 4, p. 043002, Dec. 2010, doi: 10.1063/1.3499949.

[73]   X. Wu, M. K. K. Oo, K. Reddy, Q. Chen, Y. Sun, and X. Fan, 'Optofluidic laser for dual-mode sensitive biomolecular detection with a large dynamic range', *Nat Commun*, vol. 5, no. 1, p. 3779, 2014, doi: 10.1038/ncomms4779.

[74]   Z. Li, Z. Zhang, A. Scherer, and D. Psaltis, 'Mechanically tunable optofluidic distributed feedback dye laser', *Opt Express*, vol. 14, no. 22, p. 10494, Oct. 2006, doi: 10.1364/oe.14.010494.

[75]   B. Helbo, A. Kristensen, and A. Menon, 'A micro-cavity fluidic dye laser', *Journal of Micromechanics and Microengineering*, 2003, doi: 10.1088/0960-1317/13/2/320.

[76]   Y. Sun, J. D. Suter, and X. Fan, 'Robust integrated optofluidic-ring-resonator dye lasers', *Opt Lett*, 2009, doi: 10.1364/ol.34.001042.

[77]   T. Zhang *et al.*, 'Generation of optofluidic laser in stable fiber Fabry–Pérot microcavities', *Opt Commun*, vol. 475, p. 126234, 2020, doi: https://doi.org/10.1016/j.optcom.2020.126234.

[78]   H. Zhang, P. Palit, Y. Liu, S. Vaziri, and Y. Sun, 'Reconfigurable Integrated Optofluidic Droplet Laser Arrays', *ACS Appl Mater Interfaces*, 2020, doi: 10.1021/acsami.0c05967.

[79]   Y. Chen, Z. Li, M. D. Henry, and A. Scherer, 'Optofluidic circular grating distributed feedback dye laser', *Appl Phys Lett*, 2009, doi: 10.1063/1.3186786.

[80]   M. Gersborg-Hansen and A. Kristensen, 'Tunability of optofluidic distributed feedback dye lasers', *Opt Express*, 2007, doi: 10.1364/oe.15.000137.

[81] Z. Li, Z. Zhang, T. Emery, A. Scherer, and D. Psaltis, 'Single mode optofluidic distributed feedback dye laser', *Opt Express*, vol. 14, no. 2, p. 696, Jan. 2006, doi: 10.1364/OPEX.14.000696.

[82] M. Gersborg-Hansen and A. Kristensen, 'Optofluidic third order distributed feedback dye laser', *Appl Phys Lett*, vol. 89, no. 10, 2006, doi: 10.1063/1.2345602.

[83] S. Balslev and A. Kristensen, 'Microfluidic single-mode laser using high-order Bragg grating and antiguiding segments', *Opt Express*, vol. 13, no. 1, p. 344, Jan. 2005, doi: 10.1364/opex.13.000344.

[84] W. Song and D. Psaltis, 'Pneumatically tunable optofluidic dye laser', *Appl Phys Lett*, vol. 96, no. 8, p. 081101, Feb. 2010, doi: 10.1063/1.3324885.

[85] F. M. Zehentbauer *et al.*, 'Fluorescence spectroscopy of Rhodamine 6G: Concentration and solvent effects', *Spectrochim Acta A Mol Biomol Spectrosc*, 2014, doi: 10.1016/j.saa.2013.10.062.

[86] J. A. Black, 'Chip Scale Optofluidic Devices'. 2018. Accessed: Nov. 12, 2023. [Online]. Available: https://escholarship.org/uc/item/2qm4078x

[87] M. Gersborg-Hansen, S. Balslev, N. A. Mortensen, and A. Kristensen, 'Bleaching and diffusion dynamics in optofluidic dye lasers', *Appl Phys Lett*, vol. 90, no. 14, 2007, doi: 10.1063/1.2718503.

[88] A. Penzkofer and Y. Lu, 'Fluorescence quenching of rhodamine 6G in methanol at high concentration', *Chem Phys*, 1986, doi: 10.1016/0301-0104(86)80041-6.

[89] K. H. Drexhage, 'FLUORESCENCE EFFICIENCY OF LASER DYES.', *J Res Natl Bur Stand Sect A Phys Chem*, 1976, doi: 10.6028/jres.080A.044.

[90] Z. Li and D. Psaltis, 'Optofluidic dye lasers', *Microfluidics and Nanofluidics*. 2008. doi: 10.1007/s10404-007-0225-9.

[91] F. J. (Frank J.) Duarte, L. W. Hillman, P. F. Liao, and Paul. Kelley, 'Dye Laser Principles : With Applications.', p. 470, 1990.

[92] O. Svelto, 'Principles of Lasers', *Principles of Lasers*, 1976, doi: 10.1007/978-1-4899-2748-4.

[93] V. Ganjalizadeh, G. G. Meena, T. A. Wall, M. A. Stott, A. R. Hawkins, and H. Schmidt, 'Fast custom wavelet analysis technique for single molecule detection and identification', *Nature Communications 2022 13:1*, vol. 13, no. 1, pp. 1–9, Feb. 2022, doi: 10.1038/s41467-022-28703-z.

[94] V. Ganjalizadeh, H. Schmidt, and A. R. Hawkins, 'Adaptive time modulation technique for multiplexed on-chip particle detection across scales', *Optica, Vol. 10,*

Issue 7, pp. 812-818, vol. 10, no. 7, pp. 812–818, Jul. 2023, doi: 10.1364/OPTICA.489068.

[95] J. A. Black, V. Ganjalizadeh, J. W. Parks, and H. Schmidt, 'Multi-channel velocity multiplexing of single virus detection on an optofluidic chip', *Opt Lett*, 2018, doi: 10.1364/ol.43.004425.

[96] R. K. Kanaparthi, S. Saha, M. Singh, and A. M, 'Photophysical Properties of 4-(Dicyanomethylene)-2-Methyl-6-(4-Dimethylaminostyryl)-4H-Pyran (DCM) and Optical Sensing Applications', in *Photophysics, Photochemical and Substitution Reactions*, S. Saha, R. K. Kanaparthi, and T. V Soldatovi?, Eds., Rijeka: IntechOpen, 2020. doi: 10.5772/intechopen.93149.

[97] Y. Sun, T. L. Quyen, T. Q. Hung, W. H. Chin, A. Wolff, and D. D. Bang, 'A lab-on-a-chip system with integrated sample preparation and loop-mediated isothermal amplification for rapid and quantitative detection of Salmonella spp. in food samples', *Lab Chip*, 2015, doi: 10.1039/c4lc01459f.

[98] A. Hochstetter, 'Lab-on-a-chip technologies for the single cell level: Separation, analysis, and diagnostics', *Micromachines (Basel)*, vol. 11, no. 5, 2020, doi: 10.3390/MI11050468.

[99] A. Gökaltun, Y. B. (Abraham) Kang, M. L. Yarmush, O. B. Usta, and A. Asatekin, 'Simple Surface Modification of Poly(dimethylsiloxane) via Surface Segregating Smart Polymers for Biomicrofluidics', *Scientific Reports 2019 9:1*, vol. 9, no. 1, pp. 1–14, May 2019, doi: 10.1038/s41598-019-43625-5.

[100] E. M. Veziroglu and G. I. Mias, 'Characterizing Extracellular Vesicles and Their Diverse RNA Contents', *Front Genet*, vol. 11, p. 558262, Jul. 2020, doi: 10.3389/FGENE.2020.00700/BIBTEX.

[101] F. T. Borges, L. A. Reis, and N. Schor, 'Extracellular vesicles: Structure, function, and potential clinical uses in renal diseases', *Brazilian Journal of Medical and Biological Research*, vol. 46, no. 10, pp. 824–830, 2013, doi: 10.1590/1414-431X20132964.

[102] C. V. Harding, J. E. Heuser, and P. D. Stahl, 'Exosomes: Looking back three decades and into the future', *J Cell Biol*, vol. 200, no. 4, p. 367, Feb. 2013, doi: 10.1083/JCB.201212113.

[103] I. J. White, L. M. Bailey, M. R. Aghakhani, S. E. Moss, and C. E. Futter, 'EGF stimulates annexin 1-dependent inward vesiculation in a multivesicular endosome subpopulation', *EMBO J*, vol. 25, no. 1, p. 1, Jan. 2006, doi: 10.1038/SJ.EMBOJ.7600759.

[104] J. M. Pitt, G. Kroemer, and L. Zitvogel, 'Extracellular vesicles: Masters of intercellular communication and potential clinical interventions', *J. Clin. Investig.*, vol. 126, no. 4, pp. 1139–1143, Apr. 2016, doi: 10.1172/jci87316.

[105] G. Berumen Sánchez, K. E. Bunn, H. H. Pua, and M. Rafat, 'Extracellular vesicles: Mediators of intercellular communication in tissue injury and disease', *Cell Commun. Signal.*, vol. 19, no. 1, p. 104, Dec. 2021, doi: 10.1186/s12964-021-00787-y.

[106] J. L. Hood, S. San Roman, and S. A. Wickline, 'Exosomes released by melanoma cells prepare sentinel lymph nodes for tumor metastasis', *Cancer Res*, vol. 71, no. 11, pp. 3792–3801, Jun. 2011, doi: 10.1158/0008-5472.CAN-10-4455.

[107] J. Rak, 'Microparticles in cancer', *Semin Thromb Hemost*, vol. 36, no. 8, pp. 888–906, 2010, doi: 10.1055/S-0030-1267043.

[108] A. Becker, B. K. Thakur, J. M. Weiss, H. S. Kim, H. Peinado, and D. Lyden, 'Extracellular vesicles in cancer: Cell-to-cell mediators of metastasis', *Cancer Cell*, vol. 30, no. 6, pp. 836–848, Dec. 2016, doi: 10.1016/j.ccell.2016.10.009.

[109] S. Abdollahi, 'Extracellular vesicles from organoids and 3D culture systems', *Biotechnol Bioeng*, vol. 118, no. 3, pp. 1029–1049, Mar. 2021, doi: 10.1002/BIT.27606.

[110] R. E. Thompson, G. J. Bouma, and F. K. Hollinshead, 'The Roles of Extracellular Vesicles and Organoid Models in Female Reproductive Physiology', *Int J Mol Sci*, vol. 23, no. 6, Mar. 2022, doi: 10.3390/IJMS23063186.

[111] A. C. Buenafe, C. Dorrell, A. P. Reddy, J. Klimek, and D. L. Marks, 'Proteomic analysis distinguishes extracellular vesicles produced by cancerous versus healthy pancreatic organoids', *Scientific Reports 2022 12:1*, vol. 12, no. 1, pp. 1–14, Mar. 2022, doi: 10.1038/s41598-022-07451-6.

[112] S. T. Seiler *et al.*, 'Modular automated microfluidic cell culture platform reduces glycolytic stress in cerebral cortex organoids', *Scientific Reports 2022 12:1*, vol. 12, no. 1, pp. 1–12, Nov. 2022, doi: 10.1038/s41598-022-20096-9.

[113] T. H. Swartz, A. G. S. Palermo, S. K. Masur, and J. A. Aberg, 'The Science and Value of Diversity: Closing the Gaps in Our Understanding of Inclusion and Diversity', *J Infect Dis*, vol. 220, no. Suppl 2, p. S33, Sep. 2019, doi: 10.1093/INFDIS/JIZ174.

[114] B. K. AlShebli, T. Rahwan, and W. L. Woon, 'The preeminence of ethnic diversity in scientific collaboration', *Nature Communications 2018 9:1*, vol. 9, no. 1, pp. 1–10, Dec. 2018, doi: 10.1038/s41467-018-07634-8.

[115] P. V. Baudin *et al.*, 'Cloud-controlled microscopy enables remote project-based biology education in underserved Latinx communities', *Heliyon*, vol. 8, no. 11, p. e11596, Nov. 2022, doi: 10.1016/J.HELIYON.2022.E11596.

[116] S. Rufener, D. Mäusezahl, H. J. Mosler, and R. Weingartner, 'Quality of drinking-water at source and point-of-consumption--drinking cup as a high potential recontamination risk: a field study in Bolivia', *J Health Popul Nutr*, vol. 28, no. 1, pp. 34–41, 2010, doi: 10.3329/JHPN.V28I1.4521.

[117] W. Streifer, D. R. Scifres, and R. D. Burnham, 'Coupling Coefficients for Distributed Feedback Single- and Double-Heterostructure Diode Lasers', *IEEE J Quantum Electron*, vol. 11, no. 11, pp. 867–873, 1975, doi: 10.1109/JQE.1975.1068539.